The Fulde-Ferrell Larkin-Ovchinnikov Like State in Bilayers and Trilayers of Superconducting and Ferromagnetic Thin Films

Inaugural-Dissertation
zur Erlangung des Doktorgrades der
Mathematisch-Naturwissenschaftlichen Fakultät
der Universität Augsburg

vorgelegt von
Jan-Michael Kehrle

Augsburg, Januar 2012

Erster Berichterstatter: Prof. Dr. S.R. Horn

Zweiter Berichterstatter: Prof. Dr. L.R. Tagirov

Tag der mündlichen Prüfung: 23. Februar 2012

Table of Contents

1. Introduction

In science one can distinguish between target driven and curiosity driven research. While the first one has defined goals, *e.g.* in the case of corporates as new product, the curiosity driven research has the only goal to increase knowledge. However, this does not mean, that curiosity driven research has no benefit or output for the society. In contrary, the inventions coming out of it are and were the ones with the biggest impact in every body's life. For example in 1850 the British chancellor of Exchequer (minister of finance), William Gladstone, asked Michael Faraday, for the practical use of electricity and he replied: (I do not know, but) *"One day sir, you may tax it."* [**1**]. The present work is a curiosity driven research.

In 1987/88 Peter Grünberg, from the Forschungszentrum Jülich, and independently Albert Fert from the university Paris-South, discovered the giant magneto resistance [**2**], [**3**]. This phenomenon is observed in metallic layers with the layer thickness in the nanometer range. Thereby a metal is sandwiched between two magnetic layers. When applying a current to the layers the electrical resistivity depends on the direction of the magnetization relative to each other. The resistance is lower if the magnetization in the magnetic layers is parallel compared to an antiparallel orientation. The underling physical principle is that the scattering of electrons depends on the relative orientation of the magnetization of the magnetic layers. The scattering is more likely, and thus, the resistivity is higher, if the magnetization directions of the two layers are antiparallel.

This discovery was the starting point of spintronics [**4**], a research area in which the spin of the electron (instead of the electron charge) is used to manipulate and store information. Nowadays, most of the hard drive read heads are based on the spin valve phenomenon discovered by Grünberg and Fert. And still today researcher all over the world, in target as well in curiosity driven research, work on this field.

The present work investigates a superconducting spin valve, first proposed by L. Tagirov [**5**], at the Solid State Physics Department of the Kazan Federal University in Russia. The superconducting spin valve can be made up of two ferromagnetic layers which enclose a superconductor. Theoretical calculations show, that for a given suitable temperature the spin valve structure may be either in the normal conducting state or in the superconducting state, depending on the relative orientation of the magnetic layers. However, the fabrication of a functioning spin valve is rather difficult. It seems more straightforward to start with bilayers, which are easier to produce and control. Here, the optimal choice of parameters, such as the thickness of the superconducting and ferromagnetic layer, the crystalline orientation of the layers and the magnetic properties can be studied. If the optimal parameters have been found, they have to be verified in a trilayer system. However, it is likely that in a trilayer system no switching occurs because the magnetization of the magnetic layers point always into the same direction (if they do not have a different coercive field) when rotated by an external field. Therefore, a fourth layer is introduced in order to fix the magnetization direction of one of the ferromagnetic layers, while the magnetic orientation of the second one is turned to an opposite direction relative to the first one using an external magnetic field.

The present work is arranged in the following way. In the second chapter, the theoretical background is discussed, first in a qualitative way, in order to present the main ideas of the theory, and then in a rigorous mathematical derivation. The third chapter, handling the sample preparation, contents which samples have been prepared and with which methods. Since the thickness of the layer has strong influence on the properties of the system, it has to be controlled with a high accuracy. The thickness and atomic composition is, therefore, determined by Rutherford Backscattering Spectrometry. This measurement procedure as well as the fitting is described in chapter 4. In the next chapter, the samples are analyzed with a Transmission Electron Microscope. Thereby the atomic lattice structure of the individual layers can be determined by electron diffraction. Furthermore, the thickness of the layers and the quality of the interfaces as well as the crystalline orientation can be identified by High Resolution imaging. The sixth chapter covers the analysis of the magnetic properties of the copper-nickel alloy layer used as ferromagnetic material in bilayers and trilayers and the properties of the antiferromagnetic cobalt oxide layer, which serves to exchange bias one of the ferromagnetic layers. In the last chapter, the resistance measurements at low temperatures are reported, which are applied to study the superconducting properties. Furthermore, the theory is fitted to the experimental measurement points and the obtained results are interpreted.

2. Theory

2.1. Qualitative Description of the Fulde-Ferrell Larkin-Ovchinnikov (FFLO) Like State

It is now 100 years ago, that in 1911, Heike Kamerlingh Onnes discovered that at low temperatures the resistivity of mercury vanishes. Since this time a lot of different elements and other materials have shown to become superconducting at low temperatures [**6**].

In 1957 Bardeen, Cooper and Schrieffer (BCS) developed the BCS-theory, which was able to explain the origin of superconductivity and lots of its associated phenomena on a microscopic level [**7**], [**8**]. The key assumption is that the superconducting state consists of electron pairs ("Cooper pairs") with opposite spin and momentum, which experience an attractive interaction via the exchange of virtual phonons. From the presence of opposite spins, it becomes obvious that superconductivity, as described by the BCS theory, and ferromagnetism, which favours a parallel alignment of the electron spins, are two antagonistic phenomena. Nevertheless, in 1964 Fulde and Ferrell [**9**], and independently Larkin and Ovchinnikov, (FFLO) [**10**], [**11**] showed the possibility of the formation of superconductivity in a homogenous material in the presence of a ferromagnetic background, *i.e.* an exchange field.

In this framework FFLO extended the BCS theory to the case where the total momentum of the electrons in a Cooper pair is not equal to zero, but electrons have still opposite spins. The existence of a net total momentum, $\Delta\vec{k} \neq 0$, becomes obvious when considering the electron dispersion in the presence of an exchange field, as shown in Fig. 2.1.

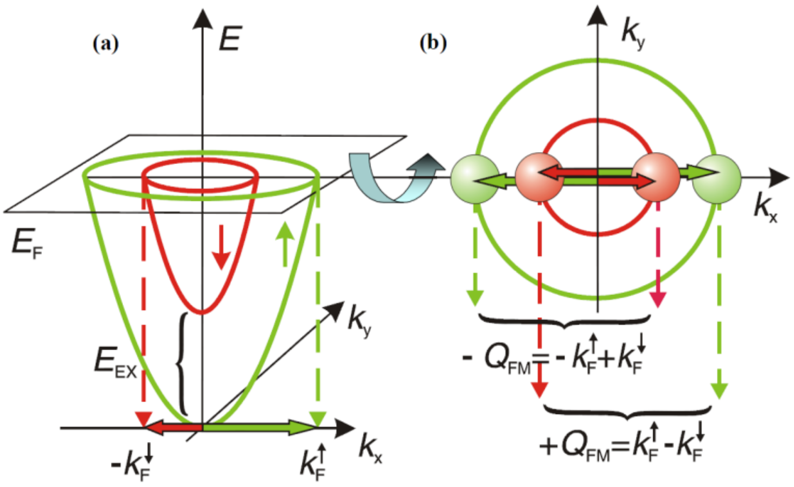

Fig. 2.1: a) Sketch of the electron dispersion relation due to the presence of an exchange field. b) In the framework of the BCS theory, the formation of Cooper pairs is possible when the total momentum of a pair Q_{FM} is not zero (from Ref. [12]).

In Fig. 2.1a) the exchange field, E_{ex}, splits the free-electron-like conduction band into a spin up, the majority, and a spin down, the minority spin sub-band. The $E(k_x,k_y)$ parabola for the different spins is shifted with respect to each other, yielding a net momentum when electrons with opposite spin pair, *e.g.* $-k_x^{\downarrow} + k_x^{\uparrow} \neq 0$. In Fig. 2.1b) a top view of the dispersion relation cut at the Fermi energy is shown. The case of a parallel spin alignment of the electron pairs, *i.e.* the formation of triplet superconductivity is possible, but not considered in the description of the FFLO state. Thus, staying in the framework of the BCS theory, a pairing with opposite spins yields a net total momentum, $\pm Q_{FM}$.

Basically the FFLO state was predicted as a superconducting state on a ferromagnetic background in a homogenous material. However, this formation of unconventional superconductivity can be just observed in a narrow range of parameters [**13**]. However, recently evidence for this kind of superconductivity was found to appear in heavy fermion and organic superconductors, [**14**,**15**,**16**].

In thin film layered structures of superconductors (S) and ferromagnets (F) a quasi-one dimensional FFLO like state can be induced. Thereby, the superconducting pair penetrates form the S-material into the ferromagnet acquiring a non-zero pairing momentum. The word quasi-one dimensional takes fact that the properties of the system only changes in the dimension, which is perpendicular to the layers.

After Wong et al. [**17**] observed a non-monotonic behavior of the superconducting transition temperature, T_c, on the Fe layer thickness in V/Fe multilayers, A.I.

Buzdin and M.Yu. Kupriyanov [**18**] and Radovic et al. [**19**] predicted such FFLO like pairing in S/F layered structures, leading to an oscillating behavior of the superconducting transition temperature. Because the Usadel equations [**20**] are the starting point of the theoretical developments [**20**,**21**,**19**,**22**,**23**], theories are only valid in the framework of the Usadel equations, *i.e.* for a dirty superconductor and ferromagnet. This means that $l << \xi$, *i.e.* the coherence length, ξ, must be much larger than electron mean free path, *l*, of electrons in the conduction band for the superconductor and the ferromagnet, respectively.

For a dirty superconductor $l_S << \xi_{BCS}$, with the BCS coherence length $\xi_{BCS} = \frac{\hbar v_S \gamma}{\pi^2 k_B T_{c0}}$. Here, $\gamma = e^C = 1.781$ where C=0.577 is the Euler-Mascheroni constant [**24**], k_B Boltzmann's constant, v_S the Fermi velocity of the superconductor, and T_{c0} the critical temperature of the superconductor. Moreover, l_S is the electron mean free path in the S-metal.

For a dirty ferromagnet $l_{F0} << \xi_{F0}$ with $\xi_{F0} = \frac{\hbar v_F}{E_{ex}}$, where v_F is the Fermi velocity in the F-material and E_{ex} the exchange energy. Moreover, l_{F} is the electron mean free path in the F-metal.

In Fig. 2.2 the penetration of the pairing wave function from the superconductor (S) into the ferromagnet (F) is shown. The pairing wave function not only decays into the ferromagnet, as it is known from the superconductor/normal metal proximity effect, but oscillates in addition [**25**,**26**,**27**]. In Fig. 2.2a) the thickness of the ferromagnet is given by d_{F1}. The pairing wave function is reflected at the boundary to the vacuum and interferes with the incoming part. As a result, the wave function is diminished until a thickness d_{F1} is reached, as illustrated in Fig. 2.2a). Increasing the thickness of the ferromagnet further to d_{F2} (see Fig. 2.2b) leads again to an increase of the total amplitude of the pairing wave function. Because the pairing wave function flux through the S/F interface oscillates as a function of the ferromagnetic layer thickness, the transition temperature $T_{\mathrm{c}}(d_{\mathrm{F}})$ shows a monotonic oscillating behavior (as given in Fig. 2.2c). Although the sketch in Fig. 2.2 gives a quite good impression of the consequences of the presence of an oscillation of the pairing wave function, it is a classical picture which tries to explain a quantum mechanical effect. It seems to have some shortcomings in explaining a total supersession of superconductivity. Since the pairing wave function is decaying into the ferromagnetic material, a complete extinction by destructive interference can only be explained in this picture if much more than 50 % of the pairing wave function amplitude penetrates into the F-material.

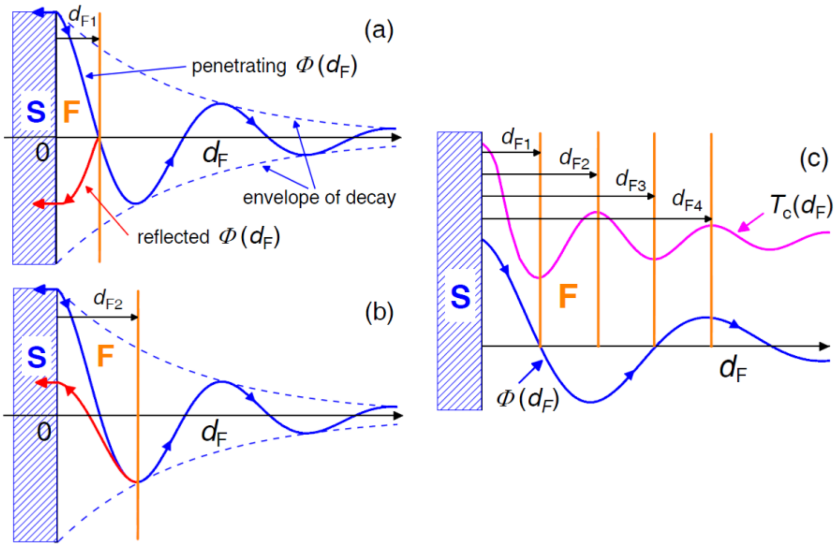

Fig. 2.2: In a superconductor/ferromagnet thin film system the pairing wave function Φ_F oscillates due to the presence of an exchange field. Interference effects occur if the paring wave function is reflected at the boundary to the vacuum and interacts with itself. Here it is assumed that ½ of the pairing wave function penetrates from S to F and ½ is reflected at the S/F boundary (from Ref. [12]).

It is not clear whether this is really necessary to result in the extinction of superconductivity which is predicted by theory [**22**] and was observed experimentally recently [**28**,**29**,**30**]. This extinction extends over a certain range of d_F. Also this property cannot be explained in the classical picture of Fig. 2.2.

The decay length of the pairing wave function in the F-material is given by $2l_F$ and $\xi_{FD} = \sqrt{\frac{2\hbar D_F}{E_{ex}}}$ for a clean and a dirty ferromagnet, respectively [**21**,**22**,**31**]. The oscillation wave length is $\lambda_{F0} = 2\pi\xi_{F0}$, where $\xi_{F0} = \hbar v_F / E_{ex}$, and $\lambda_{FD} = 2\pi\xi_{FD}$ in the clean [**31**,**32**] and dirty [**21**,**25**] F-metal, respectively. Here $D_F = \frac{1}{3} l_F v_F$ is the diffusion coefficient in the F-material and $\hbar$ is Plank's constant. For details see the Appendix. The superconductor is always assumed to be dirty, *i.e.* $l_S << \xi_{BCS}$.

From these equations it can be seen that in a strong ferromagnet with a large exchange field, E_{ex}, in the range of 0.1-1.0 eV, like for iron, cobalt or nickel [**33**], the pairing wave function oscillates with a high frequency. Diluting a strong ferromagnet, for instance by forming a copper-nickel alloy, the exchange splitting energy, E_{ex}, decreases one order of magnitude, yielding an increase of the decay length and oscillation wavelength. This shifts the ferromagnetic thin film thickness, where an extinction of the superconductivity is expected from very small d_F to a range between 5-10 nm, [**29**,**34**].

Pioneering works in theoretical description of spatially inhomogeneous superconducting systems (stacks of layers, for example) were done by G. Eilenberger [**35**] in 1968 and by K. Usadel [**20**] in 1970, who developed a quasi-classical approach to the theory of superconductivity. Another 20 years elapsed before A.I. Buzdin and M.Yu. Kupriyanov [**18**] implemented an exchange field into the quasi-classical Usadel theory. The Usadel equations are valid for dirty superconductors and ferromagnets as already discussed in detail above. In the case of F/S hybrids one has to distinguish two coherence lengths, one in the superconductor, ξ_s, and one in the ferromagnet ξ_{F0}.

The Usadel equations are second order differential equations. The specific solution for the pairing wave function can be found by its boundary conditions. The physical more interesting boundary condition, compared to the interface with vacuum, is the interface between the superconductor and the ferromagnet, *i.e.* the S/F interface. In the early work of Ivanov et al. [**36**] it was assumed that the pairing wave function must be continuous across the boundary, *i.e.* without a step. However, fitting the experimental data with this approach was only possible assuming that the ratio of conductivities in the ferromagnet and superconductor, in the normal conducting state, differs by orders of magnitude [**31**]. L. Tagirov [**22**], following the ideas of M.Yu Kupriyanov and V. Lukichev for boundary conditions at S/N interfaces [**37**], realized that the physical reasonable postulation of a continuous boundary condition was not necessary in a quasi-classical approach. The discontinuity of the quasi classical Green function was independently realized in [**31**], however, without discussion.

Fig. 2.3 illustrates the relation between the exact Gorkov Green function for the superconducting pairing and the quasi-classical approach. While the Gorkov function is a superposition of incident and reflected wave functions and is damped on the ferromagnetic side, the quasi-classical function can be considered as the envelope function of the exact wave function. Although the exact Green function has to be continuous across the boundary the envelope function can be discontinuous.

The Usadel equation is valid in a regime where the ferromagnet and the superconductor can be assumed to be dirty. However, in strong ferromagnets like iron, nickel or cobalt, the internal exchange field is so strong that the superconducting coherence length gets smaller or equal to the mean free path of the conduction electrons, i.e. the ferromagnet is in the clean limit. In this case the Usadel equation cannot longer be applied to the ferromagnetic material, and the much more complicated Eilenberger theory has to be used. However, from computer simulations of the general Gorkov type Green function in layered structures it was shown by L. Tagirov in 1998 [**22**] that the Usadel equation in the ferromagnetic layer can be still used in a first approximation if the diffusion coefficient is replaced with the one dimensional analogue (*i.e.* the three dimensional multiplied by 3: $(D_F)_{eff} = l_F v_F$); see also Ref. [**38**]). In the ferromagnet the diffusion coefficient is a complex quantity given by ([**22**] Eq. 3.16) $\widetilde{D}_F = D_F/(1 + i\hbar^{-1}E_{ex}\tau_F) = D_F/(1 + il_F/\xi_{F0})$, considering that $\tau_F = l_F/v_F$ and $\xi_{F0} = \hbar v_F/E_{ex}$. For the dirty ferromagnet and the clean ferromagnet, D_F is then given by $v_F l_F/3$ and $v_F l_F$, respectively. In early works [**19**,**21**], valid in the dirty limit, D_F instead of $\widetilde{D}_F$ is used (see also the discussion in Chap. 3.1.2.1 of Ref. [**22**]). Samples with $l_F \approx \xi_{FD}$ representing the intermediate case between the dirty and clean, have so far not considered in this framework. In this case they are best described by applying the dirty case theory extended toward the clean case, as discussed above, to the intermediate range [**28**,**34**].

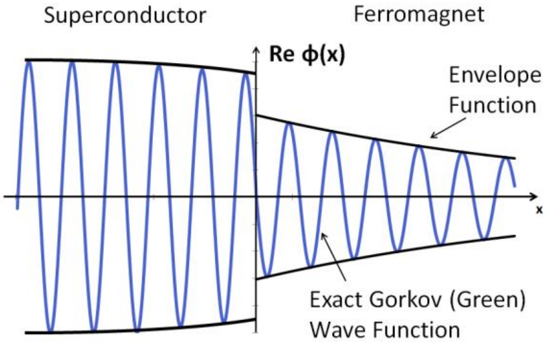

Fig. 2.3: The exact Gorkov Green function passes the interface continuously while the envelope function, used in the quasi classical approach, may be discontinues at the interface (according to Ref. [39**]). This envelope function actually oscillates in the FFLO like state.**

In 1999 L. Tagirov proposed a superconducting spin valve or, alternatively, a AF-F/S/F spin switch [**5**]. The spin valve core structure is built up of a F/S/F trilayer system. The F/S/F trilayer structure can be considered as a stack of two bilayers, *e.g.* F/S and S/F, if the S-layer thickness is two times that of the corresponding bilayer. By changing the relative alignment of the magnetization of the ferromagnetic layer, the transition temperature of the system can be changed. The largest change in the resistance is obtained if the trilayers changes from the superconducting state to the normal conducting state by changing the magnetization direction of one of the F-layers with respect to the other.

In order to keep the magnetization direction fixed for one of the F layers while the second F-layer’s magnetization is rotated, a fourth layer has to be introduced. In this structure one of the ferromagnetic layers is in contact with an antiferromagnetic layer, which keeps the orientation of one of the ferromagnetic layers fixed.

In Fig. 2.4 theoretical calculations for the transition temperature for a F/S/F spin valve core structure with F=$Cu_{41}Ni_{59}$ and S=Nb with a parallel alignment T_c^{AP} , and an antiparallel alignment T_c^{AP} of the ferromagnetic layers are given. The difference, ΔT_c, of both temperatures is given as a red line.

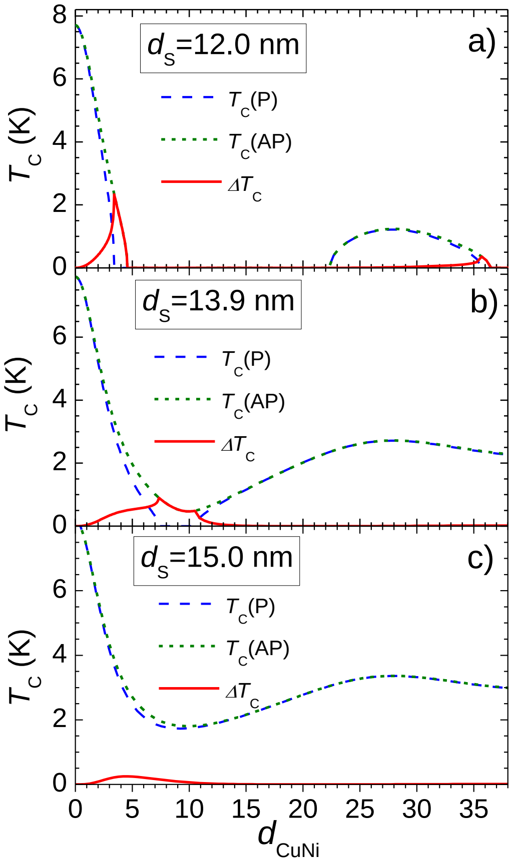

Fig. 2.4 a)-c) show the transition temperature of a F/S/F spin valve core structure for F=$Cu_{41}Ni_{59}$ where the relative orientation of the ferromagnetic layer is either parallel or antiparallel. The difference of both temperatures is given by ΔT_c. The thickness of the superconducting layer is increasing from a) 12 nm, to b) 13.9 nm and c) 15.0 nm. Here, d_{CuNi} is given in nm (from Ref. [28]).

The calculations have been made with parameters which can be obtained from S/F bilayers investigations of these materials. From Fig. 2.4a) to c) the thickness of the superconducting niobium layer increases from 12.0 nm, to 13.9 nm to 15.0 nm. The thickness of each of the layers, d_{CuNi}, is assumed to increase in narrow steps. For the superconducting layer with a thickness of 15 nm (Fig. 2.4c), the oscillation of the transition temperature is already distinct. Nevertheless, the difference in the transition temperature is still small. Decreasing the niobium thickness leads to a more pronounced oscillation (Fig. 2.4b) and to an increase in the shift of the critical temperature. When the niobium layer thickness is decreased to

12.0 nm, which would correspond to a thickness of about 6.0 nm for a S/F bilayer, first a decrease of the critical temperature can be observed. For a thickness of the F-layers in between 3-5 nm, depending on the relative orientation of the ferromagnetic layers, a vanishing of the superconducting transition temperature occurs. For the F-layer thickness of about 22 nm the transition temperature recovers again before it is suppressed again for ferromagnetic layer thicknesses above 36 nm. The largest ΔT_c effect with more than 2 Kelvin can be obtained when this “reentrant behavior” of the superconducting state is present.

In Fig. 2.5 the relation between the superconducting layer thickness, the optimized ferromagnetic layer thickness (for which the maximum ΔT_c, is observed for a given S-layer thickness) and the the maximal difference ΔT_c in the transititon temperature for the P and AP alignments is shown. For the calculations again a niobium layer, sandwiched by two copper-nickel layers, has been assumed.

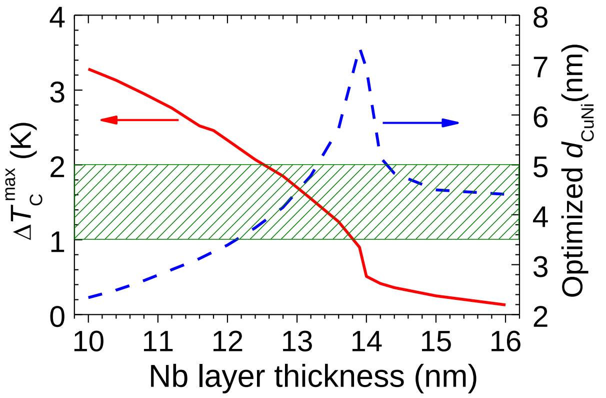

Fig. 2.5. The red curve gives the maximum spin switch effect, *e.g.* the maximum difference of the superconducting transition temperature between the parallel and antiparallel alignment of both F-layers. The blue curve gives the optimized thickness for the corresponding F-layer (from Ref. [28]).

The superconducting layer thickness was varied between about 10 and 16 nm, while the optimized ferromagnetic layer thickness ranges between 2 and 8 nm. The largest effect, with a switching temperature of over 3 K, is achieved for a niobium thickness of about 10 nm. However, for this the $Cu_{41}Ni_{59}$ layer must have a thickness of only 2 nm, which is a very thin layer and, thus, difficult to achieve in practice, due to the possibiltity of interdiffusion of the superconductor and the ferromagnet. In Fig. 2.5, the green shaded region, gives the parameter range where the switching effect is as large as 1-2 K. In this range the Nb thickness is 12.5-13.8 nm while that of the copper-nickel layer is 3.5-5.0 nm, which are dimensions which can be realized experimentally in a secure manner.

2.2. Derivation of the Fulde-Ferrell Larkin-Ovchinnikov Like State

In this chapter the derivation of the FFLO like state in superconductor/ferromagnet layered structures will be derived, starting from the Usadel equation. The work is based on Refs. [**23**,**28**] and private communications of L. Tagirov. Throughout this subchapter we set Boltzmann's constant and Planck's constant, $\hbar = k_B = 1$, respectively, if not other stated.

In the ferromagnetic region, the Usadel equation is given by [**23**],

$$\left\{ |\omega| + \frac{iE_{ex}}{2} - \tfrac{1}{2} D_F \frac{d^2}{dx^2} \right\} \Phi_F(x,\omega) = 0 \tag{2.1}$$

Where ω is the Matsubara frequency, $\omega = \pi T(2n+1)$ for *n=0,±1, ±2, ±3,…* which connects the excitation energies of phonons with the thermal energy *T*, and E_{Ex} is the exchange energy. Following earlier descriptions of the FFLO like state, valid in the dirty limit, the diffusion coefficient is given by $D_F = l_F v_F / 3$, where $(l_F v_F)$ is the product of the mean free path, l_F, and Fermi velocity, v_F, of the electrons in the F material, whereas it has to be replaced by $\tilde{D}_F = \frac{D_F}{1 + il_F / \xi_{F0}}$ with $D_F = l_F v_F / 3$ and $l_F v_F$ in the case of a dirty and clean ferromagnet, respectively, according to more recent theoretical work, as already discussed in Chap. 2.1. Moreover, Φ_F is the pairing wave function in the ferromagnetic material.

In the superconducting region the Usadel equation is [**23**],

$$\left\{ |\omega| - \tfrac{1}{2} D_S \frac{d^2}{dx^2} \right\} \Phi_S(x,\omega) = \Delta_S(x) \tag{2.2}$$

with the self-consistency equation [**19**],

$$\Delta_S(x) = \pi T \lambda \sum_{\omega} \Phi_S(x,\omega) \tag{2.3}$$

where $D_S = v_S l_S / 3$ is the diffusion coefficient of the electrons in the S material, where l_S and v_S are the electron mean free path and Fermi velocity in the S-material, respectively. Moreover, Φ_S is the pairing wave function in the superconductor, $\Delta_S(x)$ the order parameter of the superconducting state, and λ is the coupling constant of the electron-electron interaction, which is given by (using k_B= k_B and ħ= ħ) $\lambda = (\pi k_B T_{c0} \sum_{\omega} \frac{1}{\hbar |\omega|})^{-1}$, see *e.g.* Ref. [**19**]. Here T_{c0} is the critical temperature of the superconductor.

a) First, a general solution of the Usadel equation in the ferromagnetic region will be found. Therefore, the equation will be rearranged, yielding

$$\frac{1}{2} D_F \left\{ \frac{2|\omega| + iE_{ex}}{D_F} - \frac{d^2}{dx^2} \right\} \Phi_F(x,\omega) = 0 \tag{2.4}$$

$$\Rightarrow \quad \frac{2|\omega| + iE_{ex}}{D_F} \Phi_F(x,\omega) = \frac{d^2}{dx^2} \Phi_F(x,\omega) \tag{2.5}$$

On the left hand side the Matsubara frequency may be neglected, because the exchange energy of the ferromagnet is much larger than the thermal energy of the system during the experiments. For the exchange energy, $E_{exc} = 0.3\ eV$ may be taken [**40**] which is equivalent to a temperature, $E_{Ex} = k_B T$, of about 3500 K. This is orders of magnitude larger than the transition temperature of any superconductor. Thus, Eq. (2.5) can be simplified to,

$$k_F^2 \Phi_F(x,\omega) = \frac{d^2}{dx^2} \Phi_F(x,\omega) \tag{2.6}$$

which is a homogenous second order differential equation with the general solution

$$\Phi_F = C_1 e^{k_F x} + C_2 e^{-k_F x} \tag{2.7}$$

where k_F^2 is defined as

$$k_F^2 = \frac{iE_{ex}}{D_F} \tag{2.8}$$

In order to find a specific solution for this problem, the boundary conditions have to be considered. An overview over the geometry of the system is given in Fig. 2.6.

The system is considered to be one-dimensional along the shown axis. The origin of the coordinate axis is placed in the middle of the superconducting layer. The S-layer is sandwiched between the two ferromagnetic layers, given in the formulas as indices FR and FL for the right and left layer, respectively.

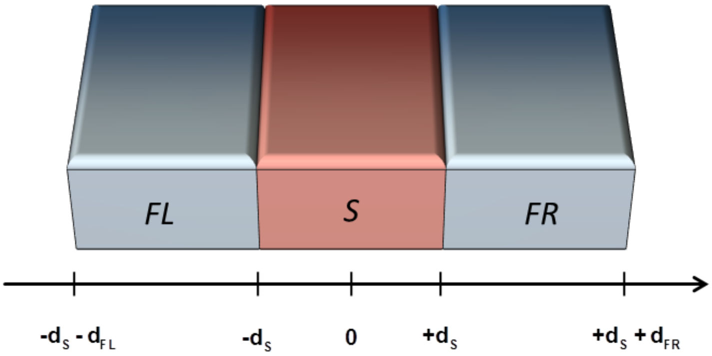

Fig. 2.6: Geometrical structure of the ferromagnet/superconductor/ferromagnet system, where FL denotes the left ferromagnet, FR the right ferromagnet, and S the superconductor.

A necessary boundary condition is that there is no flux from the ferromagnet into the vacuum on both sides. For the geometry as given in Fig. 2.6 this can be written as,

$$\frac{d}{dx}\Phi_F(\pm d_S \pm d_{\frac{FR}{FL}},\omega)=0 \tag{2.9}$$

For the boundary at the right ferromagnetic layer, one can write by using the general solution,

$$\frac{d}{dx}\Phi_{FR} = \left\{C_1 e^{k_{FR}x} - C_2 e^{-k_{FR}x}\right\}\Big|_{x=d_s+d_{FR}} k_{FR} = 0 \tag{2.10}$$

Since the wave vector k_F can be assumed to be non-zero (otherwise one will get a constant solution which vanishes according to Eq. (2.6)), this can be rearranged to:

$$C_2 = C_1 \frac{e^{k_{FR}x}}{e^{-k_{FR}x}}\Big|_{x=d_s+d_{FR}} = C_1 e^{2k_{FR}x}\Big|_{x=d_s+d_{FR}} = C_1 e^{2k_{FR}(d_s+d_{FR})} \tag{2.11}$$

With this result the pairing wave function for the right ferromagnetic layer becomes,

$$\Phi_{FR} = C_1 e^{k_{FR}x} + e^{-k_{FR}x} C_1 e^{2k_{FR}(d_s+d_{FR})} = \tag{2.12}$$

$$= e^{k_{FR}(d_s+d_{FR})} C_1 \left\{ e^{-k_{FR}(d_s+d_{FR})} e^{k_{FR}x} + e^{-k_{FR}x} e^{k_{FR}(d_s+d_{FR})} \right\} = \tag{2.13}$$

$$= C_1 e^{k_{FR}(d_s+d_{FR})} \left\{ e^{k_{FR}(x-d_s-d_{FR})} + e^{-k_{FR}(x-d_s-d_{FR})} \right\} = \tag{2.14}$$

$$= 2C_1 e^{k_{FR}(d_s + d_{FR})} \cosh\left[k_{FR}(x - d_s - d_{FR})\right] = \tag{2.15}$$

$$= C_{FR} \cosh\left[k_{FR}(x - d_s - d_{FR})\right] \tag{2.16}$$

where a new constant $C_{FR} = 2C_1 e^{k_{FR}(d_s + d_{FR})}$ was introduced in order to simplify the equation. So the pairing wave function for the right, and analogous for the left ferromagnetic side, are

$$\Phi_{FR}(x) = C_{FR} \cosh\left[k_{FR}(x - d_s - d_{FR})\right] \tag{2.17}$$

and

$$\Phi_{FL}(x) = C_{FL} \cosh\left[k_{FL}(x + d_s + d_{FL})\right] \tag{2.18}$$

where $C_{FL} = 2C_1 e^{-k_{FL}}\left(d_s + d_{FL}\right)$.

b) In order to find a solution for the self-consistency equation (Eq. (2.3)), in a first step the electron-electron coupling constant $\lambda = (\pi k_B T_{c0} \sum_{\omega} \frac{1}{\hbar|\omega|})^{-1}$ will be rewritten (here, k_B= $\mathrm{k_B}$ and ℏ= ℏ). Here ω are the Matsubara frequencies given by

$$\omega\hbar = \pi k_B T(2n+1) \quad \text{where} \quad n = 0, \pm1, \pm2, \pm3, \ldots \tag{2.19}$$

In a first step it is assumed, that the Debye temperature, Θ_D, is much larger than the superconducting transition temperature, i.e. $\Theta_D = \omega_D \hbar / k_B >> T_{c0}$ [**41**]. Considering that $\omega_D \hbar = \pi k_B T(2n_D + 1)$ one gets

$$n_D = \frac{\hbar\omega_D}{2\pi k_B T} - \frac{1}{2} \simeq \frac{\hbar\omega_D}{2\pi k_B T} >> 1 \tag{2.20}$$

Next, the term in brackets of the expression of the electron-electron coupling constant λ, *i.e.* $\pi k_B T_{c0} \sum_{\omega} \frac{1}{\hbar|\omega|} = S$, where $\omega = \omega(T_{c0})$, can be rearranged in the following way,

$$\begin{aligned} S = \pi k_B T_{c0} \sum_{\omega} \frac{1}{\hbar|\omega|} &= \pi k_B T_{c0} \sum_{n=0}^{n=\pm n_D} \frac{1}{\pi k_B T_{c0} |2n+1|} = \\ &= 2 \sum_{n=0}^{n=n_D} \frac{1}{(2n+1)} \end{aligned} \tag{2.21}$$

with $n_D=n_D(T_{c0})$. Using a mathematical handbook [**42**], the sum on the right hand side can be written as

$$\sum_{n=0}^{n=n_D} \frac{1}{(2n+1)} = \frac{1}{2}(C+\ln n_D) + \ln 2 + \frac{B_2}{8n_D^2} + \frac{(2^3-1)}{64n_D^4}B_4 + \ldots \qquad (2.22)$$

Where B are the Bernoulli numbers ([**43**] p. 804) and $C=0.577$ is the Euler-Mascheroni constant.

Since $\omega_D\hbar >> k_B T_{c0}$, it follows that $n_D >> 1$, as discussed above (typical values are around 10 [**39**]). Thus, terms in higher order of n_D can be neglected, *i.e.* $\frac{B_2}{8n_D^2} + \frac{(2^3-1)}{64n_D^4}B_4 + \ldots$, because the Bernoulli numbers B_2 and B_4 have the values 1/6 and -1/30, respectively. Then, using $C=\ln(e^C)$, one gets

$$\begin{aligned} 2\sum_{n=0}^{n=n_D} \frac{1}{(2n+1)} &= \ln e^C + \ln n_D + 2\ln 2 = \ln(n_D e^C 2^2) = \\ &= \ln\frac{4e^C\hbar\omega_D}{2\pi k_B T_{c0}} = \ln\frac{2e^C\hbar\omega_D}{\pi k_B T_{c0}} = \ln\left(\frac{1.134\hbar\omega_D}{k_B T_{c0}}\right) \end{aligned} \qquad (2.23)$$

Thus, λ can be re-written as:

$$\lambda = S^{-1} = (\pi k_B T_{c0}\sum_{\omega}\frac{1}{\hbar|\omega|})^{-1} = \left[\ln\left(\frac{1.134\hbar\omega_D}{k_B T_{c0}}\right)\right]^{-1} \qquad (2.24)$$

which is substituted into the self-consistency equation, Eq. (2.3), yielding (with $k_B= k_B$)

$$\Delta_S(x) = \pi k_B T\left[\ln\left(\frac{1.134\hbar\omega_D}{k_B T_{c0}}\right)\right]^{-1}\sum_{\omega}\Phi_S(x,\omega) \qquad (2.25)$$

where $\omega=\omega(T)$, resulting in

$$\begin{aligned} \Delta_S \ln\left(\frac{1.134\hbar\omega_D}{k_B T_{c0}}\right) &= \pi k_B T\sum_{\omega}\left(\Phi_S - \frac{\Delta_S}{\hbar|\omega|} + \frac{\Delta_S}{\hbar|\omega|}\right) = \\ &= \pi k_B T\sum_{\omega}\left(\Phi_S - \frac{\Delta_S}{\hbar|\omega|}\right) + \Delta_S \pi k_B T\sum_{\omega}\frac{1}{\hbar|\omega|} = \\ &= \pi k_B T\sum_{\omega}\left(\Phi_S - \frac{\Delta_S}{\hbar|\omega|}\right) + \Delta_S \ln\left(\frac{1.134\hbar\omega_D}{k_B T}\right) \end{aligned} \qquad (2.26)$$

yielding,

$$\Delta_S \ln\frac{T}{T_{C0}} = \pi k_B T \sum_{\omega}\left(\Phi_S - \frac{\Delta_S}{\hbar|\omega|}\right) \tag{2.27}$$

This can be rearranged, considering that $\ln(1/x) = \ln 1 - \ln x = -\ln x$, yielding

$$\Delta_S \ln\frac{T_{c0}}{T} = \pi k_B T \sum_{\omega}\left(\frac{\Delta_S}{\hbar|\omega|} - \Phi_S\right) = 2\pi k_B T \sum_{\omega>0}\left(\frac{\Delta_S}{\hbar\omega} - \Phi_S\right) \tag{2.28}$$

The above equation is written similar to the form given by Ref. [**21**]. But actually there are two pairing functions, $\Phi^+ = \Phi_{\uparrow\downarrow}$ and $\Phi^- = \Phi_{\downarrow\uparrow}$ [**23**] where the lower index stands for the electron spin projection. Thus, Eq. (2.28) can be written as

$$\begin{aligned}\Delta_S \ln\frac{T_{c0}}{T} &= 2\pi k_B T \sum_{\omega>0}\left[\frac{\Delta_S}{\hbar\omega} - \frac{1}{2}\left(\Phi_{\uparrow\downarrow}(\omega) + \Phi_{\downarrow\uparrow}(\omega)\right)\right] = \\ &= \pi k_B T \sum_{\omega>0}\left[\frac{2\Delta_S}{\hbar\omega} - \Phi_{\uparrow\downarrow}(\omega) - \Phi_{\downarrow\uparrow}(\omega)\right]\end{aligned} \tag{2.29}$$

Comparing the notation with Ref. [**23**], one has to replace $\Phi_{\uparrow\downarrow}(\omega) = \Phi^+$ by F^+ and $\Phi_{\downarrow\uparrow}(\omega) = \Phi^-$ by F^-. In order to solve this equation, one uses the Ansatz of Ref. [**21**] Eq. (3), for $\Phi^\pm$, which is given by

$$\Phi^\pm(x,\omega) = \frac{\Delta_S(x)}{\hbar\omega + 2\pi k_B T_{c0}\rho^\pm(t)} \tag{2.30}$$

where $t = \frac{T}{T_{c0}}$. Regarding now the case of a certain sample, e.g. an S/F bilayer, with a transition temperature T_c, the temperature T in Eq. (2.29) has to be replaced by T_c and the parameter t in Eq. (2.30) by $t_c = \frac{T_c}{T_{c0}}$. With $\ln(1/t_c) = -\ln t_c$ one gets by combining Eqs. (2.29) and (2.30)

$$-\Delta_S \ln t_c = \pi k_B T_c \sum_{\omega>0}\left(\frac{2\Delta_S}{\hbar\omega} - \frac{\Delta_S}{\hbar\omega + 2\pi k_B T_{c0}\rho^+} - \frac{\Delta_S}{\hbar\omega + 2\pi k_B T_{c0}\rho^-}\right) \tag{2.31}$$

where ρ^+ and ρ^- are the pair breaking parameters related to Φ^+ and Φ^-, respectively. Substituting $\hbar\omega = \pi k_B T(2n+1)$ for T=T_c yields,

$$-\Delta_S \ln t_c = \pi k_B T_c \sum_{n>0} \Big(\frac{2\Delta_S}{\pi k_B T_c (2n+1)} - \frac{\Delta_S}{\pi k_B T_c (2n+1) + 2\pi k_B T_{c0} \rho^+} - \frac{\Delta_S}{\pi k_B T_c (2n+1) + 2\pi k_B T_{c0} \rho^-} \Big) \tag{2.32}$$

Using again the definition of t_c and shortening the expression further yields

$$-\Delta_S \ln t_c = \sum_{n>0} \left(\frac{2\Delta_S}{(2n+1)} - \frac{\Delta_S}{(2n+1) + 2\rho^+ / t_c} - \frac{\Delta_S}{(2n+1) + 2\rho^- / t_c} \right) \tag{2.33}$$

$$-\ln t_c = \sum_{n>0} \left(\frac{1}{n+1/2} - \frac{1}{2} \left(\frac{1}{n+1/2+\rho^+ / t_c} \right) - \frac{1}{2} \left(\frac{1}{n+1/2+\rho^- / t_c} \right) \right) \tag{2.34}$$

The above expression can be rearranged, by using a series expansion for the digamma function ($\Psi(x) = -C - \sum_{k=0}^{\infty} \left[\frac{1}{x+k} - \frac{1}{k+1} \right]$, given in Ref. [**44**] p. 952), in the following way, $\sum_{k=0}^{\infty} \frac{1}{x+k} = -\Psi(x) - C + \sum_{k=0}^{\infty} \frac{1}{k+1} = -\Psi(x) + W$. During the rearrangement the contributions containing W cancel, and one arrives at,

$$\ln t_c = \Psi\left(\frac{1}{2}\right) - \frac{1}{2} \Psi\left(\frac{1}{2} + \frac{\rho^+}{t_c}\right) - \frac{1}{2} \Psi\left(\frac{1}{2} + \frac{\rho^-}{t_c}\right) \tag{2.35}$$

Because for the digamma function it is, $\Psi\left(z^*\right) = \Psi^*\left(z\right)$ [**43**] p. 259, as far as $\rho^- = \left(\rho^+\right)^*$ one gets,

$$\ln t_c = \Psi\left(\frac{1}{2}\right) - \mathrm{Re}\,\Psi\left(\frac{1}{2} + \frac{\rho^+}{t_c}\right) \tag{2.36}$$

If $\rho^- = \left(\rho^+\right)^*$, it follows that $\rho^+ = \left(\rho^-\right)^*$, so that this equation can also be obtained with ρ^- instead of ρ^+. Thus, in the following the indices “+” and “-” will be omitted.

The pair breaking parameter can be written as $k_s^2 = 2\rho / \xi_S^2$ where $\xi_S = \left(D_S / 2\pi k_B T_{c0}\right)^{1/2}$ [**22**] is the superconducting coherence length. Introducing moreover $\phi = k_S d_s$, gives $\rho = k_S{}^2 \xi_s^2 / 2 = \phi^2 / \left[2\left(d_s / \xi_s\right)^2 \right]$. Thus,

$$\ln t_c = \Psi\left(\frac{1}{2}\right) - \mathrm{Re}\,\Psi\left(\frac{1}{2} + \frac{\phi^2}{2t_c (d_S / \xi_S)^2}\right) \tag{2.37}$$

To get $t_c=T_c/T_{c0}$, i.e. the critical temperature of the F/S/F trilayer from this equation, k_s, i.e. $\phi= k_s d_s$ must be known. To solve this problem, in the next step one will first find a solution of the Usadel equation in the superconductor, then apply the boundary condition, using the solution for the ferromagnetic region and get an equation from which ϕ can be found.

c) Now a solution of the Usadel equation, in the superconductor *i.e.* for Eq. (2.2) has to be found. Therefore, using again the Ansatz of Ref. [**21**] Eq. (3), however, now for Φ_s, that means $\Phi_s(x,\omega)=\dfrac{\Delta_S(x)}{\hbar\omega+2\pi k_B T_{c0}\rho(t)}$, in order to eliminate the energy gap in Eq. (2.2), one obtains the homogenous second order differential equation,

$$-\frac{d^2}{dx^2}\Phi_s=\frac{4\pi T_{c0}\rho(t)}{D_S}\Phi_s \tag{2.38}$$

with the following general solution

$$\Phi_s=c_1\cos(k_s x)+c_2\sin(k_s x) \tag{2.39}$$

For the interface between the right ferromagnetic layer and the superconductor a necessary boundary condition is, that the flux of charge across the boundary is conserved, *i.e.* no charge is created or annihilated by passing the interface [**36**], resulting in

$$N_S D_S\frac{d}{dx}\Phi_S(d_S,\omega)=N_{FR}D_{FR}\frac{d}{dx}\Phi_{FR}(d_S,\omega) \tag{2.40}$$

where N_S, N_{FR} and N_{FL} are the density of states (DOS) in the superconducting and right and left ferromagnetic layer, respectively. Inserting the pairing wave function Φ_{FR} and Φ_S into the boundary condition yields (using (2.40) with (2.39) and (2.17)).

$$\begin{aligned}&N_S D_S k_S\left[-c_1\sin(k_S d_s)+c_2\cos(k_S d_s)\right]\\&=-N_{FR}D_{FR}C_{FR}k_{FR}\sinh\left(k_{FR}d_{FR}\right)\end{aligned} \tag{2.41}$$

Rewriting Eq. (2.41) gives

$$-c_1\sin(k_S d_s)+c_2\cos(k_S d_s)=-C_{FR}\frac{N_{FR}D_{FR}k_{FR}}{N_S D_S k_S}\sinh\left(k_{FR}d_{FR}\right) \tag{2.42}$$

A further boundary condition for the interface between the right ferromagnetic layer and the superconducting layer is ([**22**] Eq. 3.5),

$$-D_{FR}\frac{\partial\Phi_{FR}}{\partial x}=\frac{v_{FR}T_{FR}}{2}\left(\Phi_S-\Phi_{FR}\right) \tag{2.43}$$

where D_{FR} is the diffusion coefficient. The negative sign arises, because the pair amplitude decreases from the superconducting layer into the right ferromagnetic region, thus giving a slope $\frac{\partial\Phi_{FR}}{\partial x}<0$. Moreover, T_{FR} is the transparency from the right ferromagnetic material into the superconductor. It is defined as $T_{FR/FL}=\int_0^1\frac{T(\cos\theta)}{1-T(\cos\theta)}d\cos\theta$, where θ is the angle between the normal to the interface and the trajectory of the Cooper pair. Here, $T(\cos\theta)$ is the quantum mechanical transmission coefficient. For $T(\cos\theta)=0$ one obtains $T_{FR/FL}=0$, which corresponds to a total reflection, while for a total transmission, $T(\cos\theta)\to 1$ so that $T_{FR/FL}\to\infty$.

Usually, there is always a finite transparency present, because the conduction bands of two materials never have exactly the same energy. At the interface between two metals the chemical potential will equalize. This is realized by a flow of electrons from one metal into the other, until the chemical potential is the same, leading to a potential step between the two materials. Hence, electrons passing the interface may be reflected due to this potential step. This shift is distinct at an S/F interface, because the spin sub bands of the ferromagnet are shifted due to the presence of the exchange field.

In Ref. [**22**] the boundary condition is stated as a hydrodynamic boundary condition. In this sense the jump of the pair amplitude at the interface, i.e. the difference $\left(\Phi_S-\Phi_{FR}\right)$ can be regarded as the height difference of fluids in two basins which are connected by a pipe. The transparency acts thereby as the transmissibility of the pipe.

Thus, inserting the pair amplitudes from Eqs. (2.16) and (2.39) into the boundary condition Eq. (2.43) yields,

$$\begin{aligned}&-k_{FR}D_{FR}C_{FR}\sinh\left[k_{FR}(x-d_s-d_{FR})\right]\Big|_{x=d_s}=\\&=\frac{v_{FR}T_{FR}}{2}\left\{c_1\cos(k_sx)+c_2\sin(k_sx)-C_{FR}\cosh\left[k_{FR}(x-d_s-d_{FR})\right]\right\}\Big|_{x=d_s}\end{aligned} \tag{2.44}$$

$$\begin{aligned}&k_{FR}D_{FR}C_{FR}\sinh(k_{FR}d_{FR})=\\&=\frac{v_{FR}T_{FR}}{2}\left\{c_1\cos(k_sd_s)+c_2\sin(k_sd_s)-C_{FR}\cosh(k_{FR}d_{FR})\right\}\end{aligned}\tag{2.45}$$

$$\begin{aligned}&c_1\cos(k_sd_s)+c_2\sin(k_sd_s)=\\&=C_{FR}\left[\frac{2k_{FR}D_{FR}}{v_{FR}T_{FR}}\sinh(k_{FR}d_{FR})+\cosh(k_{FR}d_{FR})\right]\end{aligned}\tag{2.46}$$

Dividing Equation (2.42) by (2.46) gives

$$\frac{c_1\sin(k_Sd_s)-c_2\cos(k_Sd_s)}{c_1\cos(k_Sd_s)+c_2\sin(k_Sd_s)}=\frac{C_{FR}\,\dfrac{N_{FR}D_{FR}k_{FR}}{N_SD_Sk_S}\sinh\left(k_{FR}d_{FR}\right)}{C_{FR}\left[\dfrac{2k_{FR}D_{FR}}{v_{FR}T_{FR}}\sinh(k_{FR}d_{FR})+\cosh(k_{FR}d_{FR})\right]}\tag{2.47}$$

Dividing at the left hand side by $\cos(k_Sd_s)$ and at the right hand side by $\cosh(k_{FR}d_{FR})$ one gets

$$(k_Sd_S)\frac{c_1\tan(k_Sd_S)-c_2}{c_1+c_2\tan(k_Sd_S)}=(d_s)\frac{\dfrac{N_{FR}D_{FR}k_{FR}}{N_SD_S}\tanh\left(k_{FR}d_{FR}\right)}{1+\dfrac{2k_{FR}D_{FR}}{v_{FR}T_{FR}}\tanh(k_{FR}d_{FR})}\tag{2.48}$$

To simplify the above equation, we introduce $\phi=k_Sd_s$ and a new parameter R_R

$$\phi\frac{c_1\tan(\phi)-c_2}{c_1+c_2\tan(\phi)}=R_R=(d_Sk_{FR})(\frac{N_{FR}D_{FR}}{N_SD_S})\frac{\tanh\left(k_{FR}d_{FR}\right)}{1+\dfrac{2k_{FR}D_{FR}}{v_{FR}T_{FR}}\tanh(k_{FR}d_{FR})}\tag{2.49}$$

In a similar way the solution for the left layer is obtained, using the boundary condition, (2.40), for the left side,

$$N_SD_S\frac{d}{dx}\Phi_S(-d_S,\omega)=N_{FL}D_{FL}\frac{d}{dx}\Phi_F(-d_S,\omega)\tag{2.50}$$

$$\begin{aligned}&N_SD_Sk_S\left[-c_1\sin(k_Sx)+c_2\cos(k_Sx)\right]\Big|_{x=-d_S}=\\&=N_{FL}D_{FL}C_{FL}k_{FL}\sinh\left[k_{FL}(x+d_S+d_{FL})\right]\Big|_{x=-d_S}\end{aligned}\tag{2.51}$$

$$\begin{aligned}&N_SD_Sk_S\left[c_1\sin(k_Sd_s)+c_2\cos(k_Sd_s)\right]=\\&=N_{FL}D_{FL}C_{FL}k_{FL}\sinh\left(k_{FL}d_{FL}\right)\end{aligned}\tag{2.52}$$

$$c_1 \sin(k_S d_s) + c_2 \cos(k_S d_s) = \frac{N_{FL} D_{FL} C_{FL} k_{FL}}{N_S D_S k_S} \sinh\left(k_{FL} d_{FL}\right) \qquad (2.53)$$

Now, we use the second boundary condition, Eq. (2.43), for the left side

$$+D_{FL} \frac{\partial \Phi_{FL}}{\partial x} = \frac{v_{FL} T_{FL}}{2} \left(\Phi_S - \Phi_{FL}\right) \qquad (2.54)$$

At the boundary condition between the left ferromagnetic layer and the superconductor the slope of the pairing wave function is positive and, thus, the diffusion coefficient has a positive sign.

$$\begin{aligned} & k_{FL} D_{FL} C_{FL} \sinh\left[k_{FL}(x + d_s + d_{FL})\right]\Big|_{x=-d_s} = \\ & = \frac{v_{FL} T_{FL}}{2} \left\{ c_1 \cos(k_s x) + c_2 \sin(k_s x) - C_{FL} \cosh\left[k_{FL}(x + d_s + d_{FL})\right]\Big|_{x=-d_s} \right\} \end{aligned} \qquad (2.55)$$

$$\begin{aligned} & k_{FL} D_{FL} C_{FL} \sinh(k_{FL} d_{FL}) = \\ & = \frac{v_{FL} T_{FL}}{2} \left\{ c_1 \cos(k_s d_s) - c_2 \sin(k_s d_s) - C_{FL} \cosh(k_{FL} d_{FL}) \right\} \end{aligned} \qquad (2.56)$$

$$\begin{aligned} & c_1 \cos(k_s d_s) - c_2 \sin(k_s d_s) = \\ & = C_{FL} \left[\frac{2 k_{FL} D_{FL}}{v_{FL} T_{FL}} \sinh(k_{FL} d_{FL}) + \cosh(k_{FL} d_{FL}) \right] \end{aligned} \qquad (2.57)$$

Dividing Equation (2.53) by (2.57) gives

$$\begin{aligned} & k_S d_S \frac{c_1 \sin(k_S d_S) + c_2 \cos(k_S d_S)}{c_1 \cos(k_S d_S) - c_2 \sin(k_S d_S)} = \\ & = \left(\frac{N_{FL} D_{FL}}{N_S D_S} \right) \left(k_{FL} d_S\right) \frac{\sinh\left(k_{FL} d_{FL}\right)}{\frac{2 k_{FL} D_{FL}}{v_{FL} T_{FL}} \sinh(k_{FL} d_{FL}) + \cosh(k_{FL} d_{FL})} \end{aligned} \qquad (2.58)$$

Dividing at the left hand side by $\cos(k_S d_S)$ and by $\cosh(k_{FL} d_{FL})$ at the right hand side, one obtains

$$k_S d_s \frac{c_1 \tan(k_S d_s) + c_2}{c_1 - c_2 \tan(k_S d_s)} = \left(\frac{N_{FL} D_{FL}}{N_S D_S} \right) \left(k_{FL} d_s\right) \frac{\tanh\left(k_{FL} d_{FL}\right)}{\frac{2 k_{FL} D_{FL}}{v_{FL} T_{FL}} \tanh(k_{FL} d_{FL}) + 1} \qquad (2.59)$$

The equation will be simplified by using again, $\phi = k_S d_S$ and introducing R_L

$$\phi\frac{c_1\tan(\phi)+c_2}{c_1-c_2\tan(\phi)}=R_L=\left(\frac{N_{FL}D_{FL}}{N_S D_S}\right)\left(k_{FL}d_s\right)\frac{\tanh\left(k_{FL}d_{FL}\right)}{\frac{2k_{FL}D_{FL}}{v_{FL}T_{FL}}\tanh(k_{FL}d_{FL})+1} \tag{2.60}$$

According to Eqs. (2.48) and (2.59) the expression for the right and left ferromagnetic layer, R_R and R_L , thus, are,

$$\phi\frac{\tan(\phi)-\frac{c_2}{c_1}}{1+\frac{c_2}{c_1}\tan(\phi)}=R_R \quad \text{and} \quad R_L=\phi\frac{\tan(\phi)+\frac{c_2}{c_1}}{1-\frac{c_2}{c_1}\tan(\phi)} \tag{2.61}$$

Introducing the constant $c=\frac{c_2}{c_1}$ and rearranging the above expressions one obtains

$$\frac{\tan(\phi)-c}{1+c\tan(\phi)}=\frac{R_R}{\phi} \quad \text{and} \quad \frac{R_L}{\phi}=\frac{\tan(\phi)+c}{1-c\tan(\phi)} \tag{2.62}$$

Solving for c in R_R

$$\begin{aligned}
&\tan(\phi)-c=\frac{R_R}{\phi}\left[1+c\tan(\phi)\right]\Leftrightarrow\\
&c\left[\frac{R_R}{\phi}\tan(\phi)+1\right]=\tan(\phi)-\frac{R_R}{\phi}\Leftrightarrow\\
&c=\frac{\phi\tan(\phi)-R_R}{R_R\tan(\phi)+\phi}
\end{aligned} \tag{2.63}$$

This solution for c can now be inserted into the expression for R_L, yielding

$$\frac{\tan(\phi)+\frac{\phi\tan(\phi)-R_R}{R_R\tan(\phi)+\phi}}{1-\frac{\phi\tan(\phi)-R_R}{R_R\tan(\phi)+\phi}\tan(\phi)}=\frac{R_L}{\phi} \tag{2.64}$$

Here (and already to get Eq. (2.63)) it has been assumed, that the expression $R_R\tan(\phi)+\phi$ is not zero. This assumption will be picked up later on. Rearranging the expression,

$$\tan(\phi)+\frac{\phi\tan(\phi)-R_R}{R_R\tan(\phi)+\phi}=\frac{R_L}{\phi}\left[1-\frac{\phi\tan(\phi)-R_R}{R_R\tan(\phi)+\phi}\tan(\phi)\right] \tag{2.65}$$

$$\begin{aligned}&\tan(\phi)\left[R_R\tan(\phi)+\phi\right]+\phi\tan(\phi)-R_R=\\&\frac{R_L}{\phi}\left[R_R\tan(\phi)+\phi-\phi\tan^2(\phi)+R_R\tan(\phi)\right]\end{aligned}\tag{2.66}$$

Simplifying the equation further,

$$\begin{aligned}&\phi\tan(\phi)\left[R_R\tan(\phi)+\phi\right]+\phi^2\tan(\phi)-\phi R_R=\\&R_LR_R\tan(\phi)+\phi R_L-R_L\phi\tan^2(\phi)+R_LR_R\tan(\phi)\end{aligned}\tag{2.67}$$

$$\begin{aligned}&\phi R_R\tan^2(\phi)+\phi^2\tan(\phi)+\phi^2\tan(\phi)-\phi R_R+\\&+R_L\phi\tan^2(\phi)-R_LR_R\tan(\phi)-R_LR_R\tan(\phi)-\phi R_L=0\end{aligned}\tag{2.68}$$

$$\begin{aligned}&\phi R_R\tan^2(\phi)+\phi^2\tan(\phi)-R_LR_R\tan(\phi)-\phi R_R+\\&+R_L\phi\tan^2(\phi)+\phi^2\tan(\phi)-R_LR_R\tan(\phi)-\phi R_L=0\end{aligned}\tag{2.69}$$

$$\begin{aligned}&\phi\tan(\phi)\left[R_R\tan(\phi)+\phi\right]-R_R\left[R_L\tan(\phi)+\phi\right]+\\&+\phi\tan(\phi)\left[R_L\tan(\phi)+\phi\right]-R_L\left[R_R\tan(\phi)+\phi\right]=0\end{aligned}\tag{2.70}$$

Finally,

$$\begin{aligned}&\left[\phi\tan(\phi)-R_L\right]\left[R_R\tan(\phi)+\phi\right]+\\&\left[\phi\tan(\phi)-R_R\right]\left[R_L\tan(\phi)+\phi\right]=0\end{aligned}\tag{2.71}$$

Equation (2.71) is a general and important corner stone, from which the solution for the parallel and antiparallel magnetization of symmetric and anti-symmetric trilayers can be derived. They will be discussed in the next sub chapters.

2.2.1. Parallel Magnetizations in Symmetric Trilayers

First, the case of the parallel magnetization of symmetric F/S/F trilayers will be considered. Symmetric trilayers means, that the thickness and all other physical properties, except the direction of the magnetization, of the ferromagnetic layers which sandwich the superconducting layer, are the same for both layers.

In the case of symmetric trilayers, with parallel magnetization, Eq. (2.71) is invariant under the exchange of the indices R and L, *i.e.* $R_L=R_R=R$, so that

$R_L + R_R = 2R$. To consider also the case that, although the trilayers are symmetric, they are different because of a parallel or antiparallel alignment of the magnetization directions of the ferromagnetic layers (in that case $R_L \neq R_R$), two expressions will be introduced which are, again $R_L + R_R = 2R$ and, moreover $R_L - R_R = 2\Lambda$. Thus, one may write

$$\begin{aligned} R_L + R_R &= 2R \qquad & 2R_L &= 2(R+\Lambda) \\ R_L - R_R &= 2\Lambda \qquad & 2R_R &= 2(R-\Lambda) \end{aligned} \tag{2.72}$$

$$\begin{aligned} R_L &= R+\Lambda \\ R_R &= R-\Lambda \end{aligned} \tag{2.73}$$

Introducing the above expressions into Eq. (2.71) yields

$$\begin{aligned} &\left[\phi\tan(\phi) - R - \Lambda\right]\left[(R-\Lambda)\tan(\phi)+\phi\right] + \\ &+\left[\phi\tan(\phi) - R + \Lambda\right]\left[(R+\Lambda)\tan(\phi)+\phi\right] = 0 \end{aligned} \tag{2.74}$$

rearranging,

$$\begin{aligned} &\left[\phi\tan(\phi) - R - \Lambda\right]\left[R\tan(\phi)+\phi-\Lambda\tan(\phi)\right] + \\ &+\left[\phi\tan(\phi) - R + \Lambda\right]\left[R\tan(\phi)+\phi+\Lambda\tan(\phi)\right] = 0 \end{aligned} \tag{2.75}$$

$$\begin{aligned} &\left[\phi\tan(\phi) - R\right]\left[R\tan(\phi)+\phi\right] - \Lambda\tan(\phi)\left[\phi\tan(\phi)-R\right] \\ &-\Lambda\left[R\tan(\phi)+\phi\right] + \Lambda^2\tan(\phi) + \left[\phi\tan(\phi)-R\right]\left[R\tan(\phi)+\phi\right] \\ &+\Lambda\tan(\phi)\left[\phi\tan(\phi)-R\right] + \Lambda\left[R\tan(\phi)+\phi\right] + \Lambda^2\tan(\phi) = 0 \end{aligned} \tag{2.76}$$

yielding,

$$2\left[\phi\tan(\phi) - R\right]\left[R\tan(\phi)+\phi\right] + 2\Lambda^2\tan(\phi) = 0 \tag{2.77}$$

and thus,

$$\left[\phi\tan(\phi) - R\right]\left[R\tan(\phi)+\phi\right] + \Lambda^2\tan(\phi) = 0 \tag{2.78}$$

In a first step, the parallel orientation of the magnetization of the two F-layers of the F/S/F trilayer will be considered, and Eq. (2.78) will be rewritten,

$$\left(\phi^P\tan\phi^P - R\right)\left(R\tan\phi^P + \phi^P\right) + \Lambda^2\tan\phi^P = 0 \tag{2.79}$$

The above equation can be further simplified, because in the case of symmetric trilayers with parallel magnetizations the physical properties of the two ferromagnetic layers are identical, *i.e.* $R_L - R_R = 0$ and thus $\Lambda = 0$ yielding,

$$\left(\phi^{P}\tan\phi^{P}-R\right)\left(R\tan\phi^{P}+\phi^{P}\right)=0 \tag{2.80}$$

During the derivation it has been assumed (see Eq. (2.64)), that $R\tan(\phi)+\phi$ is not zero, so that the final result for a symmetric trilayer with a parallel magnetization of both F-layers is:

$$\phi^{P}\tan(\phi^{P})-R=0 \tag{2.81}$$

This equation can also be derived, if S/F or F/S bilayers are considered. It is equal to the result obtained for a bilayer with the superconducting layer thickness divided by 2 as discussed in [**29**]. In this case one would, redefine $\phi=k_S d_S$, which was introduced in Eq. (2.37), and replace it by $\phi=k_S\tilde{d}_S$, where $\tilde{d}_S=d_S/2$.

2.2.2. Antiparallel Magnetization in Symmetric Trilayers

For the case of an antiparallel orientation of the magnetization in symmetric trilayers it is assumed, that the exchange field, which enters the equation via the superconducting coherence length in ferromagnetic layer (see Eq. (2.1)), reverses the sign, so that $iE_{ex}\rightarrow -iE_{ex}$. In Eq. (2.8) it was shown that the exchange field enters the wave vector over the condition, $k_F^2=iE_{ex}/D_F$. Thus, R_R can be rewritten in the following from

$$\phi\frac{c_1\tan(\phi)-c_2}{c_1+c_2\tan(\phi)}=R_R=(d_s\sqrt{\frac{iE_{ex}}{D_{FR}}})(\frac{N_{FR}D_{FR}}{N_S D_S})\frac{\tanh\left[\sqrt{\frac{iE_{ex}}{D_{FR}}}d_{FR}\right]}{1+\frac{2\sqrt{\frac{iE_{ex}}{D_{FR}}}D_{FR}}{v_{FR}T_{FR}}\tanh(\sqrt{\frac{iE_{ex}}{D_{FR}}}d_{FR})} \tag{2.82}$$

Reversing, the direction of the magnetization in the left ferromagnetic layer gives for R_L (considering that in the symmetric case all other parameters are equal)

$$\phi\frac{c_1\tan(\phi)-c_2}{c_1+c_2\tan(\phi)}=R_L=(d_s\sqrt{\frac{-iE_{ex}}{D_{FR}}})(\frac{N_{FR}D_{FR}}{N_S D_S})\frac{\tanh\left[\sqrt{\frac{-iE_{ex}}{D_{FR}}}d_{FR}\right]}{1+\frac{2\sqrt{\frac{-iE_{ex}}{D_{FR}}}D_{FR}}{v_{FR}T_{FR}}\tanh(\sqrt{\frac{-iE_{ex}}{D_{FR}}}d_{FR})} \tag{2.83}$$

From the last two equations one can see that the relationship between two ferromagnetic layers with opposite direction of the magnetization is given by $R_R = R_L^*$ where the star indicates the complex conjugate. This conclusion remains also valid, if we replace (see the discussion at the beginning of Chap. 2.2) D_F by $\widetilde{D}_F = D_F/(1 + il_F/\xi_{F0})$ with $\xi_{F0} = \hbar v_F/E_{ex}$.

Thus, assuming that a complex number can be decomposed in a real part R_1 and an imaginary part iR_2, that means $R_L = R_1 + iR_2$ Eq. (2.72) can be rewritten,

$$\begin{aligned} 2R &= R_L + R_R = R_L + R_L^* = R_1 + iR_2 + R_1 - iR_2 = 2R_1 = 2\,\mathrm{Re}(R_L) \\ 2\Lambda &= R_L - R_R = R_L - R_L^* = R_1 + iR_2 - R_1 + iR_2 = 2iR_2 = 2i\,\mathrm{Im}(R_L) \end{aligned} \tag{2.84}$$

Thus, for symmetric trilayers with anti-parallel magnetizations Eq. (2.79) reads,

$$\left(\phi^{AP}\tan\phi^{AP} - R\right)\left(R\tan\phi^{AP} + \phi^{AP}\right) + \Lambda^2\tan\phi^{AP} = 0 \tag{2.85}$$

Introducing Eq. (2.84) yields,

$$\left(\phi^{AP}\tan\phi^{AP} - R_1\right)\left(R_1\tan\phi^{AP} + \phi^{AP}\right) - R_2^2\tan\phi^{AP} = 0 \tag{2.86}$$

2.2.3. Asymmetric Trilayers

In the case of asymmetric trilayers, *i.e.* the ferromagnetic layer thickness is different in the right and left layer, all physical parameters in the left and right layers have different values, *i.e.* have to be distinguished. In the following the index *L* and *R* denote the left and right ferromagnetic layer, respectively. From Eqs. (2.49) and (2.60) one then gets,

$$R_L = \left(\frac{N_{FL}D_{FL}}{N_S D_S}\right)(k_{FL}d_s)\frac{\tanh\left[k_{FL}d_{FL}\right]}{1 + \dfrac{2k_{FL}D_{FL}}{v_{FL}T_{FL}}\tanh(k_{FL}d_{FL})} \tag{2.87}$$

$$R_R = \left(\frac{N_{FR}D_{FR}}{N_S D_S}\right)(k_{FR}d_s)\frac{\tanh\left[k_{FR}d_{FR}\right]}{1 + \dfrac{2k_{FR}D_{FR}}{v_{FR}T_{FR}}\tanh(k_{FR}d_{FR})} \tag{2.88}$$

For the case of the antiparallel magnetization the fact $R_R = R_L^*$ does not hold any more, but has a quite more complex relationship. In this case the much more complicated Equation (2.71) has to be solved.

2.2.4. Parameterization

Although, the system of equations has been solved, equations (2.37), (2.87) and (2.88) still contain too many variables which cannot be measured directly. Thus, the parameters have to be expressed in quantities which are physically measureable. These quantities are ξ_{BCS}, the Bardeen-Cooper-Schrieffer coherence length, and ξ_S, the coherence length in a dirty superconductor, which can be estimated from the critical field $B_{C2}(T)$.

Furthermore, the final expression contains parameters which have to be fitted by the theory. These are the ratio of the Sharvin conductances $N_F v_F / N_S v_S$, the interface transparency T_F, the coherence length of a ferromagnet ξ_F, and the mean free path of the electrons in the ferromagnet conduction band, l_F. However, the last two variables will appear as a ratio, ξ_F / l_F, in the final expression, reducing them effectively to one free variable.

Here, a version of the parameterization is used which was developed in November 2001 by L. Tagirov during his visit at the University of Augsburg [**39**]. The parameterization considers the case in which the magnetic material is in the clean case limit. The superconductor is always in the dirty limit.

In the case of F/S/F trilayers with a parallel magnetization in the symmetric case, Eq. (2.81) can be written in the following form,

$$\phi \tan(\phi) = \left(\frac{N_F D_F}{N_S D_S} \right) \left(d_S k_F \right) \frac{\tanh\left[k_F d_F \right]}{1 + \frac{2 k_F D_F}{v_F T_F} \tanh(k_F d_F)} \qquad (2.89)$$

Because $R = R_L = R_R$, we omitted the indices R and L in the equation. Moreover, the up script P of the quantity ϕ has not been used here.

First, the wave vector in the ferromagnetic region will be expressed in terms of l_F and ξ_{F0}, using the relationship $k_F^2 = \frac{iE_{ex}}{D_F}$ from Eq. (2.8) and furthermore the coherence length in the clean ferromagnet $\xi_{F0} = v_F / E_{ex}$.

Substituting the expression for the diffusion coefficient in the clean case limit, i.e. replacing D_F in Eq. (2.89) and, thus, also in the expression for the wave vector, by $\tilde{D}_F = D_F /(1+il_F / \xi_{F0})$, where $D_F = l_F v_F$, as discussed in the beginning of Chap. 2.2, yields

$$\begin{aligned} k_F &= \frac{\sqrt{iE_{exc}}}{\sqrt{l_F v_F}}\sqrt{1+i\frac{l_F}{\xi_{F0}}} = \sqrt{\frac{E_{exc}}{v_F}}\sqrt{\frac{1}{l_F}}\sqrt{i-\frac{l_F}{\xi_{F0}}} = \\ &= \sqrt{\frac{1}{\xi_{F0}}}\sqrt{\frac{1}{l_F}}\sqrt{i-\frac{l_F}{\xi_{F0}}} = \sqrt{\frac{\xi_{F0}}{\xi_{F0}^2 l_F}}\sqrt{i-\frac{l_F}{\xi_{F0}}} = \frac{1}{\xi_{F0}}\sqrt{i\frac{\xi_{F0}}{l_F}-1} \end{aligned} \qquad (2.90)$$

In a next step the dimensionless ratio $2k_F D_F / v_F T_F$ is parameterized, using the expressions for D_F, ξ_{F0} and k_F from above and the relationship between the coherence length in the clean ferromagnet, the exchange field and the Fermi velocity, $\frac{1}{\xi_{F0}} = \frac{E_{\mathrm{exc}}}{v_F}$

$$\begin{aligned} &\frac{2k_F D_F}{v_F T_F} = \frac{2}{T_F} D_F \frac{1}{v_F} k_F = \frac{2}{T_F}\frac{v_F l_F}{1+i\frac{l_F}{\xi_{F0}}}\frac{1}{v_F}\sqrt{\frac{iE_{\mathrm{exc}}}{v_F l_F}}\sqrt{1+i\frac{l_F}{\xi_{F0}}} = \\ &\frac{2}{T_F}\frac{l_F}{\sqrt{1+i\frac{l_F}{\xi_{F0}}}}\sqrt{\frac{i}{l_F\xi_{F0}}} = \frac{2}{T_F}\frac{\sqrt{i\frac{l_F}{\xi_{F0}}}}{\sqrt{1+i\frac{l_F}{\xi_{F0}}}} = \frac{2}{T_F}\frac{\sqrt{i\frac{l_F}{\xi_{F0}}}}{\sqrt{1+i\frac{l_F}{\xi_{F0}}}}\frac{\sqrt{-i\frac{\xi_{F0}}{l_F}}}{\sqrt{-i\frac{\xi_{F0}}{l_F}}} = \\ &= \frac{2}{T_F}\frac{1}{\sqrt{1-i\frac{\xi_{F0}}{l_F}}} \end{aligned} \qquad (2.91)$$

Finally, the last term for the parameterization is

$$\frac{N_F}{N_S}\frac{D_F}{D_S}k_F d_S = \frac{N_F}{N_S}(D_F k_F)\left(\frac{d_S}{D_S}\right) \qquad (2.92)$$

The terms in brackets on the right hand side, $(D_F k_F)$ and d_S/D_S, will be parameterized separately. The first term is,

$$D_F k_F = \frac{v_F l_F}{1+i\frac{l_F}{\xi_{F0}}}\sqrt{\frac{iE_{exc}}{l_F v_F}}\sqrt{1+i\frac{l_F}{\xi_{F0}}} = v_F \frac{l_F}{\sqrt{1+i\frac{l_F}{\xi_{F0}}}}\sqrt{i\frac{1}{l_F \xi_{F0}}} =$$

$$= v_F \frac{\sqrt{i\frac{l_F}{\xi_{F0}}}}{\sqrt{1+i\frac{l_F}{\xi_{F0}}}} = v_F \frac{1}{\sqrt{1-i\frac{\xi_{F0}}{l_F}}} \tag{2.93}$$

The second term is

$$\frac{d_S}{D_S} = \frac{d_S}{\frac{1}{3}v_S l_S} = \frac{1}{v_S}\frac{3d_S}{l_S} = \frac{3}{v_S}\frac{d_S}{\xi_{BCS}}\frac{\xi_{BCS}}{l_S} \tag{2.94}$$

On the right hand side of expression (2.94) the electron mean free path in the superconductor, l_S, cannot be measured directly. However, in a dirty superconductor, as which the superconductor will be always considered in the present theory, the mean free path of the conduction electrons enters the superconducting coherence length via the diffusion coefficient [**28**,**45**]

$$\xi_S^2 = \frac{D_S}{2\pi T_{c0}} = \frac{\frac{1}{3}v_S l_S}{2\pi T_{c0}} = \frac{v_S l_S}{6\pi T_{c0}} = \frac{l_S}{6}\frac{v_S \gamma}{\pi^2 T_{c0}}\frac{\pi}{\gamma} \tag{2.95}$$

Where, in the last step, the equation has been expanded with Euler's constant (C=0.5772), $\gamma = e^{0.5772} = 1.781$ [**46**], and π in order to introduce the BCS coherence length $\xi_{BCS} = \frac{\gamma v_S}{\pi^2 T_{c0}}$ (definition of Abrikosov-Gorkov-Dzyaloskiskii) [**28**,**45**,**47**], giving

$$\xi_S^2 = \frac{\pi}{6\gamma} l_S \xi_{BCS} \tag{2.96}$$

Now the desired relation between l_S, ξ_S and ξ_{BCS} has been obtained,

$$\frac{1}{l_S} = \frac{\pi}{6\gamma}\frac{\xi_{BCS}}{\xi_S^2} \quad \Rightarrow \quad \frac{\xi_{BCS}}{l_S} = \frac{\pi}{6\gamma}\frac{\xi_{BCS}^2}{\xi_S^2} \tag{2.97}$$

Equation (2.97) will be substituted into (2.94) which yields,

$$\frac{d_S}{D_S} = \frac{3}{v_S}\frac{d_S}{\xi_{BCS}}\frac{\pi}{6\gamma}\frac{\xi_{BCS}^2}{\xi_S^2} = \frac{1}{v_S}\frac{d_S}{\xi_S}\frac{\pi}{2\gamma}\frac{\xi_{BCS}}{\xi_S} \tag{2.98}$$

Equations (2.93) and (2.98) will be substituted into (2.92) giving,

$$\begin{aligned}\frac{N_F}{N_S}\frac{D_F}{D_S}k_F d_S &= \frac{N_F}{N_S}\frac{v_F}{\sqrt{1-i\frac{\xi_{F0}}{l_F}}}\frac{1}{v_S}\frac{\pi}{2\gamma}\frac{\xi_{BCS}}{\xi_S}\frac{d_S}{\xi_S} = \\ &= \frac{N_F v_F}{N_S v_S}\frac{\pi}{2\gamma}\frac{\xi_{BCS}}{\xi_S}\frac{d_S}{\xi_S}\frac{1}{\sqrt{1-i\frac{\xi_{F0}}{l_F}}}\end{aligned} \tag{2.99}$$

Finally, equations (2.90), (2.91) and (2.99) will be substituted into Equation (2.89), yielding

$$\begin{aligned}&\phi\tan(\phi) = \\ &= \frac{N_F v_F}{N_S v_S}\frac{\pi}{2\gamma}\frac{\xi_{BCS}}{\xi_S}\frac{d_S}{\xi_S}\frac{1}{\sqrt{1-i\frac{\xi_{F0}}{l_F}}}\frac{\tanh\left[\frac{d_F}{\xi_{F0}}\sqrt{i\frac{\xi_{F0}}{l_F}-1}\right]}{1+\frac{2}{T_F\sqrt{1-i\frac{\xi_{F0}}{l_F}}}\tanh\left[\frac{d_F}{\xi_{F0}}\sqrt{i\frac{\xi_{F0}}{l_F}-1}\right]}\end{aligned} \tag{2.100}$$

As it stands now, Eq. (2.100) has still too many free variables. However, from this expression the critical thickness of a symmetric trilayer (and S/F or equivalent F/S system) for which superconductivity vanishes for an infinite F-layer thickness can be found.

This will allow to impose a constraint on the parameters $N_F v_F / N_S v_S$ and T_F. For this purpose the expression has to be further simplified by considering an infinitely thick ferromagnetic layer in contact with a thin superconducting layer, then $\frac{d_F}{\xi_{F0}} \to \infty$ and the tangens hyperbolicus approaches one, simplifying Eq. (2.100) to

$$\phi\tan(\phi) = \frac{N_F v_F}{N_S v_S}\frac{\pi}{2\gamma}\frac{\xi_{BCS}}{\xi_S}\frac{d_S}{\xi_S}\frac{1}{\sqrt{1-i\frac{\xi_{F0}}{l_F}}}\frac{1}{1+\frac{2}{T_F\sqrt{1-i\frac{\xi_{F0}}{l_F}}}} \tag{2.101}$$

Furthermore, for strong ferromagnets, like cobalt, iron or nickel the coherence length is expected to be in the range of 7-10 Å, whereas the mean free path of the electrons in the ferromagnet is in the range of 25-40 Å [**39**]. Thus, $\frac{\xi_{F0}}{l_F} << 1$ and $i\frac{\xi_{F0}}{l_F}$ can be neglected, simplifying the expression further to

$$\phi\tan(\phi)=\frac{N_F v_F}{N_S v_S}\frac{\pi}{2\gamma}\frac{\xi_{BCS}}{\xi_S}\frac{d_S}{\xi_S}\frac{1}{1+\frac{2}{T_F}} \tag{2.102}$$

From the existence of a critical thickness d_S^{cr} at which superconductivity vanishes when it is in contact with a ferromagnet, a further constraint can be deduced, as will be discussed in the following. At the critical thickness it is $\phi^{cr}=k_S d_S^{cr}$ and the critical temperature is then given by Eq. (2.37), that means $\ln t_c=\Psi\left(\frac{1}{2}\right)-\operatorname{Re}\Psi\left(\frac{1}{2}+\frac{\rho^{cr}}{t_c}\right)$, where $\rho^{cr}=\frac{\phi^{2,cr}}{2\left(\frac{d_S^{cr}}{\xi_S}\right)^2}$.

Since Eq. (2.102) is real valued, the equation for the critical temperature can be rewritten as

$$\ln t_c=\Psi\left(\frac{1}{2}\right)-\Psi\left(\frac{1}{2}+\frac{\rho^{cr}}{t_c}\right) \tag{2.103}$$

Using from p. 258 and 259 of Ref. [**43**] that $\Psi\left(\frac{1}{2}\right)=-C-2\ln 2$ and $\Psi(z)$~ $\ln z-\frac{1}{2z}-\frac{1}{12z^2}+\ldots$ it follows

$$\ln t_c=-C-2\ln 2-\left[\ln\left(\frac{1}{2}+\frac{\rho^{cr}}{t_c}\right)-\frac{1}{2\left(\frac{1}{2}+\frac{\rho^{cr}}{t_c}\right)}-\ldots\right] \tag{2.104}$$

At the critical thickness "d_s^{cr}" the transition temperature vanishes, $t_c\to 0$, and the factor of ½ within the terms in bracket can be neglected, because $\frac{\rho^{cr}}{t_c}\gg\frac{1}{2}$ giving

$$\ln t_c=-C-2\ln 2-\ln\left(\frac{\rho^{cr}}{t_c}\right)+\frac{1}{\frac{2\rho^{cr}}{t_c}}+\ldots \tag{2.105}$$

Rearranging, yields

$$\ln t_c = -C - 2\ln 2 - \ln\left(\rho^{cr}\right) + \ln\left(t_c\right) + \frac{1}{\frac{2\rho^{cr}}{t_c}} - \ldots \tag{2.106}$$

Cancelling the $\ln t_c$ term and realizing that the last term, on the right hand side, vanishes if $t_c \to 0$ gives,

$$\begin{aligned} \ln\rho^{cr} &= -C - 2\ln 2 \\ \ln\rho^{cr} + \ln 4 &= -C \\ \ln\left(4\rho^{cr}\right) &= -C \end{aligned} \tag{2.107}$$

Simplifying leads finally to

$$\begin{aligned} 4\rho^{cr} &= e^{-C} \\ \rho^{cr} &= \frac{1}{4}e^{-C} = \frac{1}{4\gamma} = 7.124^{-1} \end{aligned} \tag{2.108}$$

Using the expression for ρ^{cr} from above and inserting it into the last equation, yields

$$\frac{1}{4\gamma} = \frac{\phi^{2,cr}}{2\left(\frac{d_S^{cr}}{\xi_S}\right)^2} \tag{2.109}$$

This gives an expression for ϕ^{cr} by rearranging,

$$\left(\phi^{cr}\right)^2 = \frac{1}{2\gamma}\left(\frac{d_S^{cr}}{\xi_S}\right)^2 \tag{2.110}$$

This solution is then substituted into Eq. (2.102), yielding

$$\sqrt{\frac{1}{2\gamma}}\frac{d_S^{cr}}{\xi_S}\tan(\phi^{cr}) = \frac{N_F v_F}{N_S v_S}\frac{\pi}{2\gamma}\frac{\xi_{BCS}}{\xi_S}\frac{d_S^{cr}}{\xi_S}\frac{1}{1+\frac{2}{T_F}} \tag{2.111}$$

$$\tan(\phi^{cr}) = \frac{N_F v_F}{N_S v_S}\frac{\pi}{\sqrt{2\gamma}}\frac{\xi_{BCS}}{\xi_S}\frac{1}{1+\frac{2}{T_F}} \tag{2.112}$$

$$\phi^{cr} = \arctan\left(\frac{N_F v_F}{N_S v_S} \frac{\pi}{\sqrt{2\gamma}} \frac{\xi_{BCS}}{\xi_S} \frac{1}{1+\frac{2}{T_F}} \right) \qquad (2.113)$$

Substituting again for $\phi^{cr} = \sqrt{\frac{1}{2\gamma}} \left(\frac{d_S^{cr}}{\xi_S} \right)$ yields an analytical solution for the critical thickness,

$$\frac{d_S^{cr}}{\xi_S} = \sqrt{2\gamma} \arctan\left(\frac{\pi}{\sqrt{2\gamma}} \frac{\xi_{BCS}}{\xi_S} \frac{\frac{N_F v_F}{N_S v_S}}{1+\frac{2}{T_F}} \right) \qquad (2.114)$$

Experimentally (therefore $\hbar = 1$ and $k_B = 1$ will not be used in the following) the critical thickness of the superconducting layer can be found by preparing a series of S/F bilayers with decreasing thickness of the superconducting material but a ferromagnetic layer of constant and “infinite” thickness (physically it should be much thicker than the coherence length ξ_F in the F-layer).

The superconducting coherence length, ξ_S, is connected with the Ginzburg-Landau coherence length $\xi_{GL}(0)$ [**48**] which can be determined by upper critical field measurements with the external field applied perpendicular to samples with solely a niobium layer. Close to T_{c0}, the upper critical field is given by $B_{c2}(T) = \frac{\Phi_0}{2\pi\xi_{GL}^2(0)}(1-\frac{T}{T_{c0}})$, where Φ_0 is the flux quantum [**48**]. From these measurements the Ginsburg-Landau coherence length can be calculated by, $\xi_{GL}(0)= [-(dB_{c2\perp}(T)/dT)(2\pi T_{c0}/\Phi_0)]^{-1/2}$. In a dirty superconductor the coherence length is ξ_S defined by [**21**,**49**] $\xi_S = (\hbar D_S/2\pi k_B\ T_{c0})^{1/2}$. Inserting the Bardeen-Cooper-Schrieffer coherence length $\xi_{BCS} = \hbar v_S\gamma/(\pi^2 k_B T_{c0})$ yields $\xi_S = \sqrt{(\pi/6\gamma)}\sqrt{(l_S\xi_{BCS})} = (2/\pi)\xi_{GL}(0)$, using that $\xi_{GL}^2(T) = 0.855(\xi_{BCS} l_S)^{1/2}(1-T/T_{c0})^{-1/2}$ [**48**].

From the slope of the $B_{c2\perp}(T)$ curve close to T_{c0} results for $\xi_{GL}(0)$ can be calculated yielding an experimental value for ξ_S. For Nb films with a thickness of d_{Nb}=6.8 *nm* and 14.0 *nm*, one gets $\xi_S = 6.16$ nm and $\xi_S = 6.68$ nm, respectively [**28**]. A value of ξ_{BCS} can be obtained from the literature, yielding

$\xi_{BCS} = 42nm$ [**50**]. Thus, the only not known variable in Eq. (2.114) is $(N_F v_F / N_S v_S)/(1+2/T_F)$, a value of which can, thus, be fixed by Eq. (2.114).

Finally, for the case of a symmetric trilayer with parallel magnetization of the ferromagnetic layers (now it is $\hbar = 1$ and $k_B = 1$ again), the major steps in fitting the theory for a sample to calculate $t_c = T_c / T_{c0}$, and, thus, the superconducting transition temperature, T_c, will be given. Starting with Eq. (2.37), the known parameters are, the measured T_{c0} of a free standing film of S-material used in the S/F or F/S bilayers or F/S/F trilayers (see Ref. [**28**] for Nb), which enters the quantity $t_c = T_c / T_{c0}$, the superconducting layer thickness d_S, which is obtained from RBS measurements, and the superconducting coherence length, ξ_S, which can be calculated from critical field measurements, as described above. Thus, the only remaining parameter is ϕ, which has be obtained by solving, Eq. (2.81),

$$\phi \tan(\phi) - R = 0 \tag{2.115}$$

where the index “P” has been omitted. However, since ϕ is complex valued, because $R = R_R = R_L$ is complex (see Eqs. (2.49) and (2.60) with (2.89) to (2.100)), *i.e.* $\phi = (\phi_1 + i\phi_2)$, this equation has to be rearranged, in order to separate the imaginary from the real part [**46**], giving

$$\begin{aligned}&(\phi_1 + i\phi_2)\tan(\phi_1 + i\phi_2) = \\ &= (\phi_1 + i\phi_2)\left[\frac{sin(2\phi_1)}{\cos(2\phi_1)+\cosh(2\phi_2)} + i\frac{\sinh(2\phi_2)}{\cos(2\phi_1)+\cosh(2\phi_2)}\right]\end{aligned} \tag{2.116}$$

Thus giving, by inserting Eq. (2.116) into (2.115)

$$\begin{aligned}&\phi_1\frac{sin(2\phi_1)}{\cos(2\phi_1)+\cosh(2\phi_2)} - \phi_2\frac{\sinh(2\phi_2)}{\cos(2\phi_1)+\cosh(2\phi_2)} - R_1 \\ &+i\left[\phi_1\frac{\sinh(2\phi_2)}{\cos(2\phi_1)+\cosh(2\phi_2)} + \phi_2\frac{\sin(2\phi_1)}{\cos(2\phi_1)+\cosh(2\phi_2)} - R_2\right] = 0\end{aligned} \tag{2.117}$$

Where R_1 and iR_2 are the real and imaginary parts of the right side of Equation (2.100) which is for convenience given again:

$$R=\frac{N_F v_F}{N_S v_S}\frac{\pi}{2\gamma}\frac{\xi_{BCS}}{\xi_S}\frac{d_S}{\xi_S}\frac{1}{\sqrt{1-i\frac{\xi_{F0}}{l_F}}}\frac{\tanh\left[\frac{d_F}{\xi_{F0}}\sqrt{i\frac{\xi_{F0}}{l_F}-1}\right]}{1+\frac{2}{T_F\sqrt{1-i\frac{\xi_{F0}}{l_F}}}\tanh\left[\frac{d_F}{\xi_{F0}}\sqrt{i\frac{\xi_{F0}}{l_F}-1}\right]} \qquad (2.118)$$

The separation of R in Eq. (2.118) into the real and imaginary part is best done by a computer program. The parameters for which a relation is known in the above equation are the ratio of the Sharvin conductances and the transparency, which has been obtained from critical thickness measurements of the superconducting layer, which fixes the ratio of $(N_F v_F / N_S v_S)/(1+2/T_F)$. Definitely known are only the thickness of the ferromagnetic layer d_F from RBS measurements and ξ_{BCS} , from the literature, and ξ_S calculated from critical field measurements. Thus, there a two completely free parameters left, ξ_F and l_F which can be chosen so that the above Eq. (2.117) is fulfilled. This has to be done by numerical methods.

3. Magnetron Sputtering

The samples for the present work have been provided by Vladimir Zdravkov, who fabricated them at the Institute of Electric Engineering and Nanotechnologies of the Academy of Sciences of Moldova in Kishinev. He prepared the samples by magnetron sputtering using a “Leybold Z400” vacuum system at room temperature. Sputtering was performed under an Argon (99.999%, “Messer Griesheim”) atmosphere of $p_{Ar} \approx 8 \cdot 10^{-3} mbar$ with a residual pressure in the sputtering chamber of about $p_{Ar} = 2 \cdot 10^{-6}$ mbar. The substrate was a commercially available silicon substrate, usually with (111) orientation, with dimension 80 x 7mm^2. In total four different targets have been used, niobium with a purity of 99.99 %, silicon (99.999 %), cobalt (99.95 %) and a copper nickel alloy with 60 at. % nickel and 40 at. % copper.

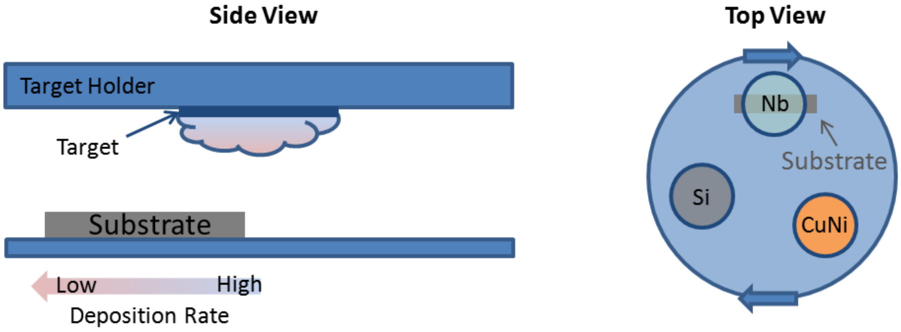

Fig. 3.1: Overview of the sputtering process. a) The Target is static to deposit a wedge structure. b) The target holder is moving in a circle over the substrate, depositing a layer of constant thickness.

In order to remove any contaminations, *e.g.* adsorbents, from the targets they were 3-5 minutes pre-sputtered, where niobium has been cleaned in a last step, because Nb acts as a getter material, *i.e.* it reduces the residual gas pressure in the chamber. The Nb was dc-sputtered, whereas the silicon and copper nickel target where rf-sputtered. Usually, the concentration in the resulting ferromagnetic alloy layer is 41 at. % Cu and 59 at. % Ni, i.e. a $Cu_{41}Ni_{59}$ layer is obtained.

Two different types of geometries have been prepared, layers with a constant thickness and layers with a wedge structure. In order to prepare a wedge structure, the natural sputtering gradient has been used, as shown in Fig. 3.1. Therefore, the substrate was placed 5 cm off-axis of the middle of the target under the magnet. The deposition rate is, thus, decreased considerably for the part of the substrate which is not placed below the target. For the deposition of layers with a constant thickness, the target was moved over the substrate in a circle path. For this propose, the target holder was moved during the deposition process. This was done in order to avoid thickness inhomogeneities, arising from, e.g., the magnet which is placed above the target, in a magnetron sputtering system. When the target is moved in this way, the growth rate of the thin film is significantly reduced. For niobium the steady state growth rate would be 4nm/s while the actual growth rate is 1.3nm/s. After the sputtering process the substrate was cut perpendicular to its longer side into about 30 samples of equal width of about 2.5mm.

3.1. Bilayers

In order to find the oscillations of the critical temperature as a function of the F-layer thickness, as predicted by theory (see Chap. 2), two types of samples have been produced. For both kinds of samples first a thin film of amorphous silicon has been sputtered on top of the substrate, in order to achieve a homogenous and flat surface.

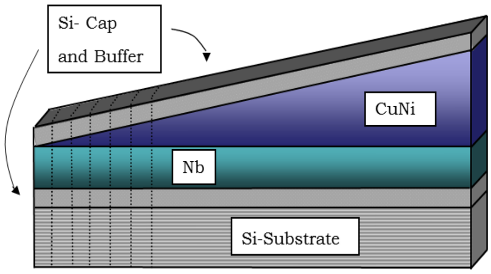

Fig. 3.2: Sketch of a wedge type geometry, a so called S/F structure, if seen from the bottom, to get a series of S/F samples.

In Fig. 3.2 the situation is sketched where a flat layer of niobium with constant thickness has been deposited followed by a wedge of copper nickel. This structure is called an S/F geometry, because beginning from the substrate first the superconductor and then a ferromagnet has been deposited. On top of the stack of layers a silicon cap has been sputtered in order to protect the layers from ambient conditions. With this kind of geometry the sample series, S15, S16, S21, S22 and S23 have been produced.

Next, an F/S layered structure has been grown, where now the superconductor is deposited on top of the ferromagnet, which is shown in Fig. 3.3.

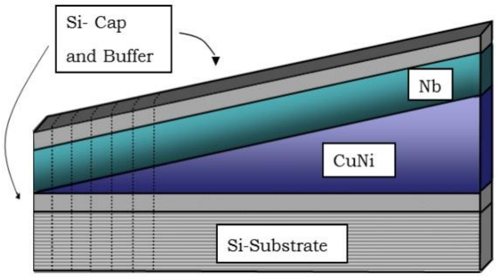

Fig. 3.3: Sketch of the wedge type geometry to get a series of F/S samples.

This kind of geometry, with which sample series FS233, FS2406, and FS712 were fabricated, is mirror symmetric to the S/F one discussed above.

Both geometries, the F/S and S/F one, can be regarded as building blocks of a F/2S/F spin valve core structure. It is not expected, that with the same settings during the sputtering process, the same behavior of the critical temperature can be observed for S/F and F/S bilayers. The reason for such deviations is that in the second case the copper-nickel alloy grows on the amorphous silicon buffer and the niobium on top of the copper-nickel alloy, whereas in the first geometry the niobium is grown on the Si buffer and the copper nickel alloy, on crystalline niobium. Furthermore, the substrate temperature is affected by the heat conductivity of the underlying material, which is different in the S/F and F/S case and may lead to a different growth or interface transparency.

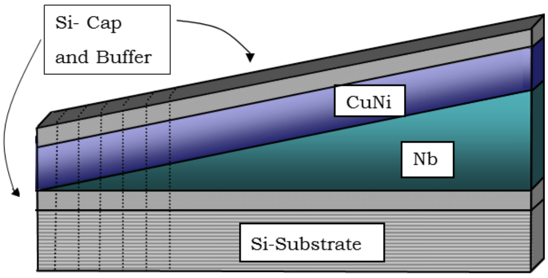

Fig. 3.4: A niobium wedge with a constant layer of copper nickel on top of it.

The third kind of geometry which has been deposited is shown in Fig. 3.4. It is a niobium wedge with a thick (“physically infinite”, see Chap. 2) layer of ferromangetic alloy on top of it. This geometry was sputtered in order to determine the critical thickness, at which superconductivity vanishes for decreasing Nb thickness. The sample series which have been prepared in this way were WNb with a ferromagnetic thickness, determined by Rutherford Backscattering Spectrometry, of d_{CuNi}=56 nm and the series WNc with d_{CuNi}=25 nm.

In addition to this S-wedge/F-constant geometry, an F-constant/S-wedge structure was sputtered, where the infinite thick ferromagnetic alloy layer has been placed below the superconducting layer. The sample series for this structure is called FSW3 with an average thickness of the copper-nickel layer of d_{CuNi}=18 nm.

3.2. Trilayers

After having successfully produced the bilayers, the next structure which had to be sputtered was the spin valve core structure, a trilayer, consisting of a niobium layer which is enclosed by two ferromagnetic layers. Two different kinds of samples have been prepared, which are shown in Fig. 3.5 and Fig. 3.6.

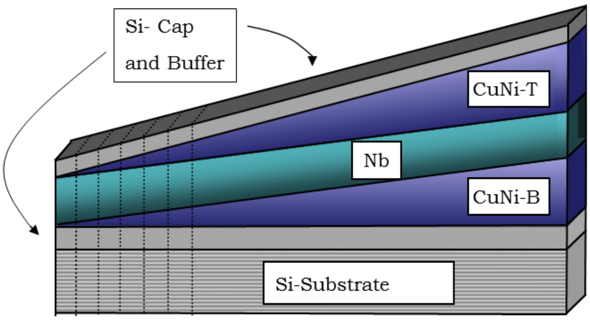

Fig. 3.5: The F/S/F double wedge geometry consist of two copper-nickel wedges which enclose a niobium wedge

The first one is a double-wedge geometry, which means that the niobium layer is enclosed by two ferromagnetic wedges, see Fig. 3.5.

The second one, shown in Fig. 3.6, is a single wedge geometry, which means that the niobium layer is deposited on a layer of constant thickness of the ferromagnetic alloy, whereas on top of the niobium layer a ferromagnetic wedge was grown.

In the single-wedge geometry sample series FSF 1 and FSF 2 have been prepared. For series FSF 3 and FSF 5 the double-wedge technique has been applied.

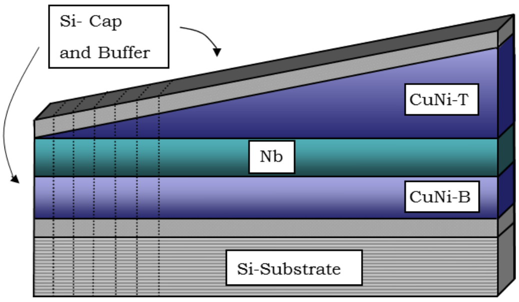

Fig. 3.6: The second kind of trilayer sample has a single wedge geometry, i.e. a constant layer of copper nickel on top of the substrate and a copper nickel wedge on top of the niobium.

3.3. Spin Valve

The basic principle of a spin valve is to have a structure which allows the fixing of the orientation of the magnetization of one of the ferromagnetic layers with respect to the other one under certain magnitudes of an externally applied magnetic field. One of the possibilities to achieve this, is the introduction of an antiferromagnetic (AF) pinning layer.

By applying an external field, the magnetization of the second ferromagnetic layer can then be reoriented, while the first one is kept fixed. As antiferromagnetic material we decide to use cobalt oxide. The antiferromagnetic cobalt oxide layer can be placed either on top of the upper $Cu_{41}Ni_{59}$ layer or below the bottom $Cu_{41}Ni_{59}$ layer.

Since the Leybold “Z400” sputtering system allows only three targets to be simultaneously mounted in the sputtering chamber, the sputtering procedure for the two possibilities is different. If the cobalt oxide layer is placed at the bottom, first a Si-buffer layer is deposited and afterwards the cobalt oxide layer.

Then the target holder has to be removed from the sputtering chamber (breaking the vacuum) and the cobalt target has to be replaced by a target of $Cu_{40}Ni_{60}$ or Nb. Afterwards the sputtering chamber has to be evacuated again and the targets are pre-sputtered, in order to remove any surface contaminations. Then the two ferromagnetic layers and in between the superconducting layer have to be deposited. Finally the multilayer system is protected with the silicon cap.

If the cobalt oxide layer is placed on top of the F/S/F system, the silicon buffer layer and the cap layer are omitted, because then the four layer system can be sputtered in one run. In this case the cobalt oxide layer deposited is sufficiently large in order to protect the niobium and $Cu_{41}Ni_{59}$ layers.

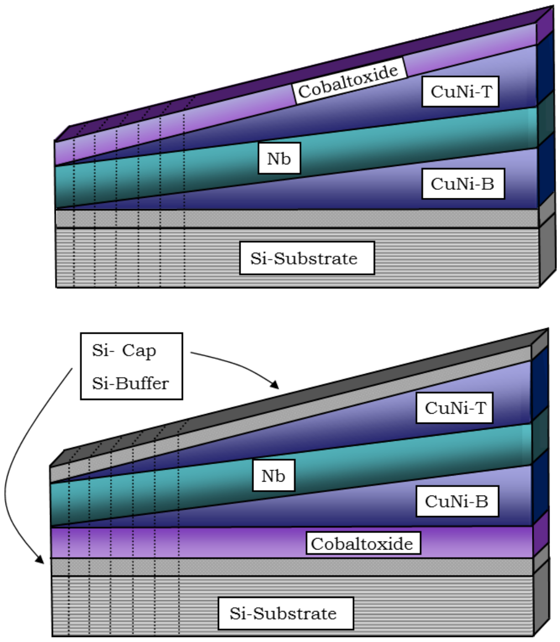

Fig. 3.7: Sketch of the spin valve structure. The direction of the magnetization of the ferromagnetic $Cu_{41}Ni_{59}$ alloy can be pinned by the introduction of an antiferromagnetic cobalt oxide layer, which can be either placed above (top figure) or below (bottom figure) one of the ferromagnetic layers. In the last case there is no Si-cap and buffer layer.

The series where the antiferromagnetic layer is on top of the stack are denoted by FSF-AF1 and FSF-AF2. The difference between the antiferromagnetic layers in these two series are, that for the FSF-AF1 series the substrate was kept at room temperature, whereas for the FSF-AF2 series the substrate temperature was heated to 300°C in order to influence the growth of the cobalt oxide layer. For the sample series where the antiferromagnetic layer was placed onto the silicon substrate, series AF-FSF5a has been also heated to 300°C whereas for the AF-FSF5b series it was kept at room temperature. Moreover, the series AF-FSF4 was fabricated at room temperature. In Fig. 3.7 the cobalt oxide layer is shown in purple.

3.4. Further Structure

One further structure has been prepared, which is shown in Fig. 3.8. The multilayer system was made in order to study the magnetic properties of the diluted ferromagnetic alloy layer.

The magnetic measurements were done in a highly sensitive Superconducting Qunatum Interference Device (SQUID) magnetometer (see Chap. 6). However, due to the dilution of the ferromagnet nickel into a copper matrix and, furthermore, due to the small thickness of the films of order of a few nanometers, the signal arising from the magnetic moment of the individual layer is very low.

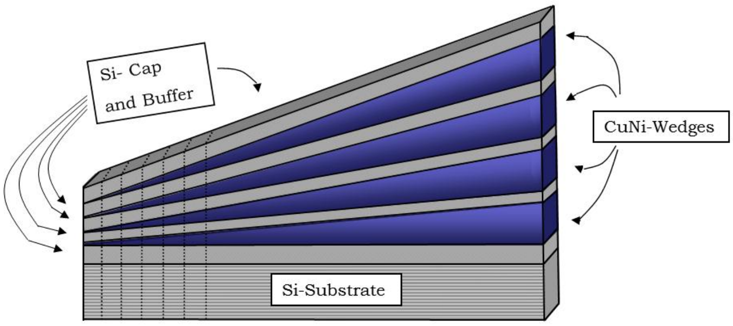

Fig. 3.8: The sample series WCN21, consiting of four $Cu_{41}Ni_{59}$ wedges which are separated by silicon buffer layer.

In order to increase the signal, a multilayer structure, consiting of four ferromagnetic layers has been prepared. To decouple the individual magnetic layers from each other, they have been separated by silicon buffer layers with a thickness of 10 nm. Moreover, a wedge technique is applied, to get a sample series (cut from the wedge perpendicular to the thickness gradient) with increasing thickness of the magnetic film. With this approach it is possible to study the magnetic properties of the ferromagnetic layer as a function of its thickness. Such thickness dependence arises possibly from ansiotropies or from nickel precipitions over the wedge, resulting in a different saturation magnetization.

4. Thickness and Composition Characterization by Rutherford Backscattering Spectrometry

The thickness and chemical composition of layers in the nanometre regime can be determined by Rutherford Backscattering Spectrometry (RBS) [**51**]. In this method, He^{++} ions accelerated to an energy of 3.5 MeV by a tandem accelerator and hit the sample. Some of these α-particles are backscattered from its atoms. The helium ions either scatter elastically, for instance when a collision with the target atoms happens, or inelastic when the helium ions passes the electron clouds of the target material.

The elastic energy loss of these particles is given by the k-factor, which describes the energy loss of an incident Helium particle, $E_{Inc}k = E_{Scat}$, where E_{Inc} is the incident energy of the α-particles and E_{Scat} is the energy of the backscattered particles. The k-factor is a function of the exit angle θ, the mass M_1 of the scattered α-particle and the mass M_2 of the scattering atom. The largest change in the projectile energy, before and after the collision, is for $\theta = 180°$, i.e. into the direction of the incident beam. However, at this angle the detector cannot be located. In the current measurements θ was 170° with respect to the incident beam which means that the angle between the incident beam and the reflected beam was 10°. Due to the larger energy loss of the helium ions, the determination of the thickness of the target material is most precise for light elements [**52**]. This fact is illustrated in Fig. 4.1 where the k-factor is shown as a function of the atomic mass. The equation given below the curve is the expression for the k-factor. Thereby the energy E, mass M, and velocity v, of the incident particle have the index *1* while the target particle has index *2*. It can be derived by considering the conservation of energy and momenta before and after the collision of two particles with mass M_1 and M_2 and exit angle θ and β, respectively, where β is the recoil angle of the scattering atom [**53**].

The kinematic factor *k*, *i.e.* the ratio of the energies of the incoming α-particle before and after scattering, is a function of only three variables, the particle and target atoms mass and the scattering angle. In the present case, the samples were build-up of a combination of silicon, cobalt, oxygen, nickel, copper and niobium.

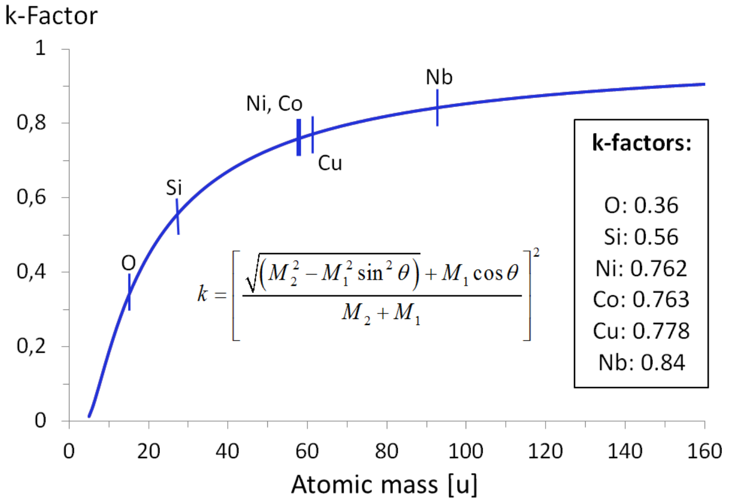

Fig. 4.1: The ratio of the energies of the backscattered and incoming helium atoms is known as the kinematic factor k. The curve shows the k-factor as a function of the atomic mass of the target material. The k-factors used in the present investigations is given in the inset. The k-factors of nickel, copper and cobalt are very close together.

In Fig. 4.1 the *k*-factors of these elements are given. While most of the shown elements have large differences in the *k* values, cobalt and nickel have similar values. Assuming an incoming particle energy of 3.5 MeV, the peak in the energy spectrum of a cobalt layer at the surface would be expected to begin at an energy of 2.670 MeV while that of a nickel would appear at 2.667 MeV, as calculated from the equation of the k-factor and given as the inset in Fig. 4.1. The difference in both peaks is well below the detector resolution of ±9 keV, of the semiconductor detector, making it impossible to distinguish both elements in a spectrum.

However, if a cobalt and nickel layer would be separated by a sufficiently thick intermediate layer, it may be possible to distinguish both layers, because there is an additional energy loss of the helium ions during the passage through this layer. This inelastic energy loss is due to the excitation of electrons into excited states or the ejection of electrons from the atom. Considering both the elastic and inelastic scattering of the α-particles, the thickness of the layers can be determined [**52**]. During the measurement the sample was azimuthally tilted by a small angle of 7° in order to prevent channelling effects [**53**].

4.1. Fitting Procedure for Thin Films

4.1.1. Bilayers

The bilayers of the present work have two different geometries. In the first type (S/F bilayers) the copper-nickel alloy layer is placed on top of the niobium layer, whereas in the second one (F/S bilayers) both layers are interchanged. In the RBS spectrum this will lead to a small energy shift of the peaks, because in the case of S/F layers, the peak of the superconducting layer will be shifted to lower energies compared to the F/S layer due to the inelastic energy loss of the helium ions during the passage through the ferromagnetic layer. In the case of F/S layers, the peak arising from the ferromagnetic layer will be shifted to a lower value compared to S/F layers due to the energy loss during the passage through the superconducting layer. However, the overall peak structure will be similar in both cases because the inelastic energy loss in thin film layers is expected to be small.

With an incident energy of the helium atoms of 3500 keV, the individual peaks of copper, nickel and niobium can be distinguished. From Fig. 4.2 the peak positions can be determined to be at a value of 2591 keV and 2532 keV for Cu and Ni, respectively. While copper and nickel overlap, the niobium peak is located at a higher energy of 2845 keV.

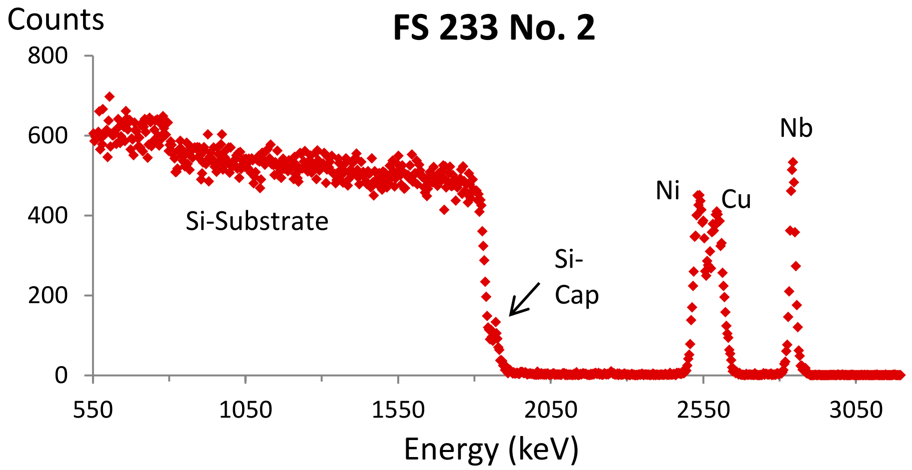

Fig. 4.2: RBS measurement of the bilayer No. 2 of sample series FS 233. With incident energy of 3.5 MeV of the He^{++} ions the copper and nickel peak arising from the ferromagnetic $Cu_{41}Ni_{59}$ layer can be clearly distinguished.

In order to prevent the bilayers from oxidization, the bilayers of copper-nickel and niobium are protected by a silicon cap. The two silicon layers, *i.e.* the silicon cap and the substrate, can just be distinguished if the intermediate layers ($Cu_{41}Ni_{59}$ and Nb) are thick enough for a sufficient energy loss of the He^{++}. The helium ions backscattered from the top layer of the silicon cap protection layer will have an energy of about 1960 keV, which is the energy of the incident ions (3.5 MeV) times the *k*-factor of silicon. The backscattered helium atoms from the substrate will have an energy of 1960 keV-ΔE where ΔE, is the energy loss due to the interaction of the α-particles with the electrons clouds of the atoms on the copper-nickel and niobium layer.

To distinguish the silicon substrate from the silicon cap, the intermediate copper-nickel and niobium layer have to be sufficiently thick in order to lead to an energy loss which can be detected.

In the case of bilayers, the atomic concentration of the copper nickel layer can also be determined. This can be seen by considering the scattering yield of, e.g., a copper-nickel alloy, with increasing copper concentration. For a high nickel and lower copper atomic concentration, the peak of the sputtering yield of nickel will be much higher than that of the copper. By increasing the copper concentration further, the nickel peak will decrease whereas the copper peak increases. So, the ratio of the peak height of the sputtering yields of copper and nickel gives a relationship between the atomic concentrations of copper and nickel. However, the ratio has to be corrected for the different scattering cross sections of the two elements in the alloy, because different elements have different scattering cross section [**53**].

The measured RBS spectra can be simulated by computer programs like RUMP [**54**], or SIMNRA [**55**] for a given specimen structure, and fitted to the measured spectra. From the resulting elemental areal densities of the elements in the sample (*e.g.* Nb, cu, Ni), the thickness of the layers (here Nb, copper-nickel alloy) can be calculated, considering the densities of the respective materials, and usually also the alloy concentrations (here of the copper-nickel alloy) is obtained.

In Fig. 4.3 the results of the RBS measurement of series FS 233 is given. The niobium layer (red diamonds) has an average thickness of 7.7 nm. The maximum and minimum values are 8.1 nm and 7.4 nm, respectively. For the $Cu_{41}Ni_{59}$ layer (blue squares), for low sample numbers the thickness first stays constant and then the thickness decreases monotonously from 31.9 nm to 0.9 nm, for samples No. 5 to No. 32, respectively. At the top of the figure the green circles give the nickel concentration in the copper-nickel alloy layer. The average concentration is $Cu_{41}Ni_{59}$, which is close to that one of the sputtering target.

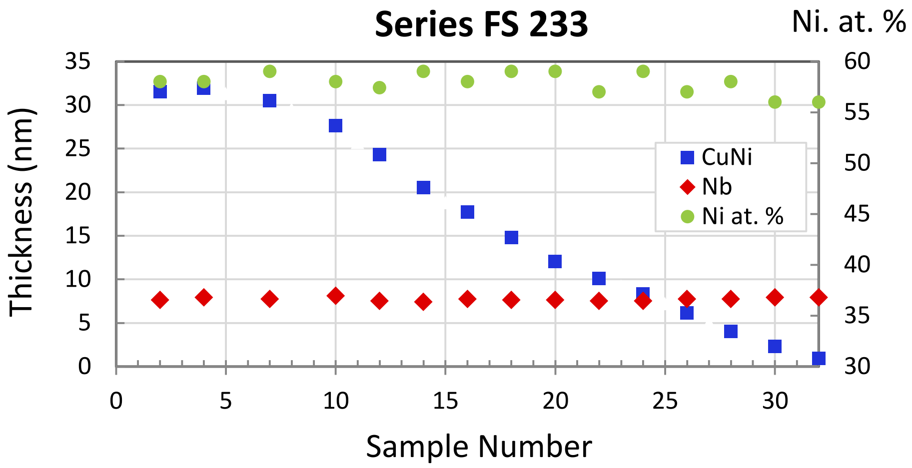

Fig. 4.3: Thickness of the copper-nickel and Nb films of the bilayer series FS 233, measured with RBS. The variation in the Ni concentration is given on the right x-axis.

4.1.2. Trilayers

In Fig. 4.4 the RBS spectrum of sample FSF3 No. 1 is shown. Similar to the spectrum of a bilayer, the niobium peak is above 2800 keV and the silicon cap is at an energy of 1960 keV. However, in the case of three layers, the signal coming from the Si-Buffer/Substrate is shifted more to lower energies, because the three intermediate layers give rise to a larger inelastic energy loss of the He-ions. The superposition of peaks in the energy range from 2500 keV to 2800 keV arises from a combined signal from the top and bottom ferromagnetic layers. In Fig. 4.1 it is shown, that copper has a higher k-value than nickel, because its atomic mass is larger compared to that one of nickel. Therefore, the beginning of the copper peak will be always situated at a higher energy than the nickel peak.

Both ferromagnetic layers are separated by the niobium layer, which gives an additional energy loss of the He^{++} particles passing it. This means, that in an RBS spectrum the α-particles which are backscattered from the copper and nickel atoms in the bottom ferromagnetic alloy layer are shifted to lower energies compared to those in the top one.

Thus, in Fig. 4.4 the signal coming from the top ferromagnetic alloy layer is the nickel in the large peak and the copper is located at its “right” shoulder. The energies of the α-particles coming from the copper and nickel of the bottom alloy layer have an energy which is shifted by about $\Delta E = 60$ keV, which is equal to the energy spread of a copper-nickel alloy layer in a bilayer (see Chap. 4.1.1) for an incident particle energy of 3500 keV. Thus, the α-particles which are backscattered from the nickel atoms in the top alloy layer have about the same energy as those coming from the copper atoms in the bottom alloy layer, giving rise to a common peak at about 2640 keV. The left “shoulder” of this peak arises from particles which have been backscattered from the Ni atoms in the bottom alloy layer.

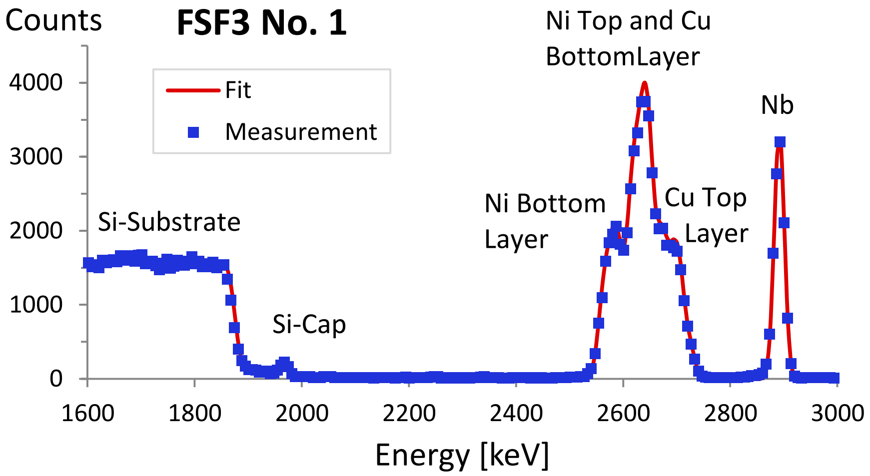

Fig. 4.4: Rutherford Backscattering Spectrum of sample FSF 3 number 1. The peak between 2500 keV and 2800 keV results from the measurement signals from the top and bottom ferromagnetic layer. The peak above 2800 keV arises from the niobium layer.

The fitting procedure for the trilayer is that the layer thickness will be determined subsequently from the top layer to the bottom layer. First of all, the silicon cap is fitted. In order to separate the signals arising from the cap and from the substrate, the sample is chosen, where the intermediate F/S/F layers are thickest to produce the largest inelastic energy loss during the passage through the sample.

Simulating the thickness of both ferromagnetic layers is difficult, because the left side of the copper top peak is overlapped with the signal coming from the Ni in the top ferromagnetic layer and copper in the bottom ferromagnetic layer. However, it is possible to fit the thickness of the top ferromagnetic layer by adjusting the right side of the niobium peak, since this peak position is determined by the thickness of the layers above, *i.e.*. the silicon cap and the top ferromagnetic layer. The reason is that the energy of the α-particles which are (back-)scattered at the top of the Nb layer can be written as $E_{Nb} = \left[3500keV - \Delta E^{Si}(d_{Si}^{cap}) - \Delta E^{CuNi}(d_{CuNi})\right] \cdot k_{Nb}$, where ΔE is the energy loss by passing through a thickness d_{Si}^{cap} of the Si cap and d_{CuNi} of the copper-nickel layer [**53**]. During the way out of the sample the α-particles pass again the top ferromagnetic layer and the Si cap and experience an additional energy loss. Next, the thickness of the niobium layer is determined by adjusting the half width of the niobium peak. The last layer which has to be simulated is the bottom ferromagnetic layer. The thickness of this layer can only be determined by adjusting the peak arising from the Nickel atoms in the bottom ferromagnetic layer, because the peak of the copper atoms of this alloy layer overlap in the spectrum with the one of the nickel atoms in the top alloy layer.

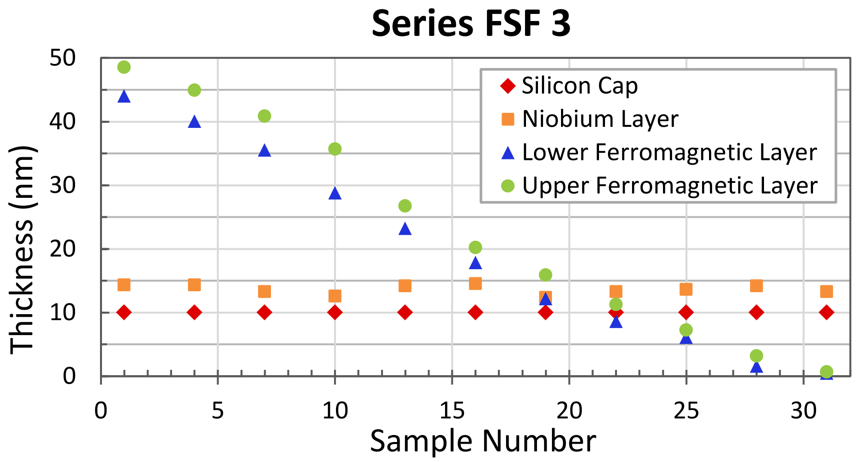

Fig. 4.5: Thickness determined by RBS of the nanolayers of the "double wedge geometry" trilayer series FSF3.

Thus, the thickness of the bottom ferromagnetic layer can be fitted to the RBS measurement points below the left shoulder of the large $Cu_{41}Ni_{59}$ peak. Furthermore, if the thickness of the bottom ferromagnetic layer has been correctly determined, the signal due to the Ni-top and Cu-bottom atoms should have been fitted with the correct amount of counts.

In Fig. 4.5 an overview over the thickness determination via RBS of the FSF3 series is given. The average thickness over all measured RBS data points for the Nb layer is 13.6 nm with minimum and maximum values of 2.6 nm and 14.3 nm. The FSF3 series has been cut from a F/S/F double wedge geometry with two $Cu_{41}Ni_{59}$ wedges which have nearly the same thickness. They start from nearly the same inital thickness, *i.e.* 48 nm and 44 nm, at the thick side for the top and bottom layer, respectively, and decay with nearly the same slope. Both wedges decrease monotonously to zero. The nickel content in the copper-nickel alloy layers has not been fitted, but kept constant at 59 at. % over the wedge, because the overlap of the structures in the RBS spectrum would make the results not reliable.

If the thickness of the niobium layer is very small, the peak overlap is even stronger, compared to the series FSF3, discussed above. In Fig. 4.6 the RBS spectrum of sample 2 of the single wedge trilayer series FSF1 is shown.

The average thickness of the niobium layer of sample series FSF3 is around 10 nm (see Fig. 4.7) and, thus, the energy loss of the helium ions during the passage through this layer is small, so that the separation of the signals of both ferromagnetic layers is small, as discussed above. Because the copper peak of the bottom ferromagnetic layer is overlapped by the signal from the upper copper nickel layer, it is hard or even not possible to fit this element for the bottom alloy layer.

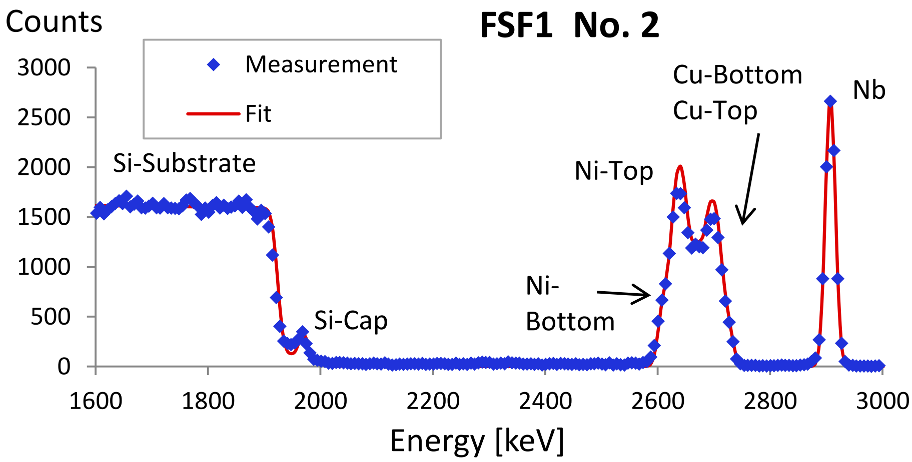

Fig. 4.6: RBS spectrum of sample FSF1 No. 2. Due to the fact, that the niobium layer is so thin (only 10 nm), the ferromagnetic peaks cannot be resolved anymore.

However, the thickness can be determined from High Resolution Transmission Electron Microscopy (HRTEM) images. Furthermore, at the left side of the nickel peak from the top alloy layer, there is again a slight shoulder arising from the lower ferromagnetic layer, which could be adjusted by the fitting.

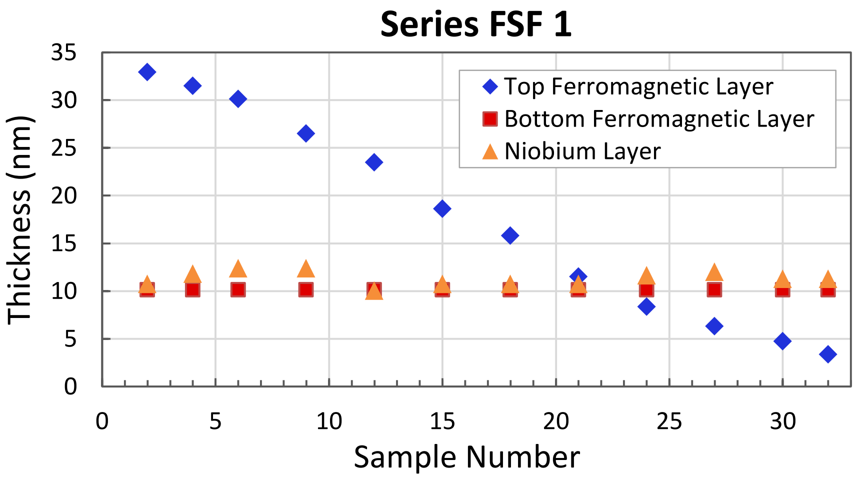

Fig. 4.7: The thickness obtained from the RBS measurement for the single wedge geometry series FSF 1. The thickness of the bottom ferromagnetic layer was determined by TEM analysis and set constant over the series.

The RBS analysis for the complete FSF1 series is given in Fig. 4.7. The average thickness of the lower ferromagnetic alloy layer was determined from TEM measurements and set to a constant value of 10.2 nm over this single wedge geometry series. The niobium layer has an average value of 11.3 nm, deviating to

10.0 nm and 12.4 nm within the measurement. The thickness of the upper ferromagnetic layer decreases from 32.9 nm to 3.4 nm over the series.

4.1.3. Spin Valve

In the case of a four layer system, the antiferromagnetic pinning layer is placed either on the bottom, when regarding the stack of an AF-F/S/F structure, or on top, in the case of an F/S/F-AF structure. In both cases the signal arising from cobalt in the cobalt oxide is close to that one of the nickel from the copper-nickel alloy layer. With *k*-factors of 0.762 for nickel and 0.763 for cobalt (taken from the inset in Fig. 4.1) and an incident helium particle energy of 3500 keV, the backscattered helium ions have an energy of 2667 keV and 2671 keV, which is too close together to resolve them in an RBS spectrum if both layers are adjacent. Because of this the thickness of the cobalt oxide layer has to be determined by a high resolution transmission electron microscopy image.

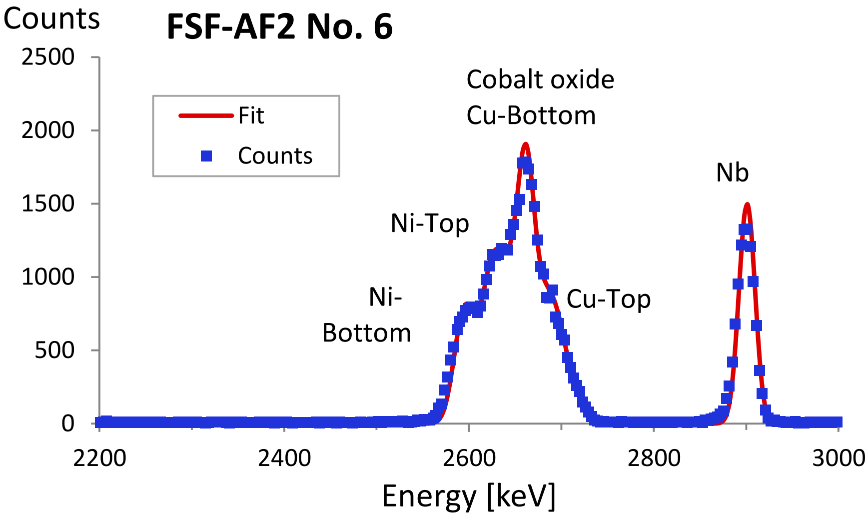

Fig. 4.8: RBS measurement of sample FSF-AF2 No. 6. In this kind of series the cobalt oxide layer is placed on top of the multilayer system.

In Fig. 4.8 an RBS measurement, *i.e.* a function of counts over energy is shown for sample No. 6 of series FSF-AF2. This kind of samples series are not protected by a silicon protection layer, because the outer most layer is a cobalt oxide layer, which is already oxidized. Before starting the simulation of the thicknesses of the individual layers, the thicknesses of the layers are determined by the evaluation of a HRTEM image, made from the sample FSF-AF2 No.5, which is the sample just next to the one shown Fig. 4.8. With this as a starting point the signal from the individual layers can be simulated. Because the measurement signal coming from the cobalt oxide layer and from copper in the bottom ferromagnetic layer overlap, at an energy of the backscattered He ions of 2660 keV, the height of this peak is given by the thickness of the lower copper-nickel layer and the thickness of the cobalt oxide layer

Furthermore, the height of this peak, *i.e.* the amount of counts measured by the detector, depends on the atomic concentration of cobalt in the cobalt oxide layer. During the deposition process either Co_3O_4 or CoO may have been formed. The cobalt oxide layer thickness has been determined by HRTEM images and the fitting of the layer is better done with an atomic concentration of cobalt of 43 at. % and oxygen of 57 at. % than with an equally weighted atomic concentration of 50 % for oxygen and cobalt. Since 43/57≈ ¾, the cobalt oxide in the sample is probably Co_3O_4. The thickness of the cobalt oxide layer can be cross checked by simulating the beginning of the RBS copper signal of the top alloy layer (see right lower side of the large peak in Fig. 4.8). The nickel concentration of this layer was assumed to be 59 at. %. If the cobalt oxide layer would have been assumed to be too large (small), the simulation would be shifted to the left (right) with respect to the measurement points in Fig. 4.8.

Next, the signal coming from the niobium layer is fitted by adjusting the niobium layer thickness and afterwards the thickness of the last layer is fitted, which is the copper-nickel layer at the bottom. The thickness is adjusted by the left side of the peak from the nickel in the bottom ferromagnetic layer. Also the Ni concentration of this alloy layer was assumed to be 59 at. %.

In Fig. 4.9 the RBS measurement of sample AF-FSF5a No. 2 is shown. The sample series consists of a cobalt oxide layer, which is placed on the Si buffer layer covering the Si substrate and above two ferromagnetic wedges which sandwich a superconducting layer. Finally there is a Si cap protecting the layers. In contrast to Fig. 4.8, the signal form the cobalt in the cobalt oxide layer in Fig. 4.9 is shifted to a lower energy and overlaps with the signal arising from nickel in the bottom ferromagnetic layer. The initial thickness of the cobalt oxide layer is again determined by a HRTEM image of the multilayer system.

The thickness of the top ferromagnetic layer can be controlled, during the fitting process, by shifting the peak, or better “shoulder”, labeled by Cu-Top in the figure until it fits the measurement. Furthermore, the onset of the niobium signal is governed by the layer above, *i.e.* by the silicon cap and the top ferromagnetic layer. Next, the niobium peak is simulated. The simulation of the thickness of the bottom ferromagnetic layer is done by observing the combined peak arising from the

Ni in the top layer and copper in the bottom layer. The cobalt oxide layer was again fitted with a value of 43 at. % of cobalt. The nickel content in the ferromagnetic alloy layers was again set constant at 59 at. %.

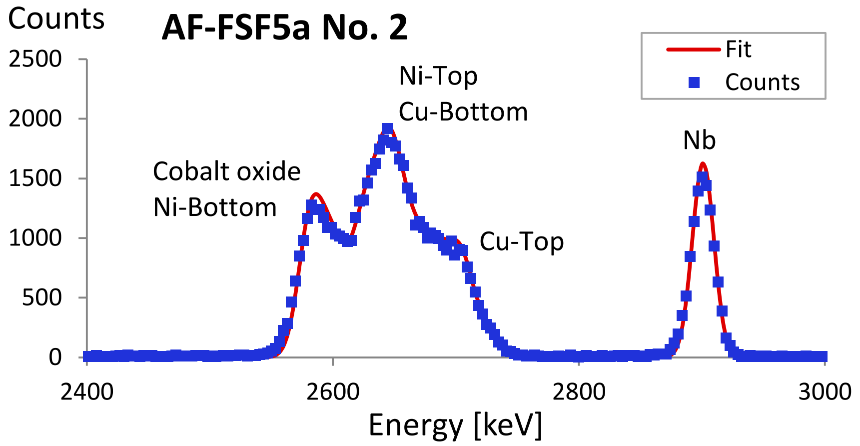

Fig. 4.9: RBS measurement of sample series AF-FSF5a No. 2. The cobalt oxide layer is placed on the substrate (covered by a Si buffer layer) on which the F/S/F structure and Si cap are deposited. The cobalt oxide and the two ferromagnetic layers give rise to one large peak.

In Fig. 4.10 the four layer system AF-F/S/F4 is shown. In this series a cobalt oxide layer is placed on the substrate (covered by a Si buffer layer), on which a ferromagnetic/superconducting/ferromagnetic layered structure is deposited. The system is protected from ambient conditions by a silicon cap.

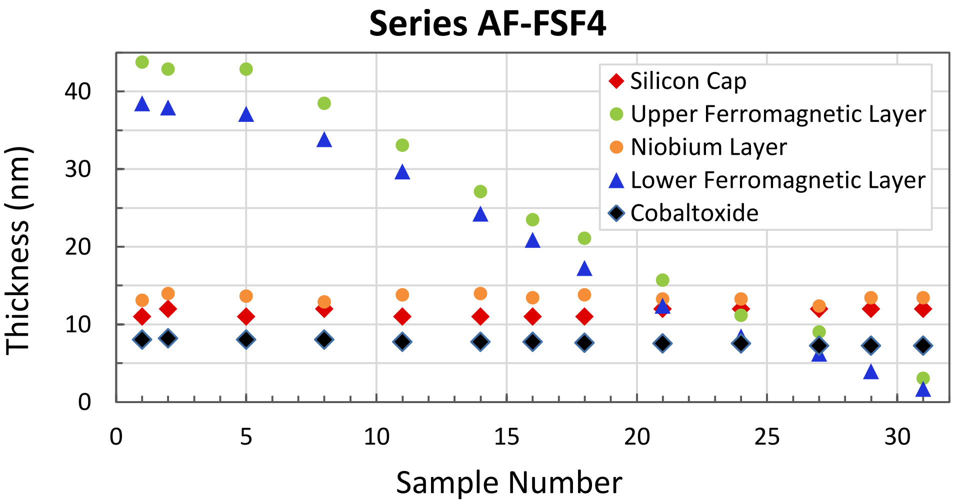

Fig. 4.10: Results of the RBS measurement of sample series AF-FSF4, which consists of two ferromagnetic wedges which enclose a superconducting niobium layer. A silicon cap prevents the layers from oxidization.

Similar to the double wedge three layer geometry, in the case of the four layer system both wedges decline continuously. For the bottom ferromagnetic layer the wedge begins from about 37 nm and ends at 1.7 nm, and for the top ferromagnetic layer the range is about 44 nm to 3 nm. The superconducting layer has an average thickness of 13.4 nm with a deviation of -0.3 nm to +0.6 nm and the silicon cap varies between 11 nm and 12 nm over the wedge. In the case of the cobalt oxide layer one observes a slight decrease of the layer, beginning with about 8 nm for sample No. 1 to 7.3 nm for sample No. 31. Again Co_3O_4 oxide is assumed to be present and the Ni content in the ferromagnetic alloy is set to 59 at. %. The thickness of the cobalt-oxide layer was determined by HRTEM to be 8.5 nm.

5. Transmission Electron Microscopy

To obtain information about the structure and quality of the prepared samples, Transmission Electron Microscopy (TEM) and High Resolution Transmission Electron Microscopy (HRTEM) has been performed, and Electron Diffraction Patterns of the samples have been analyzed. The microscope was a JEOL JEM 2100F, equipped with a GATAN imaging Filter and a CCD camera. The acceleration voltage was 200 kV.

The samples were prepared either in plane-view or in cross section. The preparation process for the cross section is schematically shown in Fig. 5.1.

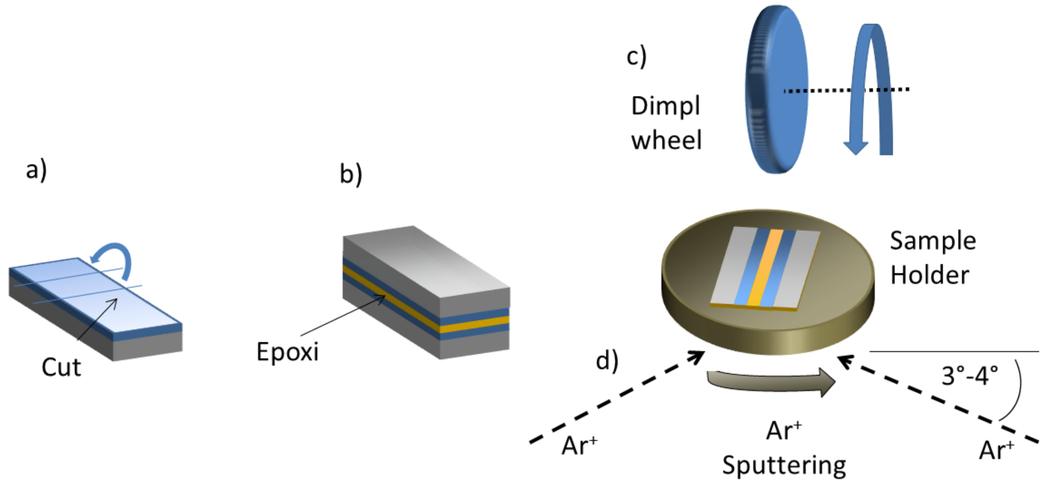

Fig. 5.1: Various steps in the preparation of a sample for cross sectional TEM analysis a) cutting b) gluing c) grinding and polishing d) Argon sputtering

In a first step, one sample of a sample series is cut perpendicular to its long side, i.e. parallel to the wedge, into stripes (see Fig. 5.1a). Next, two of these stripes are glued together with an epoxide resin, in a way, that the thin film layers face each other (indicated blue in Fig. 5.1b). Afterwards, this sample is glued into a sample holder, which has a diameter of about 3 mm, so that the layers are perpendicular to the flat side of the holder. Then the sample, as well as the sample holder, are grinded and polished until the system has a thickness of about 100 µm. The sample is then further prepared by using a “Gatan Dimple Grinder Model 656”, where a grinding wheel and a micrometer suspension do the thinning. Finally, the sample is ion etched with argon ions in a “Gatan Precision Ion Polishing System Model 691”, until a small hole in the middle of the sample is visible. The light microscope image of the hole is shown in Fig. 5.2. When the sample has passed the preparation optimally, one has four different places (shown with white arrows in the figure) where the sample thickness is a few tens of nanometers, which is needed for good high resolution TEM images.

For a plane view preparation the sample is cut again into stripes, but then directly glued into the sample holder. The further preparation is similar to that of a cross section, except that for this preparation the “back side” of the sample is thinned and argon sputtered until the hole appears.

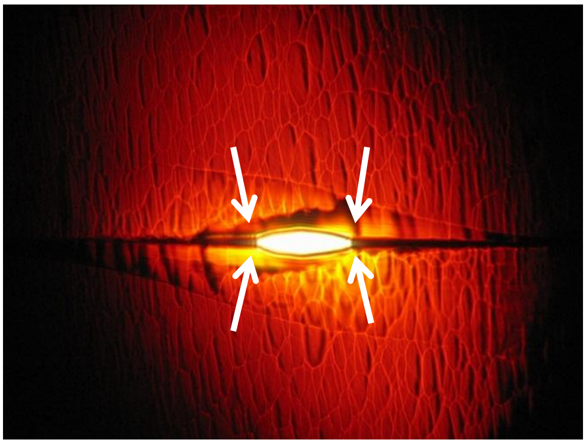

Fig. 5.2: Light Microscope image of the center hole after ion etching. The sample was WCN19 from a pure copper-nickel wedge series.

5.1. TEM and High Resolution TEM

In Fig. 5.3a) a cross sectional TEM analysis of sample FS2103 No. 1 is shown. In the top image the Si(substrate)/Si(buffer)/$Cu_{1-x}Ni_x$/Nb/Si(cap) structure of the bilayer can be clearly recognized. The image gives an overview over a large area of the sample of about 0.2 µm. The thickness of the niobium and copper nickel layer is 8.6 nm and 25.4 nm, respectively.

In the HRTEM images in Fig. 5.3b) the highly textured niobium and the copper nickel layer is shown. Fig. 5.3c) is the magnification of an area of Fig. 5.3b). The bright spots may represent the position of the niobium atoms, but in order to clarify this point a simulation of the image is needed. Depending on the value of the defocus the interference conditions change and the position of the atoms might be located at the position of the bright spots or in between.

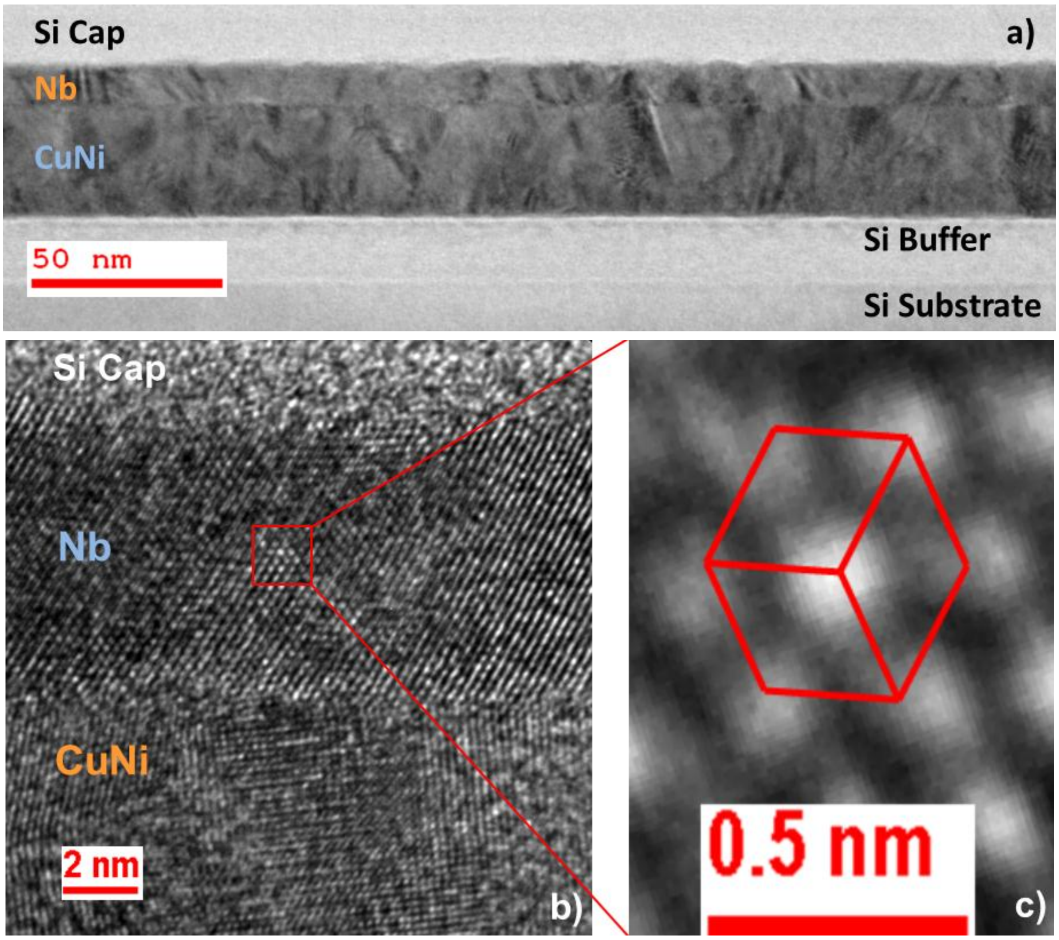

Fig. 5.3: a) Overview over the bilayer FS 2103 No. 1. The TEM image shows straight surfaces on a large lateral scale. b) High resolution image of the niobium and copper-nickel layer. c) Magnification at atomic resolution of the niobium layer. The red cube indicates the lattice orientation (according to [29]**).**

The ferromagnet/superconductor interface in Fig. 5.3b) shows that there has no interface layer been build. The interface roughness between the layers is on the atomic scale and shows no irregularities in the thickness, *i.e.* there is a sharp boundary. Furthermore, the interface between the niobium and the silicon cap and the copper-nickel alloy and the silicon buffer layer is quite linear.

The spacing between the niobium atomic layers in Fig. 5.3b) has been measured for several lattice planes and an average value of 2.36 Å was observed. This value is nearly equal to the 2.33 Å, which would be observed in the body centered cubic (bcc) niobium lattice for the separation of the {110} planes [**56**]. Considering this and the three fold symmetry in Fig. 5.3c), the viewing direction is the <111> direction. The growth of the niobium on the copper-nickel alloy occurs in the <110> direction, because one of the {110} planes of the bcc niobium is oriented parallel to the silicon substrate (see the horizontal rows in Fig. 5.3c). The red cube indicates the corresponding lattice structure in real space.

Measuring the separation of the lattice planes in the copper nickel layer gives distances of 2.07 Å and 1.85 Å, respectively. Considering, that the nickel and copper both crystallize in the fcc lattice with nearly the same lattice constants, Cu: 3.615 Å and Ni: 3.524 Å [**57**], these two values for the lattice spacings correspond to {111} and {200} planes in the copper-nickel alloy, respectively. However, from this high resolution TEM images it is not possible to uniquely identify the direction of growth of the ferromagnetic layer, because the respective lattice spacing depends on the area regarded.

In the case of F/S/F trilayers, samples from a single wedge and double wedge geometry series have been cross sectionally prepared.

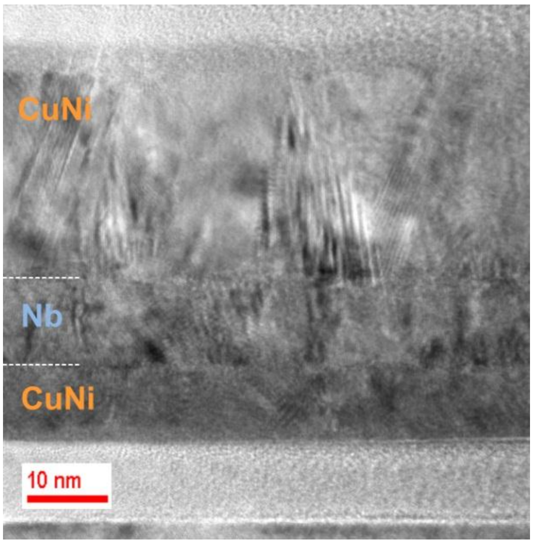

Fig. 5.4: Cross sectional TEM image of sample FSF1 No. 5, a single wedge geometry (according to [30]).

In Fig. 5.4 and Fig. 5.5 an overview TEM image of a sample from a single wedge and a double wedge sample series, FSF1 No. 5 and FSF5 No. 2, respectively, is given. For the single wedge sample the thickness of the top $Cu_{41}Ni_{59}$, the niobium layer and the bottom copper nickel layer is 31.2 nm, 10.6 nm and 8.6 nm, respectively. For the double wedge structure the thicknesses are 44.6 nm, 12.7 nm and 45.5 nm. The layer thicknesses, determined by TEM are in good agreement with those obtained by RBS, *i.e.* the deviations are within 10%. In Chap. 5.2 another image (Fig. 5.9a)) of sample FSF5 No2 is given. The interface of the niobium and one of the ferromagnetic layers is shown at high resolution. Again no intermediate layer has been formed and the roughness of the interface is of the order of 3 atomic layers or even less.

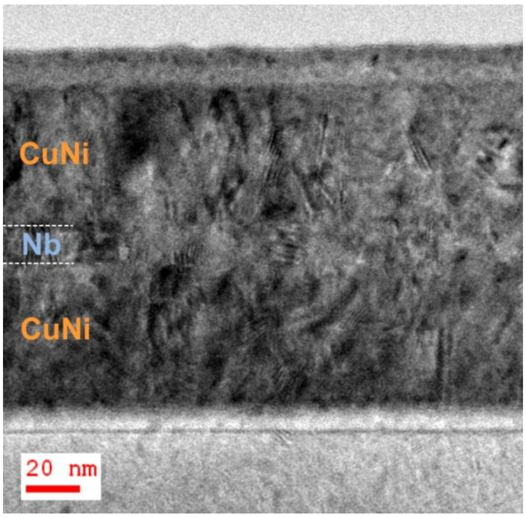

Fig. 5.5: Double wedge geometry specimen FSF5 No. 2 (according to [30]).

In the case of specimens with four layers, there are two different types of geometrical structures. In the first type the F/S/F spin valve core is deposited on top of the antiferromagnetic (AF) cobalt oxide layer, whereas in the second type the cobalt oxide layer is on top of it. Sample series AF-FSF5a belongs to the first type of geometry. Sample No. 13 of this series is shown in Fig. 5.6. The lateral extent of the image is about 500 nm. The individual layers are labeled in the image. For all layers, the thickness of the layer stays constant over the lateral extension of the image. The boundary between the individual layers is sharp and in this magnification shows no roughness even along on this wide lateral area.

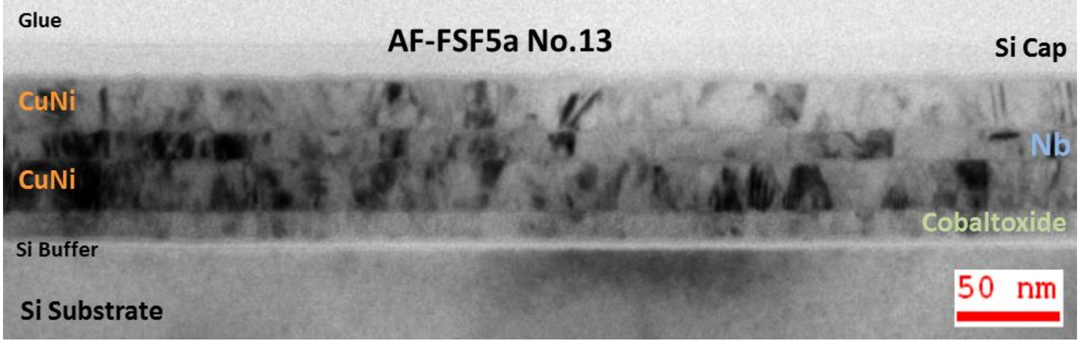

Fig. 5.6: Overview over the sample AF-FSF5a No. 13, which consists of a F/S/F spin valve core structure, which is deposited on top of a cobalt oxide layer. The image extends over a lateral size of about 500 nm.

In Fig. 5.7 the HRTEM image of sample FSF-AF2 No.5 is shown. The sample belongs to the second type of geometry. It consists of a spin valve core structure on which a layer of about 24 nm of cobalt oxide was deposited. The image, showing a section of the cobalt oxide region, was taken at a magnification of about 1.000.000 times. From the evaluation of the atomic concentration during fitting the RBS spectrum, as discussed in Chap. 4.1.3, one has a first indication that the cobalt oxide might be a Co_3O_4 and not CoO. A Co_2O_3 can be excluded from the consideration because it seems to be only stable under high oxygen partial pressures at low temperatures [**58**].

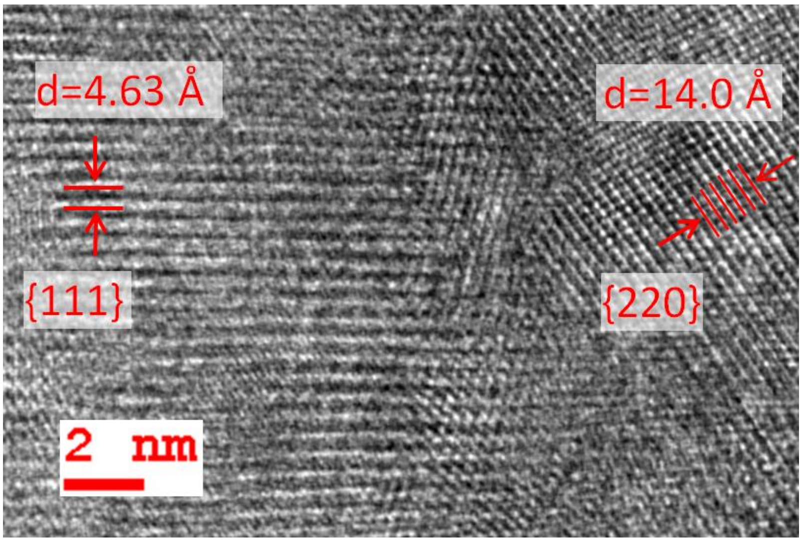

Fig. 5.7. HRTEM images of sample FSF-AF2 No. 5. The sample consists of a spin valve core structure with a Co_3O_4 layer on top. The image shows a section of the cobalt oxide. The indicated lattice planes belong to the {111} and {220} planes of Co_3O_4, respectively.

Cobalt monoxide has a rock salt, i.e. NaCl, structure, with a lattice constant of 4.260 Å [**59**] while Co_3O_4 has a spinel structure with a lattice constant of 8.084 Å [**60**]. With the value of the lattice constant, the spacings of the {111} and {220} lattice planes can be calculated. For CoO the values for these planes are, 2.46 Å and 1.51 Å, and for Co_3O_4, 4.665 Å and 2.85 Å, respectively. The HRTEM image in Fig. 5.7 shows various lattice planes of the cobalt oxide. The largest spacings give a value of about 4.63 Å, measured between two adjacent lattice planes, indicated on the left side of the figure. On the right side of the figure the distance over 5 lattices planes was measured to be 14.0 Å, which gives an average value of 2.80 Å. Thus, from the HRTEM image it can be concluded, that, at least at this particular place of the sample, Co_3O_4 has been crystallized. A statement about the lattice structure over a larger area of the sample has to be done by electron diffraction.

5.2. Electron Diffraction and Crystalline Orientation

The electron diffraction pattern of sample FSF5 No. 2, in Fig. 5.8, shows diffraction rings due to the poly-crystalline $Cu_{41}Ni_{59}$ alloy layers and the superconducting niobium layer and diffraction spots arising from the mono crystalline Si-substrate. The diffraction pattern has been obtained by using highly sensitive camera plates which have been scanned by an “Imaging Plate Scanner Micron” of Ditabis and converted to a Tagged Image File Format (TIFF).

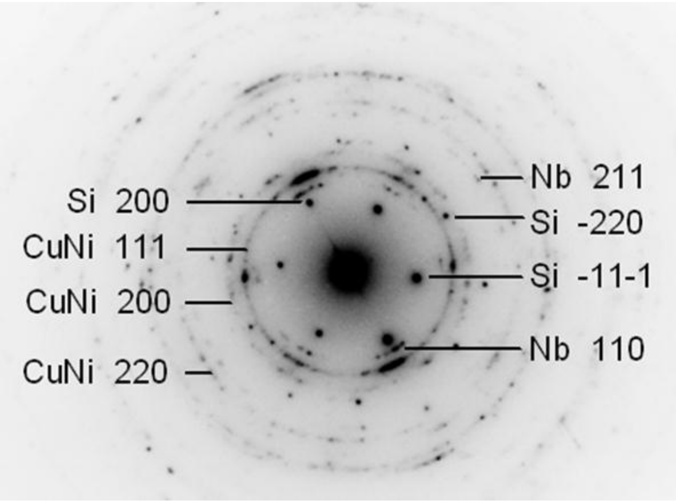

Fig. 5.8: Diffraction pattern of FSF5 No. 2 (according to [30]).

The silicon diffraction spots can be identified as belonging to the {111}, {200} and {220} planes of silicon giving a viewing direction into the <110> direction in the cross section [**61**,**62**,**63**,**64**,**65**]. From this result it is not possible to conclude definitely the perpendicular crystallographic direction. Potential candidates for low indexed directions are the <110>, <100> and <111> directions. Therefore, HRTEM investigations of the substrate region where made, yielding that the inter-planar spacing results in {100} planes parallel to the surface of the Si substrate of the FSF1 series.

Next, the amount of pixels from the central spot to the 111 spot of silicon is counted. Since the 111 spot corresponds to a spacing of 3.135 Å of the {111} planes in real space, the $\bar{1}1\bar{1}$ spots can be used as an internal standard, because the separation from the central spot is inverse proportional to the inter-planar spacings in real space. Furthermore, the silicon single crystal wafer can be used to check if any astigmatism is present in the image. In that case the silicon planes would have different deviations from the theoretical lattice parameters in different directions.

Using this internal standard, the diffraction rings arising from Nb and the $Cu_{41}Ni_{59}$ alloy can be indexed. Niobium gives rise to a 110 diffraction ring, which corresponds to a separation of the {110} lattice planes by 2.38 Å in real space. Compared to the bulk value this is an increase of the lattice parameter for these planes of 2.1 %.

Although this seems to be a large increase in the lattice parameter in a bulk material, it seems to be reasonable in thin film structures [**66**]. The presence of the 110 and the absence of the 200 diffraction ring shows, that one is looking into the <111> direction in the cross section [**61**,**62**,**30**]. This means, coonsidering only low indexed planes which have a dense package of atoms, that the bcc niobium film grows with {110} planes parallel to the silicon substrate. This conclusion is verfied by Fig. 5.9, in which {110} planes are visible for the niobium, identified by the inter-planar spacing. The distance is 2.38 Å, demonstrating (again and directly) the increase of the lattice parameters already concluded from the electron diffraction pattern above.

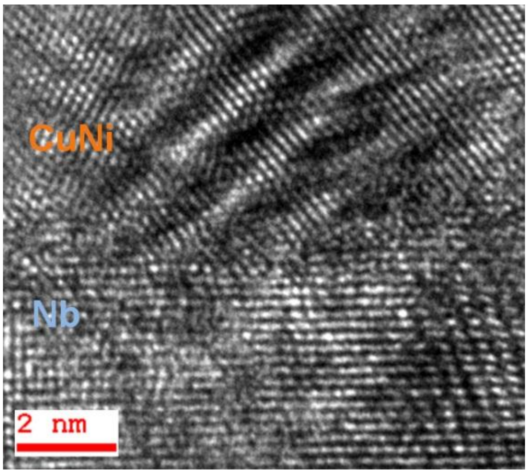

Fig. 5.9: High resolution transmission electron microscopy image of the niobium copper-nickel interface of the double wedge series sample FSF5 No. 2.

Following this kind of analysis, it can be furthermore concluded, that during the deposition process, the preferred growth of the ferromagnetic $Cu_{41}Ni_{59}$ layers is with {111} planes parallel to the silicon substrate. This conclusion comes from the presence of diffraction rings which correspond to {111}, {200} and {220} planes, yielding a viewing direction into the <110> direction in the cross section. This yields a <110>, <100>, or <111> direction (with planes with the same Miller indices perpendicular to the directions) in the plane view, if one again only considers low indexed, densely packed planes.

The final decision comes from Fig. 5.9, where the inter-planar spacing of the $Cu_{41}Ni_{59}$ lattice planes parallel to the Nb/$Cu_{41}Ni_{59}$ boundary give evidence for a preferred growth with {111} planes parallel to the Si substrate, as one may also conclude from the intensity distribution of the $Cu_{41}Ni_{59}$ diffraction ring in Fig. 5.8. The obtained results agree with the growth observed for Nb and $Cu_{41}Ni_{59}$ observed by X-ray diffraction for Nb/$Cu_{41}Ni_{59}$ bilayers and the orientation of Nb observed for a $Cu_{41}Ni_{59}$/Nb bilayer in Chap. 5.1 of the present work.

For the bottom ferromagnetic layer, there is no lattice mismatch between the amorphous silicon buffer layer and the copper nickel layer expected. However, the same does not hold for the top ferromagnetic layer, which has to grow on the niobium layer. The same counts for the niobium which is deposited on the polycrystalline bottom ferromagnetic layer. The growth of the niobium layer as well as the polycrystalline copper nickel layer has to occur in a way, which minimizes the interfacial energy between the layers.

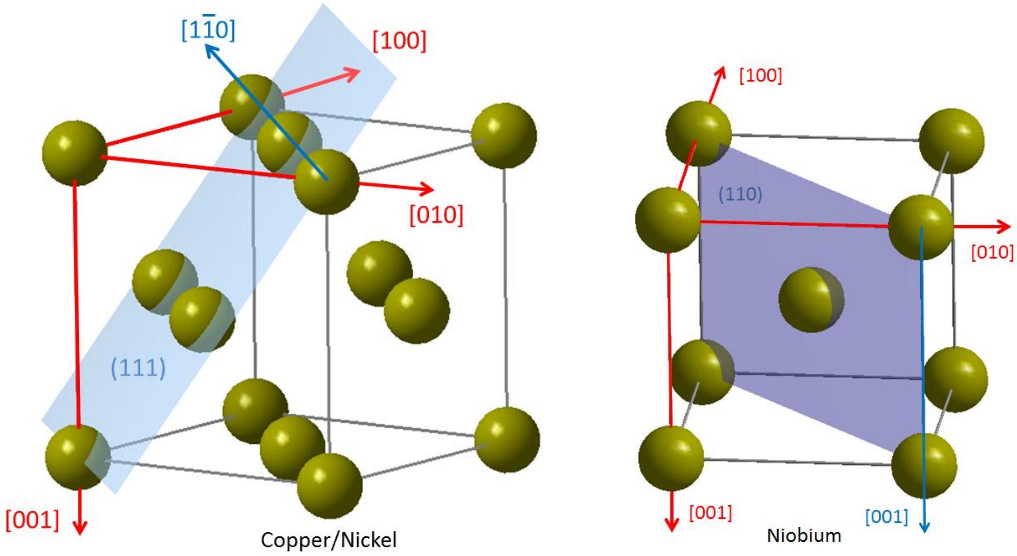

Fig. 5.10: Lattice structure of copper-nickel alloy and niobium. In the fcc copper-nickel alloy lattice the (111) plane is shaded, in the bcc niobium lattice the (110) plane. The Nishiyama-Wassermann orientation builds up an interface from a $(111)_{fcc}$ plane with a $(110)_{bcc}$ plane. The relative orientation thereby is the $[1\bar{1}0]_{fcc}$ direction parallel to the $[001]_{bcc}$ direction. The directions and planes indicated relate to a right-handed coordinate system in the upper left atom of the elementary cells.

In the case of a fcc(111)/bcc(110) interface there are several possibilities for the relative orientation of the (111) plane with respect to the (110) plane [**67**,**68**,**69**,**70**]. Assuming a rigid sphere model and a simple sinusoidal interaction potential it can be shown that there are three different configurations which minimize the interface energy. This first one is the Nishiyama-Wassermann [**67**,**68**,**69**,**70**] orientation in which the $[1\bar{1}0]_{fcc}$, or $[0\bar{1}1]_{fcc}$ see [**62**], direction is parallel to the $[001]_{bcc}$ direction, see also Fig. 5.10. The second one is the Kurdjumov-Sachs [**67**,**68**,**69**,**70**] relationship with $[1\bar{1}0]_{fcc}$ parallel to $[1\bar{1}1]_{bcc}$ and a R30° orientation relationship [**65**,**69**] with $[2\overline{11}]_{fcc}$ parallel to $[001]_{bcc}$. In which configuration the layer will crystallize depends on d_{bcc}/d_{fcc}, that means the ratio of the atomic diameters of the bcc and fcc lattice [**67**].

Considering a rigid sphere model of the atomic arrangement, the distance between the atoms in any direction is equal to the nearest neighbor distance. For the bcc lattice it results from the <111> direction, yielding $(\sqrt{3}/2)a_{bcc}$, where a_{bcc} is the lattice constant of the bcc, in our case niobium, lattice, *i.e.* 3.303 Å. For the fcc lattice the <110> direction gives the nearest neighbor distance, resulting in $(\sqrt{2}/2)\,a_{fcc}$, where a_{fcc},= 3.539 Å for $Cu_{41}Ni_{59}$. Thus, $a_{bcc}/a_{fcc}=0.93$, so that for the ratio $d_{bcc}/d_{fcc} = (\sqrt{6}/2)\,a_{bcc}/a_{fcc}$ a value of 1.14 is obtained, for which (see Fig. 6 of Ref. [**67**]) the Nishiyama-Wassermann relationship shows a minimum in the interfacial energy. Thus, this orientation is expected for our $Cu_{41}Ni_{59}$/Nb interfaces (Tab. I of Ref. [**68**]).

Considering the symmetry of the S/F and F/S boundaries in the F/S/F trilayers the interfacial energy minimization should be the same and so, the crystalline growth in both F-layers. Since the ferromagnetic layers are expected to grow in the same orientation, the transparency [**22**] is expected to be similar for both boundaries. However, in detail the crystal growth is influenced by much more parameters, like the deposition temperature, which may differ during the deposition process because, *e.g.*, the heat conductivity of niobium and the $Cu_{41}Ni_{59}$ alloy is not the same. This may cause differences in the boundaries in detail, yielding transparencies which are not identical.

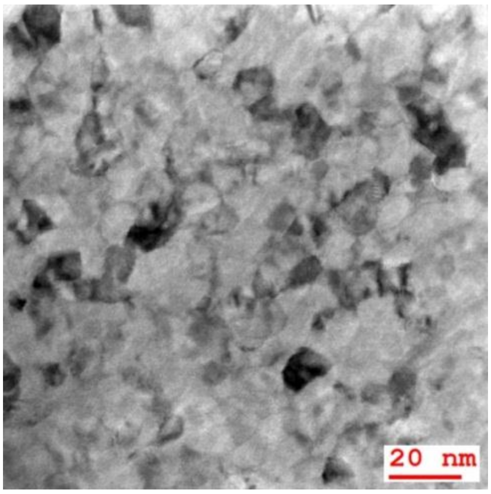

Fig. 5.11: Plane View Image of sample FSF3 No. 29

So far, the orientation of the grains in the polycristalline layers was discussed. In the following TEM investiagations are presented to get an impression of the size of these grains.

In Fig. 5.11 a plane view image of sample No.29 of the trilayer series FSF3 is shown. Although the image has been taken at a very thin area of the sample, prepared for the plane view TEM investigations, not only grains from the bottom copper-nickel alloy layer, but also grains from the niobium layer and the top copper-nickel alloy layer may be present in the image. It seems that all grains have a size which is in the order of 10 nm, when viewed from top onto the layers.

In Fig. 5.12 a cross sectional view of the trilayer sample FSF1 No.5 is shown. The image was taken using an annular dark field detector in the scanning transmission electron microscopy mode (STEM).

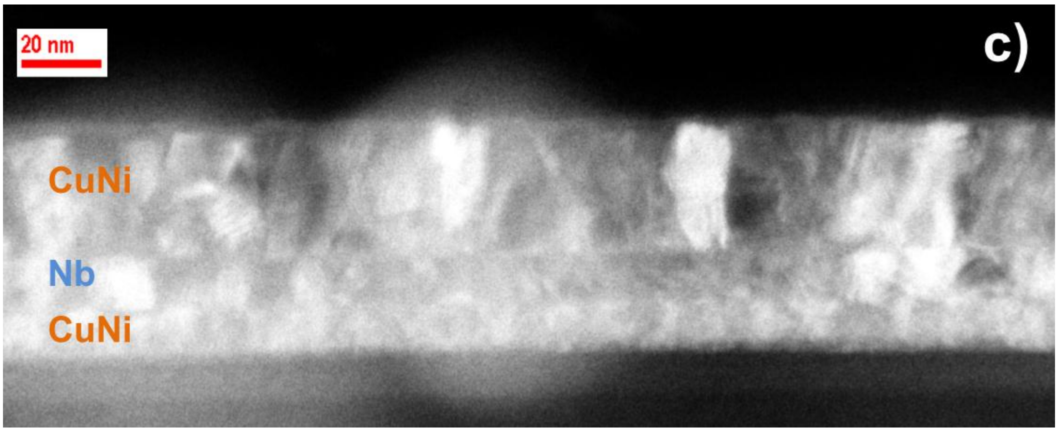

Fig. 5.12: Cross sectional dark field TEM image of the trilayer sample FSF1 No5 (after [30]).

Again, different grains could be resolved, this time in a side view. It seems that the grain size in the direction perpendicular to the layers is equal to the thickness of the respective layer. This means that the thickness of the grains in the bottom $Cu_{41}Ni_{59}$ layer and in the Nb layer is of the order of 10 nm, while the grains in the top layer extend over the layer thickness of about 30 nm, i.e. the grain size is limited by the the thickness of the respective metal layer.

To get information about the lattice structure of the cobalt-oxide layer over an extended lateral scale, a cross sectional electron diffraction pattern of sample AFW1 No. 2 has been made. The sample series solely consists of a cobalt oxide wedge on top of the silicon substrate. For this analysis a sample from a single layer cobalt oxide series was taken, because the scattering intensity of cobalt oxide is small compared with that one of copper-nickel and niobium. Furthermore, the diffraction rings of cobalt oxide, either in the oxidization state II or III, may overlap with the diffraction rings arising from the copper-nickel layer. To determine the diffraction spots, as well as the diffraction rings in Fig. 5.13, first the silicon spots have to be identified to arise from {111} and {200} planes and used as internal standards, as described above. The most striking diffraction ring has *d*-spacing. *i.e.* a distance from the central spot, which corresponds to lattice planes with a distance of 2.44 Å in real space, which could be attributed to the {111} planes of CoO, with a lattice separation of 2.46 Å, or to {311} planes of Co_3O_4 which have a spacing of 2.44 Å.

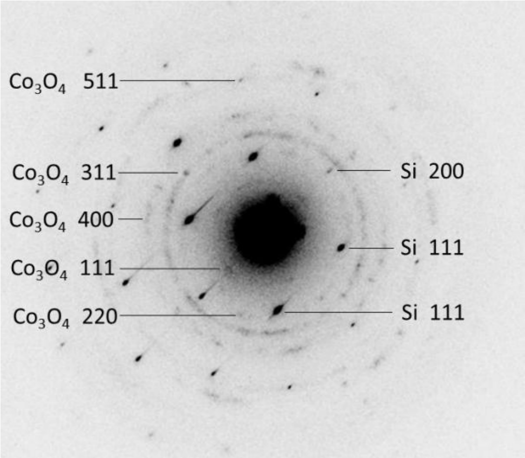

Fig. 5.13: Electron diffraction pattern of the cross sectionally prepared sample AFW1 No. 2. It consists solely of a cobalt oxide layer on top of the substrate.

The next prominent diffraction ring corresponds to lattice planes, which are separated by 2.03 Å in real space. Polycrystalline cobalt monoxide would show a diffraction ring arising from {200} planes with d-spacings of 2.13 Å, while from Co_3O_4 it would originate from {400} planes with a separation of 2.03 Å. Further evidence for the presence of Co_3O_4 is given by the two faint diffraction rings, arising from the {111} planes with lattice separations of 4.66 Å and {220} planes with a lattice spacing of 2.856 Å in real space.

6. Magnetic Measurements

The itinerant electron model can be used to describe ferromagnetism of the transition metals Fe, Co and Ni. In this group two bands overlap [**71**]. There is the 4s band of electrons of high mobility with a shape similar to the band of free electrons and the 3d band, where the electrons are attached more tightly to the atoms. This model offers an explanation why nickel is a ferromagnet and copper, with only one atomic number more, is not. In the case of copper, the electron configuration for a free copper atom is $4s^1 3d^{10}$, *i.e.*, the 3d band is completely filled, whereas the 4s band is half filled. The electron configuration of atomic nickel is $4s^2 3d^8$ which means that the s band is fully occupied and the 3d band partially.

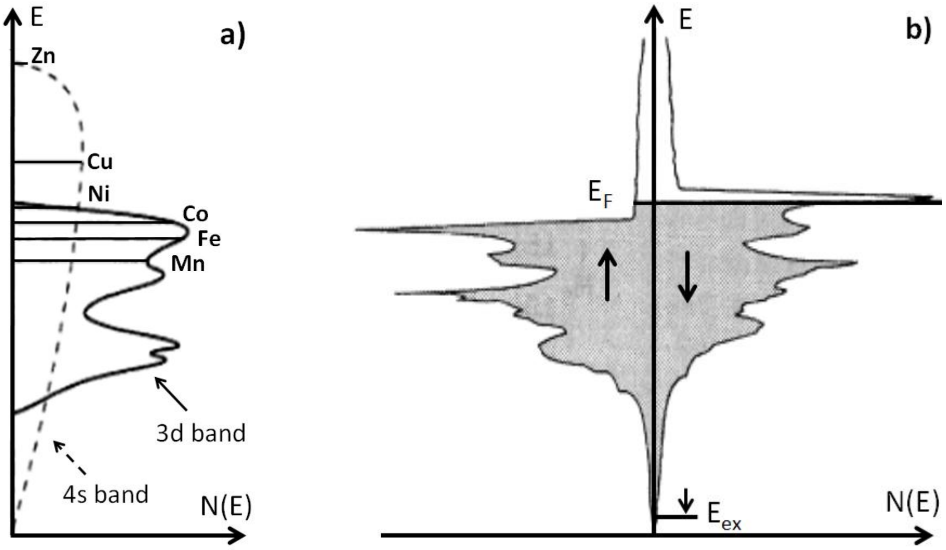

Fig. 6.1: a) Density of states for some of the transition metals. The structure of the 3d and 4s band is assumed to be the same for all materials (after [72**]) the horizontal lines mark the Fermi energies for the respective metals b) Density of states for nickel below the Curie temperature. Due to the exchange energy the spin up and down bands are split (after Ref. [**73**]).**

In a solid the electrons tend to form bands and hybridize, so that it is not possible to attribute the atoms to individual bands. In Fig. 6.1a) the density of states for various elements of the iron group is given. It is assumed that the shape of the 4s and 3d band, respectively, does not change for increasing atomic number. The density of states of the 4s band in this figure is overdrawn. The 3d atoms are rather tightly attached to the atoms, whereas the 4s electrons are rather free and enter the conduction band. Nickel has 10 outer electrons from which statistically 9.46 are in the 3d band and 0.54 electrons in the 4s band. In contrast to copper, which has its 3d band completely filled and one 4s electron in the conduction band [**72**].Since both spin sub bands are equally filled the total net magnetization of the 3d-band is zero.

Fig. 6.1b) gives the density of states below the Curie temperature. There is a split of the spin up and down bands due to the exchange interaction [**73**]. For nickel, five electrons of the 3d band will lower their energies by aligning the spin parallel to the exchange field while 4.46 electrons will align the spin antiparallel, leaving on average 0.54 spin uncompensated electrons in the 3d band. These electrons give rise to a magnetic moment of $0.54\mu_B$ per atom at T=0K. Therefore, the saturation magnetization is $M_s=0.54N\ \mu_B$, where N is the number of Ni atoms in the sample [**41**]. However, experimentally a value of $M_s=0.60N\ \mu_B$ can be observed. The additional magnetic moment arises from an orbital contribution to the magnetic moment [**74**].

When an alloy between copper and nickel is formed, ferromagnetism vanishes when the atomic concentration of copper is increased, since the copper 4s electrons first occupy the places in the nickel 3d band. When the copper concentration reaches about 60 atomic per cent, all 0.54 holes in the 3d band of nickel are filled up and the alloy is no longer ferromagnetic.

6.1. Analysis of the Curie Temperature and Saturation Magnetization

The content of this chapter has been already published in Ref. [**28**]. In order to analyze the magnetic properties of the samples, they were measured with a Quantum Design MPMS-5 superconducting quantum interference device (SQUID) magnetometer. The SQUID magnetometer measures the magnetic moment, m [emu] of the sample. From the magnetic moment, the magnetization M [emu/mol] is calculated by $M = m[\text{emu}]/[(V_{\text{film}}/V_{\text{mol,CuNi}})\text{mol}]$, where V_{film} is the volume of the $Cu_{41}Ni_{59}$ film, and $V_{\text{mol,CuNi}} = 6.8\ \text{cm}^3$ is the volume of 1 mol of an $Cu_{41}Ni_{59}$ alloy.

In Fig. 6.2, the magnetization is shown as a function of the temperature. During the measurement an external field of 1000 Oe was applied parallel to the thin film samples, i.e. perpendicular to the gradient of the $Cu_{41}Ni_{59}$ wedge, from which the sample series was cut. The samples have the thicknesses 48 nm, 21 nm and 8 nm, *i.e.* they were taken from the thick, middle and thin end of the wedge, respectively. The cgs unit Oe can be converted to SI units by using 1 Oe = $(10^3/4\pi)$(A/m) = 79.58 A/m [**75**]. The conversion from emu to mol will be discussed below.

Samples #21 (blue triangles) and #1 (red squares) were measured during cooling down, while #12 (green circles), cooled down in a field of 1000 Oe, was measured, during warming up. Since the external applied magnetic field during the measurement is equal to the value for which all branches of the hysteresis curve (see Fig. 6.4) meet, it is not essential in which, however, field the sample actually was cooled down before the measurement.

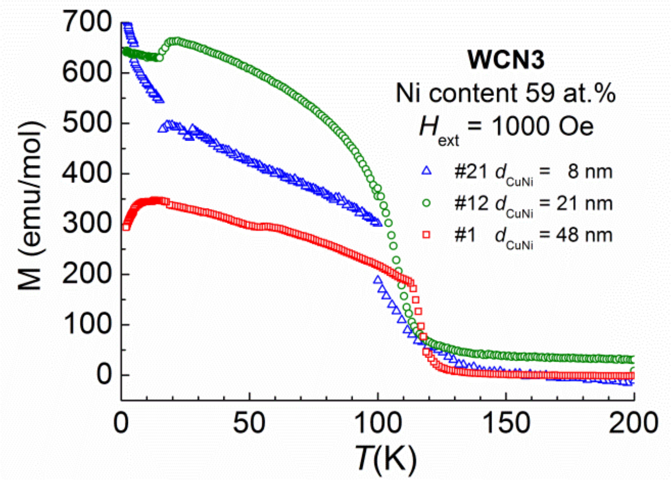

Fig. 6.2: Temperature dependence of the magnetization of $Cu_{41}Ni_{59}$ thin films measured in an external applied field of 1000 Oe [28].

For a bulk specimen of copper nickel alloy, with a nickel content of 59 at. %, the Curie temperature, i.*e.* the onset of ferromagnetic ordering, is T_C = 180 K [**74**]. For thin films, the ferromagnetic transition temperature is somewhat lower [**76**]. The three samples have similar Curie temperatures. The onset of the ferromagnetic ordering is at, T_C = 100 K, 110 K and 118 K, for samples No.21 (d_{CuNi} = 8 nm), No.12 (d_{CuNi} = 21 nm) and No.1 (d_{CuNi} = 48 nm), respectively, which means that the Curie temperature increases slightly for increasing film thickness. The measured T_C values are in agreement with the thickness dependence for $Cu_{40}Ni_{60}$/Cu thin film multilayers with a 10 nm thick Cu interlayer [**76**]. This documents the high homogeneity of the magnetic properties of the material over the sample series. In Fig. 6.2 the signal, above the Curie temperature, arising from the diamagnetic silicon substrate as well as from a possible ferromagnetic background, was set to zero.

In Fig. 6.3 and Fig. 6.4 the hysteresis curve for sample WCN2 No. 12 is shown. The measurement has been made at a temperature of 2 K and the external field was applied parallel to the film plane, as described above. The signal of the curve is a superposition of two contributions, one arising from the diamagnetic Si-substrate with a negative slope and the other from the ferromagnetic alloy. The magnetic moment $m(H)$ is given as measured by the magnetometer.

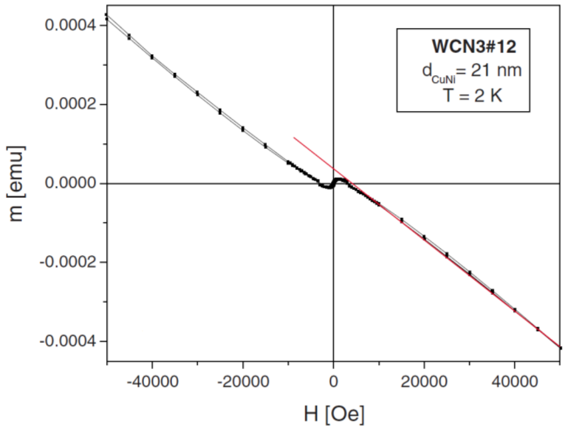

Fig. 6.3: Hysteresis measurement of sample WCN3 No. 12 at a temperature of 2 K. The figure shows a small ferromagnetic signal for low fields and a strong diamagnetic signal from the substrate for high fields. The saturation magnetization is extrapolated as indicated by the red straight line (from Ref. [28]).

For high applied magnetic fields the diamagnetic contribution, with a constant negative slope dominates, as shown in Fig. 6.3. For small magnetic fields, *i.e.* below 1000 Oe, the ferromagnetic part becomes visible (see Fig. 6.3 and, in higher magnification, in Fig. 6.4). In the case of high fields, *i.e.* above the saturation magnetization of the ferromagnetic film, the combined signal, arising from the Si and $Cu_{41}Ni_{59}$ alloy, can be written as, $m=\chi_{Si}[(V_{Si}/V_{mol,Si})mol]H+[(V_{film}/V_{mol,CuNi})mol]M_s$. Here, χ_{Si} is the magnetic susceptibility of the silicon with the units [emu/(mol×Oe)], V_{Si} and $V_{mol,Si}$ are the volume of the Si substrate and the volume of 1 mol Si, respectively, and M_S is the saturation magnetization of the ferromagnetic film, with units [emu/mol]. The saturation magnetization is obtained for H=0 in the above formula, yielding $m_S/[(V_{film}/V_{mol,CuNi})mol]=M_S$. It is determined from the experiment by a back extrapolation of the straight red line in Fig. 6.3 from high fields to zero field. The saturation magnetic moment, m_s, of sample WCN3 No. 12, thus obtained for the magnetic alloy, is $m_S = 3.7\times10^{-5}$ emu, which corresponds to a saturation magnetization of $M_S = 790$ emu/mol. For the thickest sample, WCN3 No. 1, the saturation magnetization, evaluated in this way from a similar hysteresis curve, is $m_S = 1.1\times10^{-4}$ emu, yielding $M_S = 900$ emu/mol. For the thinnest sample of the series, WCN3 No. 21, high field hysteresis measurements are not available. The error in our determination of the saturation magnetization is at least about 10%, due to the back extrapolation of the magnetic moment to H=0.

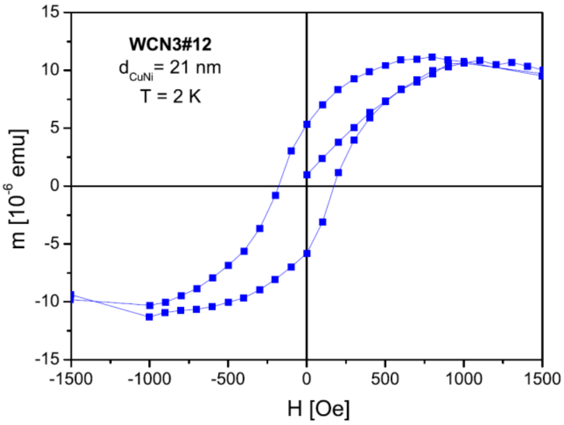

Fig. 6.4: Measurement of the hysteresis curve at a temperature of 2K [28].

These values are comparable to those obtained in Ref. [**76**] for $Cu_{40}Ni_{60}$/Cu thin film multilayer samples with a thickness of the $Cu_{40}Ni_{60}$ layer ranging from 4.2 nm to 34 nm. The saturation magnetization had values M_S=72-112 emu/cm^3. In order to compare the obtained saturation magnetizations with the results of the present work, emu/cm^3 has to be converted to emu/mol. Since, 1 emu/mol = 1 (emu/cm^3)(cm^3/mol) with 1 emu/cm^3=10^3 A/m in SI units, that means 1 emu = 10^{-3} Am^2, one gets 1 emu/mol = 10^{-3} (A/m) (m^3/mol). For a $Cu_{41}Ni_{59}$ as well as for a $Cu_{40}Ni_{60}$ alloy, 1 mol has a volume of $V_{\mathrm{mol,CuNi}}$ = 6.8×10^{-6}m^3, yielding 1 emu/mol = 0.147×10^3 A/m. Thus, M_S=72-112 emu/cm^3 gives (72-112)×10^3 A/m = [(72-112)×10^3 / (0.147×10^3)] emu/mol = (490-762) emu/mol. The value of 762 emu/mol for 34 nm can be compared with the sample WCN3 No. 1 of thickness 48 nm, with M_S = 900 emu/mol. Sample WCN3 No. 12 has a saturation magnetization of M_S = 790 emu/mol and a thickness of 21 nm and can be compared with a 17 nm sample of Ref. [**76**] which has a saturation magnetization of M_S=100 emu/cm^3, *i.e.* 680 emu/mol. Both samples are in reasonable agreement with the ones obtained in Ref. [**76**]. In both cases the saturation magnetization of our samples is a factor of 1.2 larger.

The saturation magnetization of 790 emu/mol and 900 emu/mol obtained by the hysteresis measurements at 2 K for sample WCN3 No. 12 and WCN3 No. 1, respectively, should be the same as the magnetization values obtained in Fig. 6.2 at the same temperature. The thinnest sample, No. 21, shows a result which is close to these values. For sample No. 12, with the medium thickness, the saturation magnetization obtained from the hysteresis curve is somewhat larger. The deviation is significantly larger for sample No. 1. The reason is not clear. An evaluation of the magnetic moment of samples WCN No. 12 and WCN No. 1 at H=1000 Oe from the measured hysteresis curves, considering the diamagnetic moment of the Si substrate, yields values for the magnetization, which also not agree with those of Fig. 6.2 at 2 K for these samples (for details see [**28**]).

Finally, one can calculate the magnetic moment per atom of the alloy, m_{at}, from the saturation magnetization obtained for our samples. To get m_{at} in the presence of 1emu/mol $=0.147\times10^{3}$A/m (see above) one has to multiply this result for the magnetization, i.e. the magnetic moment per volume in SI units, by $V_{mol,CuNi}=6.8\times10^{-6}\text{m}^3$ divided by Avogadro's constant, that means by the volume per atom. Thus, one gets m_{at}(1emu/mol)$=0.166\times10^{-26}\text{A/m}^2=0.179\times10^{-3}\mu_B$. Here, $\mu_B=e\hbar/2m_e=0.9274\times10^{-23}\text{A/m}^2$ is the Bohr magnetron, where e, $\hbar=h/2\pi$ and m_e are the elementary charge, Planck's constant h divided by 2π, and the electron mass, respectively. For M_S of samples WCN3 No. 12 and WCN3 No. 1 of 790 emu/mol and 900 emu/mol, respectively, one gets $m_{at}=0.14\mu_B$ and $0.16\mu_B$. The results are equal to or close to the bulk material value for a $Cu_{41}Ni_{59}$ alloy of $0.14\mu_B$ [**74**].

6.2. Determination of the Easy and Hard Axis

For magnetic anisotropic materials, the direction of spontaneous magnetization, in the absence of any external magnetic field, is given by its easy axis (of magnetization). The source of this uniaxial direction of magnetization can be, e.g. the magneto crystalline anisotropy, which means that the lattice structure introduces favorable directions of magnetization.

In the framework of the Stoner-Wohlfarth model [**77**] the energy density of a particle, with an uniaxial direction of magnetization, in an external magnetic field, H, can be written as

$$E_{tot}=K_u\sin^2\theta-\mu_0 MH\cos(\alpha-\theta) \tag{6.1}$$

Here, the first term represents the uniaxial anisotropy with, K_u, being the uniaxial anisotropy constant, arising from, *e.g.* the shape and/or magneto crystalline anisotropy. The second term describes the interaction of the magnetized particle with the applied field, with *M*, the magnetization of the particle, *H* the applied field. The angles α and θ are the directions of the external field and the direction of the magnetization, shown in Fig. 6.5, respectively.

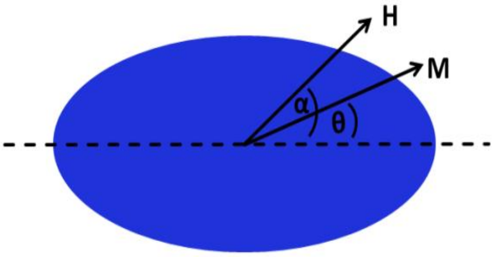

Fig. 6.5: Stoner particle (fixed in space) with a magnetization *M* and an external field *H*. Here, α and θ give the angles of the external field and the magnetization to the anisotropy axis, respectively (according to [78]).

Minimizing the total energy with respect to θ, gives two conditions, $\frac{dE_{tot}}{d\theta} = 0$ and $\frac{d^2E_{tot}}{d\theta^2} > 0$. For α=0°, *i.e.* the external applied field is parallel to the easy axis of magnetization, i.e. along the dashed line in Fig. 6.5, the first derivative becomes $\left.\frac{dE_{tot}}{d\theta}\right|_{\alpha=0} = 2K_u \sin\theta\cos\theta - MH\sin\theta = 0$ giving [**77**,**78**],

$$H = H_C = \frac{2K_u}{\mu_0 M_S} \tag{6.2}$$

which can be interpreted as the maximum anisotropy field. For α=0°, and thus θ=0°, there are only two possible configurations of the magnetization, either parallel or antiparallel to the external field, and the transition between both is abruptly happening at the maximum coercive field, H_C.

Fig. 6.6 visualizes the change of the hysteresis curve for various angles between the easy axis and the external applied field. For increasing angles the coercive field decreases. If the angle is parallel to the hard direction (*i.e.* perpendicular to the easy direction), the coercive field vanishes, because the magnetization of the particle continuously increases or decreases with an increasing or decreasing magnetic field [**78**].

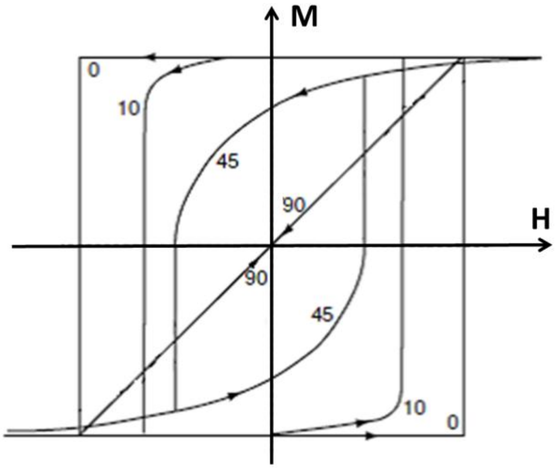

Fig. 6.6: The figure shows how the hysteresis curve changes when the externally applied field has a certain angle with the anisotropy axis of a particle. For a field applied parallel to the anisotropy axis, the hysteresis loop is a perfect square, while the *M*(*H*) behavior is proportional if the external magnetic field is applied parallel to the hard axis (according to [78]).

To determine the easy and hard axis, the samples were cut into a square and measured in three different directions, which are shown in Fig. 6.7. The orientations are (from left to right), the magnetic field perpendicular to the film plane, the magnetic field parallel to the film plane and parallel to the direction of an increasing/decreasing wedge (from which the sample series was cut) and parallel to the thin film surface but perpendicular to the direction, i.e. thickness gradient, of the wedge.

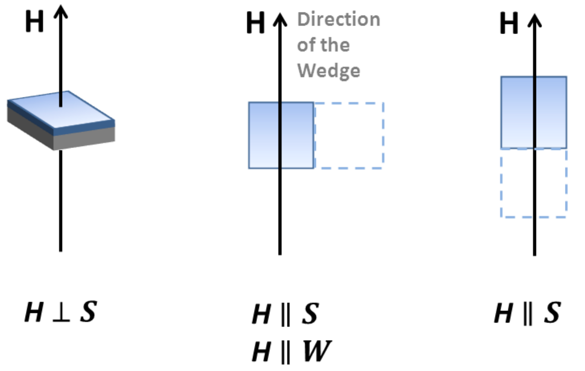

Fig. 6.7: Sample orientation with respect to the external field. From left to the right, the field is perpendicular to the surface of the sample, parallel to the surface and to the gradient of the wedge of which the sample series was cut and parallel to the sample surface and perpendicular to the gradient of the wedge. The dotted line indicates the original sample size of the series.

The measured sample No. 9 is from the $Cu_{41}Ni_{59}$ sample series WCN21. To increase the measurement signal, four ferromagnetic wedges were deposited, which were separated by a silicon layer. The sample geometry has been sketched in Fig. 3.8 of Chap. 3.4. Sample WCN21 No. 9 has a thickness 42.5 nm for each of the ferromagnetic layers, according to RBS measurements, and had a size of 2.5 mm times 2.8 mm. The measurements of the hysteresis curves are given in Fig. 6.8. From the data of the magnetic moment of the sample, obtained by the SQUID magnetometer, the diamagnetic background of the Si substrate has been subtracted. The orientation of the magnetic field is given in the legend and is labeled according to the description in Fig. 6.7. The inset in the figure shows a TEM image of sample WCN21 No. 19. The $Cu_{41}Ni_{59}$ alloy layers are separated by silicon layers.

Comparing Fig. 6.8 with Fig. 6.6 shows that the direction of the easy axis is perpendicular to the plane of the film, which means that the present $Cu_{41}Ni_{59}$ alloy has a perpendicular magnetic anisotropy (PMA). This is in agreement with the result of another group which investigated a $Ni_{60}Cu_{40}$ alloy and could extrapolate a PMA up to a ferromagnetic layer thickness of 55 nm [**76**], as discussed below.

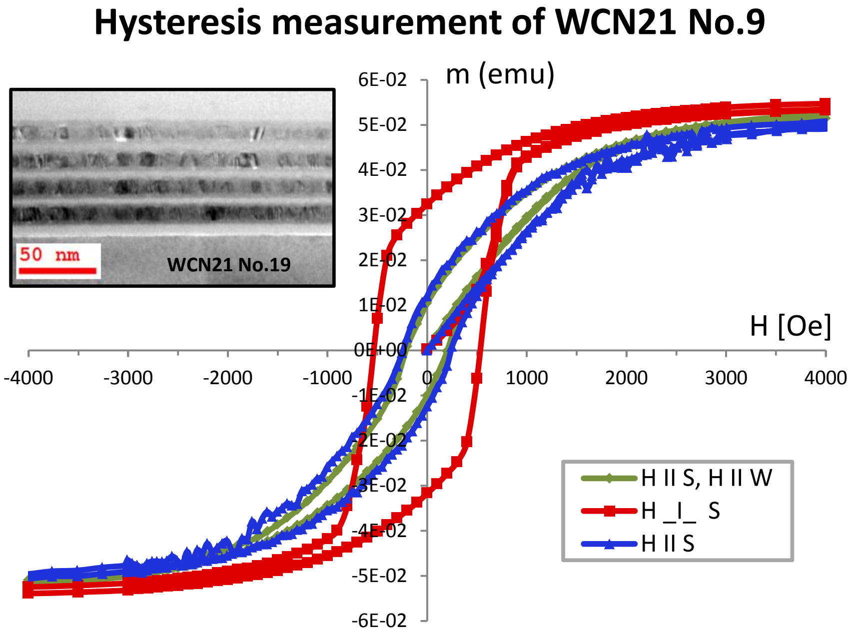

Fig. 6.8: Hysteresis curves of sample WCN21 No. 9. The sample series was cut from four ferromagnetic $Cu_{41}Ni_{59}$ wedges, separated by a silicon layer. The orientation of the sample with respect of the magnetic field was explained in Fig. 6.7. The direction of the easy axis is perpendicular to the thin film. The inset shows a TEM image of sample WCN21 No. 19. The four copper-nickel alloy layers are separated by silicon buffer layers. The measurement was made a temperature of 2 K.

6.3. Exchange Bias

In 1956 Meiklejohn and Bean published that “A New Magnetic Anisotropy has been discovered, which is best described as exchange anisotropy. This anisotropy is the result of an interaction between an antiferromagnetic material and a ferromagnetic material” [**79**]. The phenomenon is characterized by a shift of the center of the magnetic hysteresis loop from H=0 to H≠0 as sketched in Fig. 6.9. The dashed line gives the hysteresis curve of Co/CoO nanoparticles after cooling to 77 K without an externally applied magnetic field. The solid line is the result of a measurement with an externally applied magnetic field of 1 Tesla, when cooling down to the temperature of LN_2, i.e. 77 K.

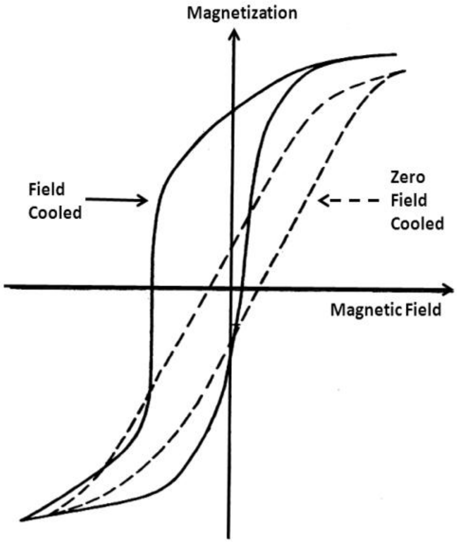

Fig. 6.9: Shift of the hysteresis loop of a ferromagnet due to the presence of an antiferromagnet, where the dashed line is a measurement after cooling down the sample in zero field and the solid line is the measurement after cooled in a field, according to [80**].**

The shift of the hysteresis curve can be understood when considering the spin configuration of a ferromagnetic-antiferromagnetic boundary, shown in Fig. 6.10. In a first step the sample is cooled to a temperature below the Curie temperature, T_C, of the ferromagnet, but still above the Néel temperature, T_N, of the antiferromagnet. The spins of the ferromagnet align with the external field, while those of the antiferromagnet stay at a random orientation (Fig. 6.10a). Below the Néel temperature the antiferromagnet orders the first spin row parallel to the ferromagnet, while the subsequent rows alternate in the alignment in order to produce a zero net magnetization (Fig. 6.10b). When the external field is reversed, the ferromagnetic spins start to rotate until they are in opposite direction to the antiferromagnet (Fig. 6.10c-d). The spins in the ferromagnet have only one stable orientation, *i.e.* that the anisotropy is unidirectional. This means that a higher and lower external field, compared to a single ferromagnetic layer, is needed to align the spins parallel and antiparallel, because the antiferromagnet either prefers or opposes the alignment, respectively [**81**].

The strength of the exchange bias is for all observed systems inversely proportional to the ferromagnetic layer thickness. There is a strong indication that this phenomenon is a pure interface effect [**81**]. Although the antiferromagnetic ordering in a bulk antiferromagnet is due to a super exchange [**82**] mediated by the oxygen atoms, the reason for the exchange bias is not yet clear. At a metal-oxide/metal interface, both coupling mechanisms, *i.e.* indirect over the oxygen atoms or direct over the metal atoms is possible [**83**].

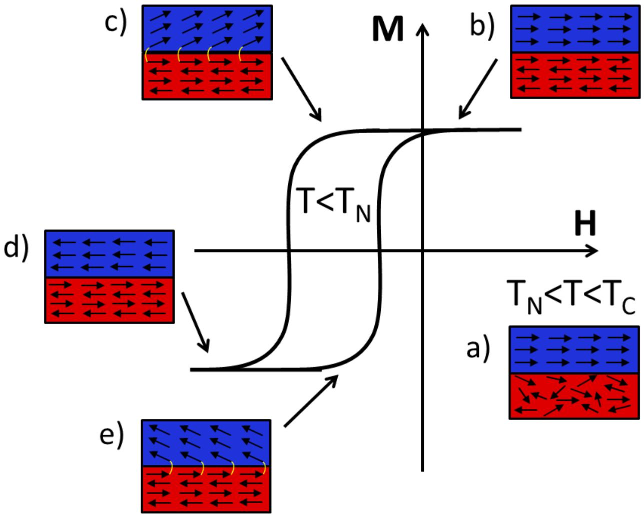

Fig. 6.10: Change of the spin orientation of an AF(red)/F(blue) bilayer during cooling in an external field and driving an external field, (according to [81]). The indicated curve is for *H* parallel to the easy direction.

The first mathematical description of the phenomenon was done by Meiklejohn in 1962 [**84**]. The shift of the hysteresis loop is thereby given by $H_E = \frac{J}{aM_S t}$, where J is the exchange coupling constant, originating from the interface between the F and AF layer, M_S is the saturation magnetization of the F-layer, t is the thickness of the F-layer, and a the lattice constant of the ferromagnet. However, the strength of the exchange bias field obtained in this way is an order of 10-100 too large when compared with experimental values [**85**].

The model holds for the case of uncompensated spins, *i.e.* the interface between the AF and F is formed by {111} planes of the AF, in which all spins have the same alignment, and the ferromagnetic layer has a net magnetic moment. However, if the interface of the antiferromagnet is build-up of a {100} plane, the net magnetic moment of the antiferromagnetic interface layer is zero. Nevertheless, for this case of compensated spins, an exchange bias effect can be observed, too [**85**]. In this case the exchange bias phenomenon may be explained by a random interface roughness, giving rise to a unidirectional anisotropy, whose magnitude is in accordance with the measured one [**86**].

In experiments both crystal orientations, *i.e.* the {001} and {111} planes, parallel to the interface yield an exchange bias with nearly the same strength [**87**]. Although there are various models, trying to explain the exchange bias phenomenon, there is still no satisfactory explanation. The reason for this is that various different mechanisms are contributing to the magnitude of H_E, such as the interface roughness, crystallinity, non-bulk properties, spin orientation, and stress gradients due to a lattice constant mismatch [**81**].

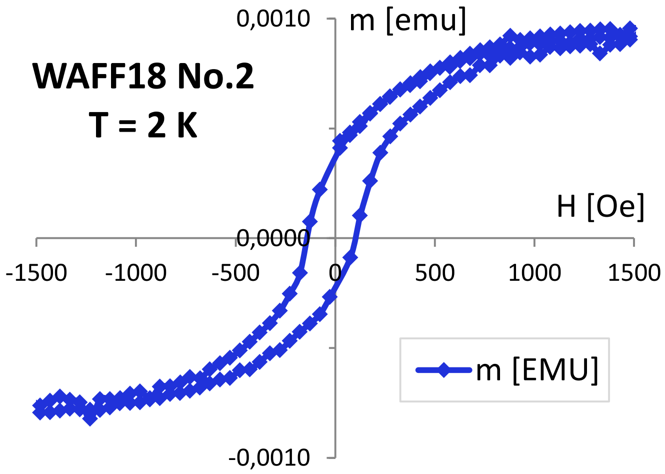

Fig. 6.11: Hysteresis measurement of sample WAFF18 No. 2. The sample consists of an antiferromagnetic cobalt oxide (Co_3O_4) pinning layer and a copper-nickel ($Cu_{41}Ni_{59}$) alloy layer. A small exchange bias is visible.

The hysteresis curve in Fig. 6.11 was measured for sample WAFF18 No.2 which was cut from a specimen where an F-wedge was deposited on top of an AF-layer of constant thickness. The sample consists of a cobalt oxide (Co_3O_4), layer, on top of which a layer of copper nickel ($Cu_{41}Ni_{59}$) was deposited. From sample No. 1 of the same series, *i.e.* the sample just next to No. 2, the thickness of the cobalt oxide layer was determined by HRTEM to be about 16.1 nm, while the copper nickel layer was 50.8 nm thick. The hysteresis curve shows a small exchange bias shift of about 50 Oe. Thus, the exchange bias field is as large as 25 Oe. At a temperature of 400 K a field of 5 T was applied and then the sample was cooled down (field cooled, FC).

A much stronger exchange bias is observed for the cobalt/cobalt-oxide system in Fig. 6.12. The sample is from the series SFF1, where a niobium layer is deposited on the substrate, followed by a copper nickel ($Cu_{41}Ni_{59}$) layer. The next two layers are a cobalt layer with a cobalt oxide layer on top. The applied field during field cooling was 2 T. The hysteresis curve was measured at a temperature of 10 K, which is well above the critical temperature of the superconductor, thus avoiding a strong diamagnetic signal.

Because the deposition process of the cobalt oxide is kept in the same condition as for the other sample series, it can be assumed that again Co_3O_4 has been crystallized. However, it may be that at the interface between the Co_3O_4 and the cobalt layer a CoO layer has formed [**88**]. The reason for this may be a natural concentration gradient which builds up between a Co_3O_4 layer and a Co layer. Since the exchange bias phenomenon is an interface effect, the formation of a CoO interface layer formed by a solid state reaction [**89**] is a possible explanation for the strong exchange bias observed.

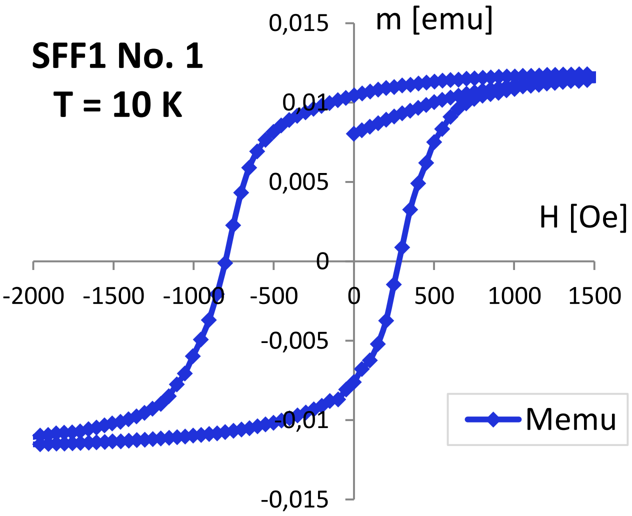

Fig. 6.12: Sample SFF1 No. 1, which is stack of $Nb/Cu_{41}Ni_{59}/Co/Co_3O_4$. The hysteresis measurement was made at a temperature of 10 K. The exchange bias arises from the Co/Co_3O_4 interface.

7. Superconducting Properties of the FFLO Like State

To study the superconducting properties, resistance versus temperature measurements have been made in a ^{3}He cryostat, where the temperature regime down to about 1.4 K was accessible with a 1 K-stage, operated with liquid ^{4}He, and a temperature of 380 mK was achievable by vapor pressure reduction of liquefied ^{3}He. Temperatures down to 40 mK were realized using a ^{3}He/^{4}He dilution refrigerator. The measuring current in the ^{3}He cryostat was 10 µA, whereas it was 2 µA in the dilution refrigerator. During the resistance measurements, the polarity of the measuring current has been altered for each measurement point, in order to avoid thermoelectric voltages.

In the following subchapters, first, the results of investigating F/S bilayers will be presented, afterwards those of S/F layers. Since the F/S/F core of the superconducting spin valve can be regarded as a combination of an F/S and S/F geometry, it is the next step of the investigations. In the last subchapter, the results on the AF-F/S/F spin valve, *i.e.* a four layer system with an antiferromagnetic pinning layer, will be given. The contents of chapters 7.1, 7.2 and 7.3 have been published in Refs. [**12**,**28**,**29**,**30**,**90**].

7.1. F/S bilayers

The transition curves of sample series FS 2406 are shown in Fig. 7.1. The series was cut from a ferromagnetic $Cu_{41}Ni_{59}$ wedge on which a 6.8 nm thick layer of niobium was deposited. The inset gives the ferromagnetic layer thickness of the different samples. The normal conducting resistivity was determined at 10 K. The superconducting transition temperature is evaluated from the midpoint of the resistance curves. The width of the superconducting transition was around 0.2-0.3 K.

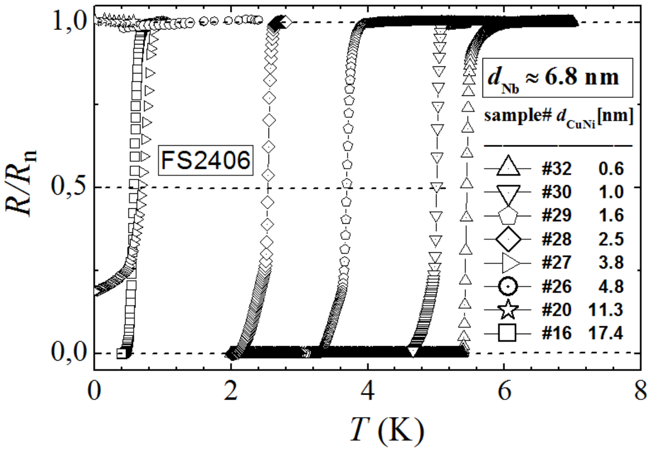

Fig. 7.1: Transition cures of series FS2406. The thickness of the superconducting niobium layer was 6.8 nm while the ferromagnet layer thickness changes, because the series was cut from a $Cu_{41}Ni_{59}$-wedge/Nb specimen (from [29]**).**

The transition temperature measurements for the F/S series FS 233, FS 2406, and FS 712 are shown in Fig. 7.2. All three sample series were cut from a $Cu_{41}Ni_{59}$-wedge/Nb specimen. The superconducting layer thickness differed for the sample series. The dashed lines give the theoretical fit to the experimentally measured points.

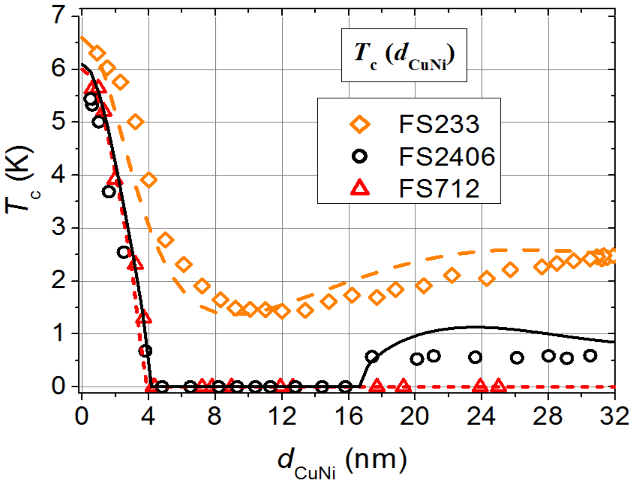

Fig. 7.2 Critical temperature T_c of sample series FS233, FS2406, and FS712, with d_{Nb}=7.5 nm, 6.8 nm and 6.3 nm, respectively (from Ref. [29]**).**

For sample series FS233, the thickness of the niobium layer was, d_{Nb} = 7.5 nm. For this series the superconducting transition temperature shows, first, a monotonic decrease until a minimum is reached, followed then, by an increase of the critical temperature.

Decreasing the thickness of the niobium layer to d_{Nb} = 6.8 nm (sample series FS2406) results in a decrease of the critical temperature to zero for a thickness of the copper-nickel alloy layer of about 4 nm. The extinction of superconductivity continues until a sample thickness of 17.4 nm, where superconductivity sets in again.

For the sample series FS712 the thickness of the niobium layer was further reduced to value of 6.3 nm, which is close to the thickness of 6.2 nm where no superconductivity is observed, if the thin film is covered by a sufficiently thick $Cu_{41}Ni_{59}$ layer, as discussed below. Thus, for samples of the FS712 series with a ferromagnetic layer thicknesses larger than 4 nm, superconductivity is suppressed.

In Fig. 7.3 the critical temperature variations of a sample series, cut from a specimen consisting of a wedge of niobium on top of a ferromagnetic $Cu_{41}Ni_{59}$ layer with a large thickness, is shown. The continuous green line gives the fit of the theory to the experimental values. Decreasing the thickness of the niobium layer reduces the transition temperature, until superconductivity is completely suppressed for a thickness of about 6.2 nm.

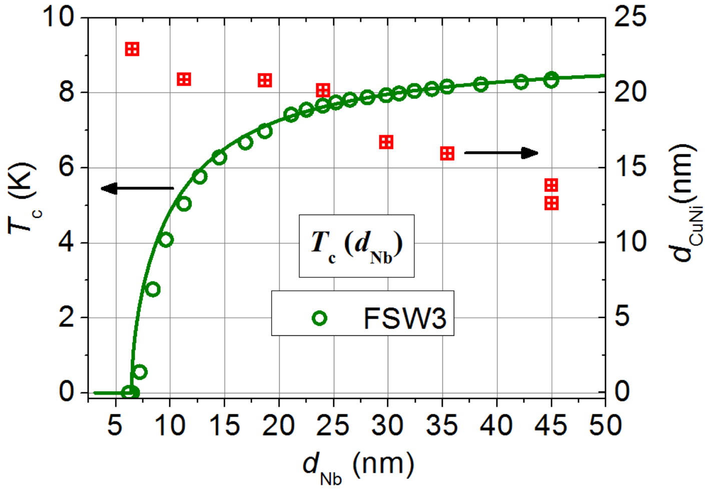

Fig. 7.3: Critical temperature of sample series FSW3, cut from a niobium wedge with a ferromagnetic layer on top (from [29]), the thickness of which is indicated by the right scale.

The steep decrease of the superconducting transition temperature for a niobium thickness smaller than 9 nm is the region of Nb layer thickness, for which one can observe deep critical temperature oscillations and reentrant behavior of superconductivity in F/S bilayers with fixed niobium layer thickness and variable F-layer thickness. The red squares are RBS measurements of the ferromagnetic layer thickness. The copper-nickel alloy thickness decreases from about 22.5 nm to 12.5 nm, while the niobium thickness is increasing. However, the main change of the copper-nickel thickness, from 21 nm to 12.5 nm, takes place in a region where the superconducting niobium film is less sensitive to a change of the ferromagnetic thin film layer, *i.e.* at the thick side of the niobium wedge. In the physically interesting region, ranging from a niobium thickness of 18.6 nm and a transition temperature of about 7 K to a thickness of 7.5 nm with a critical temperature of about 0.6 K, the copper-nickel alloy layer thickness varies only from 22.5 nm to 21 nm, which does nearly not affect the steep T_c decrease from which the critical thickness is extrapolated.

With the knowledge of the critical thickness, the number of variables which have to be fitted in the theory can be reduced, using Eq. (2.114) of Chap. 2.2.4. From Fig. 7.3 the value of the critical thickness, for which $\mathrm{T_c}\ d_{\mathrm{Nb}}^{\mathrm{cr}} = 0\,\mathrm{K}$, can be extrapolated to be 6.2 nm. Furthermore, using for the BCS coherence length a value of $\xi_{\mathrm{BCS}} = 42$ nm [**50**] and for the coherence length in the superconductor a value of $\xi_{\mathrm{S}} = 6$ nm, it is possible to calculate a constraint for the product of $N_{\mathrm{F}}v_{\mathrm{F}}/N_{\mathrm{S}}v_{\mathrm{S}}$ and T_{F}, giving

$$\frac{N_{\mathrm{F}}v_{\mathrm{F}}}{N_{\mathrm{S}}v_{\mathrm{S}}}\frac{1}{1+2/T_F} \approx 0.052 \tag{7.1}$$

In the above calculation, making use of Eq. (2.114), a value for the superconducting coherence length of $\xi_{\mathrm{S}} = 6$ nm was assumed. To obtain a first guess for this parameter, one has to measure niobium thin film samples in a perpendicular magnetic field, to get the upper critical field $B_{\mathrm{c}2\perp}$ as a function of temperature. From these measurements ξ_{S} is evaluated as described in detail in Chap. 2.2.4 (below Eq. (2.114).

Therefore, single niobium thin films are measured in a magnetic field perpendicular to the film surface. For $d_{\mathrm{Nb}} = 6.8$ nm and $d_{\mathrm{Nb}} = 14.0$ nm the slope of the critical field curve close to the critical temperature is straight, with $dB_{\mathrm{c}2\perp}(\mathrm{T})/\mathrm{d}T = 0.558$ T/K and 0.372 T/K, respectively. Following the calculation discussed in Chap. 2.2.4, gives a Ginsburg-Landau coherence length $\xi_{\mathrm{GL}}(0)=$ 9.7 nm and 10.5 nm, resulting in a superconducting coherence length $\xi_{\mathrm{S}} = 6.16$ nm and 6.68 nm, respectively.

In Fig. 7.4 the variation of the critical temperature on a decrease of the thickness of the superconducting niobium layer is measured for single Nb films of different thicknesses. The inset shows a cross sectional TEM image of the single niobium layer sample Nb No. 5. The niobium has a sharp interface to the adjacent silicon layers. The red curve represents a fitting to $T_{c0} = T_{c0Nb,Bulk} = \left[1 - d_1/d_s + \left(d_2/d_s\right)^2\right]$ with $T_{c0Nb,Bulk} = 9.3K$ [**91**], $d_1 = 2.07nm$ and $d_2 = 4\cdot 10^{-5}nm$. This figure gives us the possibility to get a value for the critical temperature of the Nb film in our bilayers in the “alone standing” case without the influence of a ferromagnetic film.

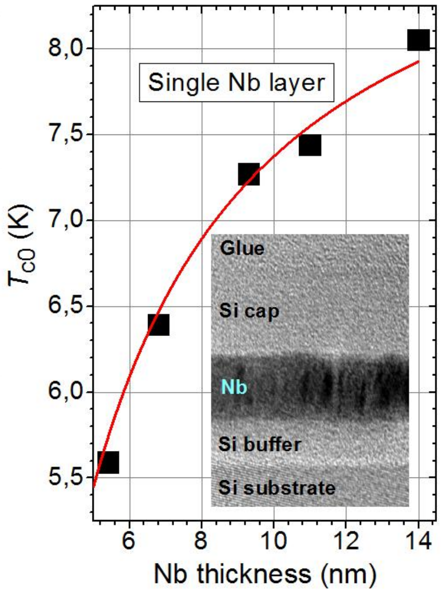

Fig. 7.4 Critical temperature decrease for decreasing thickness of the superconducting niobium layer. The inset shows a TEM image of the single niobium layer with d_{Nb}=6.8 nm. The full red curve is given in the text (from [28]).

The parameters left for a consistent fitting are, the superconducting coherence length ξ_S, the magnetic coherence length ξ_{F0}, and the electron mean free path of the conduction electrons, l_F in the ferromagnet, the ratio of the Sharvin conductances $N_F v_F/N_S v_S$ at the F/S interface, and the transparency parameter T_F. The last two parameters can, however, only be varied within the constraint of Eq. (7.1) given above. The experimental measurement points in Fig. 7.3a,b) have been fitted with the parameters given in Table 1, where attention was paid, that the parameters do not vary more than 10-15% from one series to another.

In Fig. 7.3a) for the sample series FS 2406 the theoretical values deviate from the experimental ones for copper-nickel thicknesses larger than 16 nm. It seems that the interference conditions are disturbed and a full recovery of the superconducting transition temperature was not possible. The reason for this might be the presence of lateral inhomogeneities of the nickel concentration or interface roughness. It gives an indication that the superconducting paring wave function is highly sensitive to any disturbances after a recovery from extinction.

In Table 1, the superconducting coherence length ξ_S has the same value for different niobium layer thicknesses. However actually, ξ_S depends on the electron mean free path, l_S, and on T_{c0} (via ξ_{BCS} as shown in Chap. 2.2.4), which have different values at different thicknesses of the superconducting Nb layer. In previous studies it could be shown, that these kind corrections have no essential impact on the fitting of these curves and may be neglected [**28**] (see also the next subchapter).

Moreover, the electron mean free path of the electrons in the ferromagnetic alloy, l_F, may vary over the thickness of the ferromagnetic wedge, especially at the thin side of the wedge. Since this variation is not known, it has not been considered.

Sample series	$T_{c0,Nb}$ (d_{CuNi}=0 nm)	ξ_S	$N_F v_F / N_S v_S$	T_F	l_F/ξ_{F0}	ξ_{F0}
FS233	6.6 K	6.0 nm	0.19	0.81	0.6	11.6 nm
FS2406	6.1 K	6.0 nm	0.20	0.88	0.6	10.4 nm
FS712	6.0 K	6.0 nm	0.20	0.82	0.7	10.8 nm
FSW3	8.9 K	6.0 nm	0.22	1.0	0.9	11.0 nm

Table 1: Overview over the fitting parameters used for the curves in Fig. 7.2 for sample series FS233, FS2406 and FS712 an in Fig. 7.3 for sample series FSW3.

7.2. S/F bilayers

In order to set a constraint on the fitting parameters, *i.e.* to reduce the amount of free parameters, also for the case of S/F bilayers a $T_c(d_S)$ dependence was measured. Contrary to the previous section on F/S bilayers, in the case of S/F bilayers a physically infinitely thick ferromagnetic layer of constant thickness was placed on top of the niobium wedge. Two different series have been produced WNb and WNc, where the thickness of the ferromagnetic layer on top of the superconducting wedge was 56 nm, i.e. physically infinite, and 25 nm thick, respectively. From Fig. 7.5 the critical thickness at which superconductivity vanishes can be determined, resulting in $d_{Nb}^{cr} = 6.0\ nm$. The shadowed area indicates the niobium thickness where deep oscillations of the critical temperature and even reentrant superconducting behavior can be expected.

Measurements of the critical temperature as a function of the ferromagnetic copper-nickel alloy layer thickness are given in Fig. 7.6. The solid line is the result obtained from the theory fitted to the experimental measurement points.

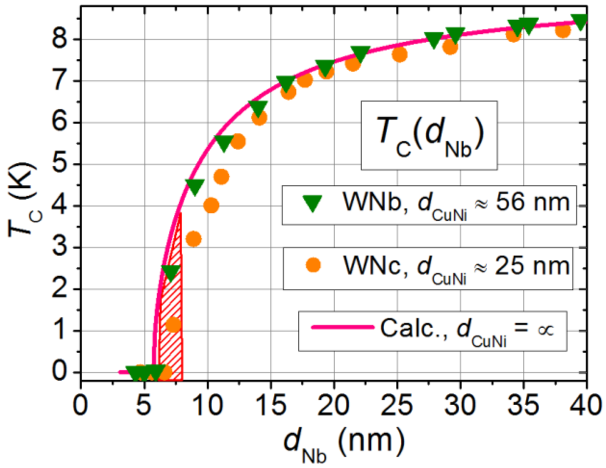

Fig. 7.5: The figure gives the critical temperature as a function of the niobium layer thickness. Two sample series have been produced. In the case of series WNc, the ferromagnetic layer thickness, which was deposited on top of the ferromagnet was 25 nm thick, while for WNb the thickness was 56 nm. The last one can be treated as physically infinite thick (form Ref. [28]).

For the thickest niobium layer (series S23), where d_{Nb}=14.1 nm, the oscillation of the critical temperature has only a slight minimum. This kind of shallow minimum has also been observed in other studies [**92**,**93**,**94**,**95**,**96**,**97**,**98**,**99**,**100**,**101**].

Decreasing the thickness of the niobium layer to d_{Nb}=8.3 nm and d_{Nb}=7.8 nm, for sample series S16 and S22, respectively, shows the non-monotonic behavior of the transition temperature much more clearly, with a distinct minimum at a cooper-nickel layer thickness of 7.0 nm and 7.9 nm, respectively.

For a niobium layer with a superconducting layer thickness of 7.3 nm (S15), first the superconducting temperature decreases rapidly, until it is completely suppressed for a thickness of 3.8 nm. In the following region of suppression, superconductivity could not be found, at least not down to temperatures of 40 mK, which was the lowest measuring temperature of the samples in the dilution cryostat. Superconductivity recovers again for ferromagnetic layer thicknesses larger than 12.8 nm, and the critical temperature increases to about 2.2 K until a decrease below 2 K is again observed.

For sample series S21 the niobium layer is thinnest, with a value of 6.2 nm. Again the superconducting transition temperature decreases rapidly until it vanishes for a ferromagnetic layer thickness of about 4 nm. But this time the range in which superconductivity is suppressed is much broader. A reentrance is observed for a thickness of 24 nm. This time superconductivity reaches only a critical temperature of about 0.9 K, until it decreases again and is suppressed, a second time, for $Cu_{41}Ni_{59}$ layer thicknesses larger than about 37 nm.

In summary, in Fig. 7.6 all different types of non-monotonous behavior, which are predicted by the theory [**22**], are present.

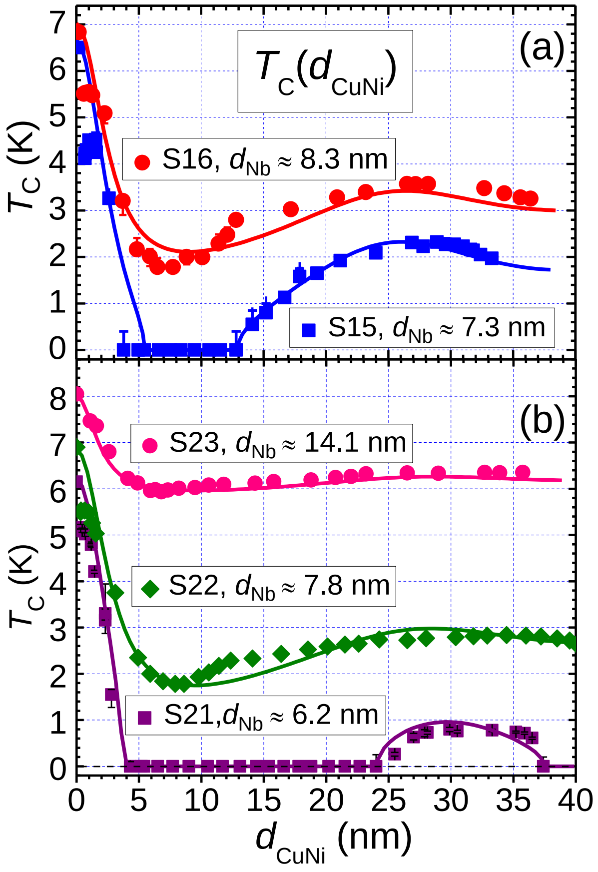

Fig. 7.6: Measurements of the critical temperature as a function of increasing ferromagnetic layer thickness. The measurement points are given as dots, the fit from the theory is given by the solid line (from Ref. [28**]).**

In Table 2 an overview over the fitting parameters, used for the theoretical curves shown in Fig. 7.6, is given. The experimental data points, *i.e.* the $T_c(d_{CuNi})$ behavior for different thicknesses of the niobium layer, could be reproduced quite well by the theory, using the tabulated values. The critical temperature $T_{c0Nb}(d_{CuNi}=0\text{ nm})$ were taken from Fig. 7.4. The superconducting coherence length in the dirty superconductors, ξ_S, has been decreased a little bit for decreasing niobium layer thickness, because a small reduction is expected for decreasing niobium layer thickness and, thus, decreasing electron mean free path, l_S, according to the theoretical expression, as e.g. given in Chap. 2.2.4 (Eq. 2.95). In detail a change of $\xi_S(l_S,T_{c0})$ and $\xi_{BCS}(T_{c0})$, where $T_{c0}=T_{c0}(d_{Nb})$ with changing niobium layer thickness was not considered, as in the case of F/S bilayers discussed in Chap. 7.1. For the fitting a value of the BCS coherence length, ξ_{BCS}, of 42 nm was taken [**50**]. The mean free path of the conduction electrons in the ferromagnet, which was used in our calculations, was $l_F \approx 11.8 - 12.4$ nm. This is close to the values for the coherence length in the ferromagnet, $\xi_{F0} = 9.5 - 11.2$ nm. This indicates that our samples are between the dirty ($l_F << \xi_{F0}$) and clean ($l_F >> \xi_{F0}$) limit.

Sample series	$T_{c0,Nb}$ (d_{CuNi}=0 nm)	ξ_S	$N_F v_F / N_S v_S$	T_F	l_F/ξ_{F0}	ξ_{F0}
S15	6.67 K	6.3 nm	0.22	0.67	1.3	9.5 nm
S16	7.0 K	6.4 nm	0.22	0.66	1.3	9.5 nm
S21	6.2 K	6.1 nm	0.22	0.65	1.1	11.2 nm
S22	6.85 K	6.5 nm	0.22	0.61	1.1	10.7 nm
S23	8.0 K	6.6 nm	0.22	0.44	1.1	10.8 nm

Table 2: Overview over the parameters used for fitting the full curves in Fig. 7.6.

For a $Cu_{47}Ni_{53}$ alloy bulk material, which has a similar atomic composition as the present $Cu_{41}Ni_{59}$ alloy, the electron mean free path was determined to be, $l_F \approx 4.4$ nm, and the resistivity $\rho_F = 57$ μΩ·cm, both at 10 K [**102**]. Low temperature measurements on our samples of the present alloy gives a specific resistivity $\rho_F \approx 25$ μΩ·cm [**34**]. Since the product of the specific resistivity and the mean free path may assumed to be constant when impurities are added [**103**], the mean free path resulting for our samples is $l_F \sim 10$ nm, which is close to the values obtained above. Thus, also the resistivity measurements verify that the ferromagnetic layer can neither be treated as dirty nor as clean but represents the intermediate case.

In Refs. [**12**,**34**,**90**], the fitting of the $T_c(d_F)$ and $T_c(d_S)$ curves was made with a value for the superconducting coherence, ξ_S, of about 10 nm. However, from measurements of the upper critical field an improved value for ξ_S could be determined, ranging between 6.2 nm and 6.7 nm, as already mentioned above. For ξ_S~10 nm, the parameters used to fit the measurements of Fig. 7.6 were, $\xi_S = 9.6 - 11.0$ nm, $N_F v_F / N_S v_S = 0.17 – 0.23$, $T_F = 0.43\text{-}0.85$, $l_F/\xi_{F0} = 1.1 - 1.2$, and $\xi_{F0} = 8.6 - 11.0$ nm. Comparing these fitting parameters with those given in Table 2, shows that the values are similar. This demonstrates that the phenomenon is not very sensitive to variations in the superconducting coherence length, ξ_S.

In the case of the S/F samples, the results for the fitting parameters are comparable to those obtained for F/S samples. However, in detail there are some differences. First, the transparency values for the F/S bilayers are about 1.4 times higher than the values obtained for the S/F bilayers. Furthermore, the ratio l_F/ξ_{F0} is about two times smaller, and the mean free path of the conduction electrons in the ferromagnet is about a factor 1.6-1.9 smaller. Comparing the appearance of the minimum of the oscillation of the transition temperature $T_c(d_{CuNi})$ shows, that it is located at d_{CuNi}=10 nm for F/S bilayers (see FS233), whereas, the value for S/F bilayers is somewhat smaller, with 7-8 nm. It may be that this observation indicates, that for S/F bilayers the exchange energy is somewhat larger compared to F/S bilayers, because due to the theory the minimum should appear at a fixed ratio of d_F/ξ_{F0} [**22**]. This means that a reduced d_F indicates a decrease of ξ_{F0}. The coherence length in the ferromagnet is, however, linked to the exchange field via, $\xi_{F0} = \hbar v_F / E_{Ex}$, *i.e.* decrease of ξ_{F0} may result from an increase of E_{ex}.

7.3. F/S/F Trilayers

Two different types of trilayer sample series have been prepared (see Fig. 3.5 and Fig. 3.6 of Chap. 3.2). The first one results from a double wedge structure, *i.e.* a superconducting layer of constant thickness is enclosed by two ferromagnetic wedges, which have the same or similar slope and thickness. Sample series FSF3 and FSF5 have been prepared in this way. The other type of sample series results from a single wedge geometry, *i.e.* the superconducting layer is deposited on a ferromagnetic layer of constant thickness. On top of the superconducting layer a wedge of ferromagnetic alloy was placed. From this kind of structure, sample series FSF1 and FSF2 have been prepared.

In Fig. 7.7a) and b) the transition temperatures for the series FSF2, FSF1 and FSF3 and FSF5 are given, respectively. In Fig. 7.7a) the single wedge geometry series are shown. The bottom $Cu_{41}Ni_{59}$ alloy layer has a constant thickness of 6.2 nm for FSF2 and 9.0 nm for FSF1, respectively. For this kind of geometry, the transition temperature has been plotted as a function of the thickness of the upper layer. The niobium layer thickness was 10.9 nm for FSF1 and 15.5 nm for FSF2. In Fig. 7.7b) the results for the double wedge series are shown. The transition temperature is plotted as a function of the combined thicknesses of the bottom and top ferromagnetic alloy layer, *i.e.* $d_{CuNi\text{-}B}$+$\mathrm{d}_{CuNi\text{-}T}$. The thickness of the niobium layer was 12.8 nm and 15.5 nm for sample series FSF5 and FSF3, respectively. In both kinds of sample geometries an oscillation of the critical temperature as well as an extinction and reentrance of the superconducting state can be observed.

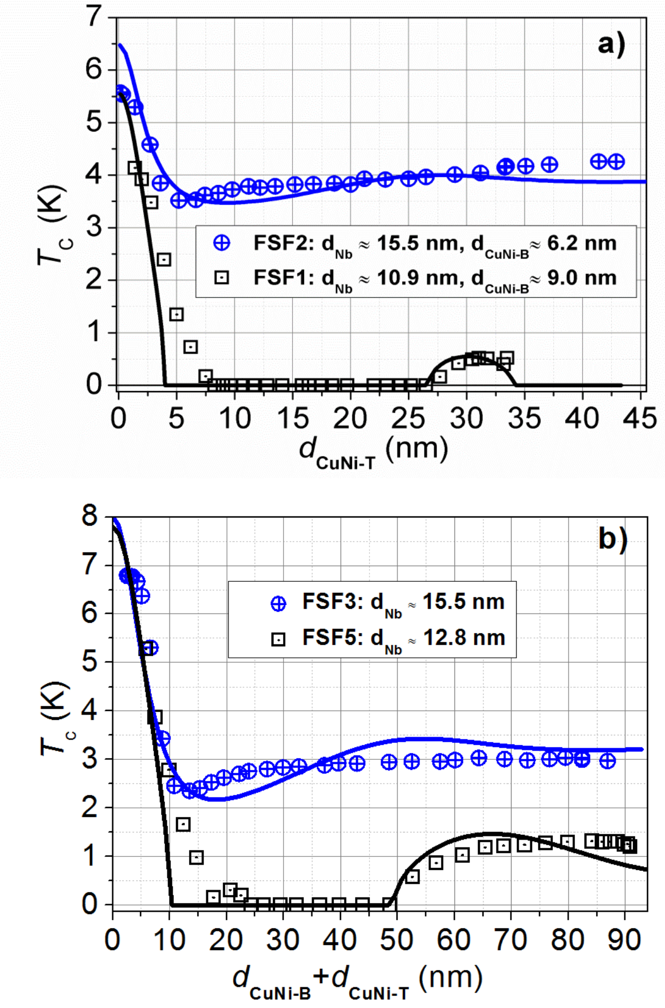

Fig. 7.7: a) Transition temperature measurements as a function of the ferromagnetic layer thickness from Ref. [30]**. In the case of the single wedge geometry series FSF1 and FSF2 the measurements were plotted as a function of the top $Cu_{41}Ni_{59}$ alloy layer thickness, $d_{\text{CuNi-T}}$. b) Transition temperatures of F/S/F trilayers as a function of the ferromagnetic layer thickness for double wedge geometry series, where the transition temperature has been plotted as a function of the sum of the thicknesses of the bottom and top $Cu_{41}Ni_{59}$ alloy layers, $d_{\text{CuNi-B}}+d_{\text{CuNi-T}}$ (from** [30]**).**

For sample series FSF5 the thickness of the top and bottom ferromagnetic alloy layers are equal (see Fig. 3b) of Ref. [**30**]). For series FSF3 there is a small difference between the thickness of the top layer, $d_{\text{CuNi-T}}$, and the thickness of the bottom layer, $d_{\text{CuNi-B}}$. While, for sample #1 and #19, the top layer has a thickness of 47.4 nm and 14.7 nm, the values for the bottom layer are $d_{\text{CuNi-B}}$=39.5 nm and 12.4 nm, respectively (compare Fig. 4.5 of Chap. 4.1.2).

The results can be compared with those of F/S and S/F bilayers, because trilayers can be considered as a F/S-S/F stack, when the thickness of the niobium layer is divided by 2. The thickness of the superconducting layer of FSF3 and FSF5 is 15.5 and 12.8 nm, respectively and, thus, the obtained results may be compared with those of bilayers with 7.8 nm and 6.4 nm Nb layer thickness. For S/F bilayers as well as for F/S bilayers indeed an oscillation of the critical temperature was observed for niobium layer thicknesses of about 8 nm, while an extinction and recovery of superconductivity, i.e. a reentrant behavior, was observed for thicknesses of about 6 nm. Furthermore, the range of the ferromagnetic layer thickness where superconductivity is suppressed for sample series FSF5 is comparable to that one of bilayers, if the average of the thickness of the top and bottom ferromagnetic layer is taken, $d_{\mathrm{CuNi,\ AV}} = (1/2)(d_{\mathrm{CuNi\text{-}B}} + d_{\mathrm{CuNi\text{-}T}})$. For sample series FSF3 the minimum of the transition temperature is close to $d_{\mathrm{CuNi,\ AV}} = 6.8$ nm, which is in accordance with the results obtained from S/F bilayers.

Sample series	$T_{\mathrm{c0,Nb}}$ (d_{CuNi}=0 nm)	ξ_S	$N_F v_F / N_S v_S$ Top/Bottom	T_F Top/Bottom	l_F/ξ_{F0} Top/Bottom	ξ_{F0} Top/Bottom
FSF 1	7.55 K	6.0 nm	0.22/0.19	0.77/0.40	1.1/0.65	11.4/10.8 nm
FSF 2	8.0 K	6.5 nm	0.22/0.19	0.61/0.45	0.92/0.61	10.8/11.6 nm
FSF 3	8.0 K	7.0 nm	0.22/0.20	0.68/0.6	0.68/0.6	10.8/11.6 nm
FSF 5	7.8 K	6.4 nm	0.21/0.19	0.83/0.68	1.0/0.65	12.8/14.4 nm

Table 3: Overview over the fitting parameters used for the curves of the theoretical predictions for FSF1, FSF2, FSF3, and FSF5 in Fig. 7.7.

A comparison of the results obtained for the single wedge geometry series FSF1 and FSF2 with bilayers, is just possible for one sample of the FSF series, where the thickness of the upper layer is equal to that of the lower layer, because only for this sample the F/S-S/F mirror symmetry is conserved. The lower ferromagnetic layer has a constant thickness of 9.0 nm and 6.2 nm for series FSF1 and FSF2 and the niobium thicknesses are 10.9 nm and 15.5 nm, respectively. For bilayers, this corresponds to a Nb layer thickness of 5.5 nm and 7.7 nm. For series FSF1 with a reentrant behaviour of the superconducting state, a copper-nickel thickness of $d_{\mathrm{CuNi\text{-}T}}$=9.0 nm is in the extinction region. For series FSF2, showing an oscillation of T_c, $d_{\mathrm{CuNi\text{-}T}}$ =6.2 nm, corresponds to the minimum of the T_c oscillation. Considering the Nb layer thickness of the samples, these observations are in agreement or close to the results obtained for S/F bilayers.

A summary of the fitting parameters used for the curves in Fig. 7.7 is given in Table 3. For the bottom and the top layer different fitting parameters have been used. This takes care of the fact, that for the ferromagnetic layer different growth conditions were present during the deposition, because the lower ferromagnetic layer grows on amorphous silicon, whereas the upper one grows on polycrystalline niobium. The parameters used for the fit are in the range of the parameters obtained for S/F and F/S bilayers.

7.4. Spin Valve

After having successfully demonstrated the non-monotonic behavior of the transition temperature of the FSF spin valve core structures (see Chap. 7.3), as a last step a fourth, antiferromagnetic cobalt oxide layer is introduced into the system. It can be placed either on top of the stack of thin film layers, or at the bottom, next to the silicon buffer layer (see Fig. 3.7 in Chap. 3.3). The ferromagnetic layers were deposited as a double wedge while the thickness of the cobalt oxide layer was kept constant. The sample series AF-FSF4 and AF-FSF5a have a niobium layer of constant thickness of 13.4 nm and 11.3 nm, respectively.

The $T_c(d_F)$ measurement of samples which consist of the last mentioned geometry are shown in the following two figures. The $T_c(d_F)$ curve of the sample series with the thicker niobium layer, AF-FSF4, plotted in Fig. 7.8, shows a deep oscillation.

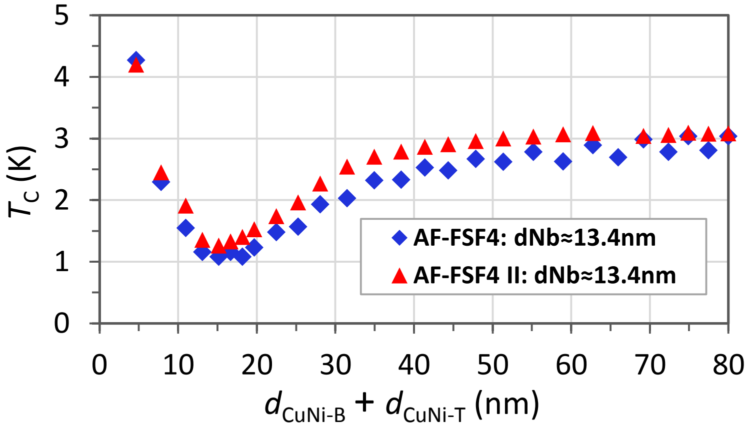

Fig. 7.8: Critical temperature measurement of the four layer system AF-FSF4 as a function of the sum of the thickness of the bottom and top $Cu_{41}Ni_{59}$ alloy layers. The thickness of the niobium layer is 13.4 nm.

The red triangles in Fig. 7.8 correspond to a measurement which has been made one month after the first one (marked with the blue diamonds).

In Fig. 7.9, the $T_c(d_F)$ measurements of sample series AF-FSF5a were made at three different dates. The first one, in September 2010, shows a complete extinction of superconductivity. The next one, made one month later, exhibits reentrant superconductivity. The last measuring session, in March 2011, indicates a change from reentrant superconductivity to an oscillatory behavior.

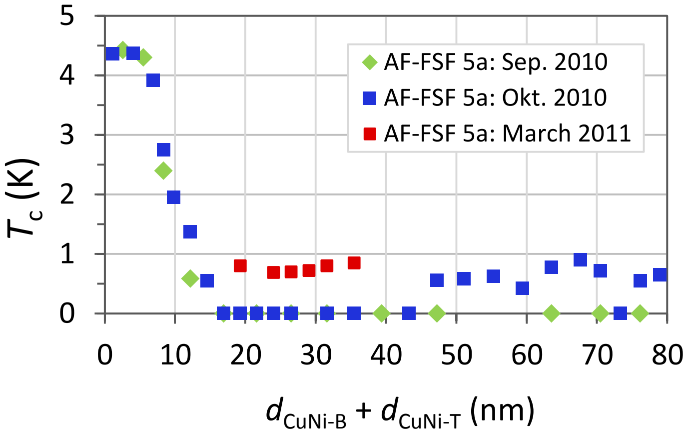

Fig. 7.9:. Critical temperature measurement of the four layer system AF-FSF5a as a function of the sum of the thickness of the bottom and top $Cu_{41}Ni_{59}$ alloy layers. The thickness of the niobium layer is 11.3 nm.

The results are similar to those obtained for trilayer samples, see *e.g.* Fig. 7.7b), where a slight oscillation of the critical temperature was observed for the case of a thicker niobium layer with 15.5 nm and an extinction and recovery of superconductivity for a niobium layer of 12.8 nm, *i.e.* a thickness which is in between the values of the curves shown above. As expected from these measurements, at a copper nickel thickness $d_{\text{CuNi-B}}+d_{\text{CuNi-T}}$ of around 12 nm the beginning of the extinction region of a reentrant behavior is observed.

The appearance of a strong oscillation and a reentrant behavior is promising for a large spin valve effect, as described in Chap. 2.1.

The aging effects may be due to a diffusion of oxygen from the cobalt oxide layer towards the niobium layer. This seems to change the transparency at the F/S interface. To avoid this, one may introduce a thin niobium layer between the cobalt oxide and the ferromagnetic layer. A solid state reaction may then capture the diffusing oxygen.

An alternative spin valve structure is obtained, when the antiferromagnetic layer is placed on top of the spin valve structure. Depositing this structure with an average niobium layer thickness of 12.0 nm yields a shallow T_c oscillation, shown in Fig. 7.10. Comparing this result with the trilayers in Fig. 7.7b) shows that at an average niobium thickness of 12.8 nm an extinction and recovery of superconductivity can be expected. However, a detailed analysis of the RBS data of the thickness gives the indication that, during the preparation process, something unusual happened. It seems that the cobalt oxide layer is not constant but increases from 3.3 nm to 21.3 nm over the sample series, along with the increasing thickness of the ferromagnetic layers. An increase of the cobalt oxide layer should not be important when considering the $T_c(d_F)$. However, changes in the ferromagnetic

$Cu_{41}Ni_{59}$ or superconducting Nb layer thickness have strong influence, especially if they are located at the thin side of the ferromagnetic wedge. Therefore, the thickness of the Nb layer should be kept as constant as possible in this type of sample series. This is, unfortunately, not the case in this series.

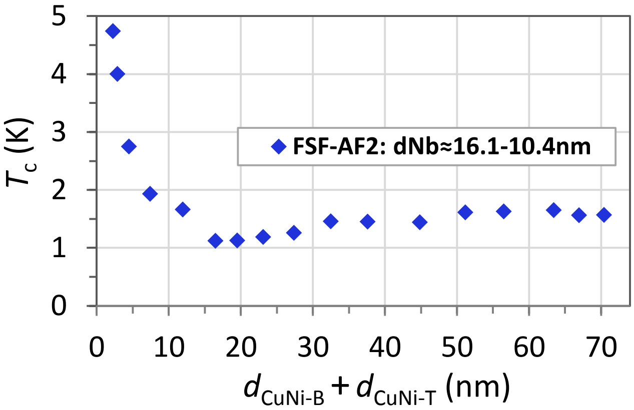

Fig. 7.10: Measurement of the transition temperature of series FSF-AF2 as a function of the combined lower and upper ferromagnetic layer thickness. The average thickness of the niobium layer is 12.0 nm.

For the first three samples shown, the critical temperature drops rapidly to 2.75 K while the Nb layer has a thickness of about 16.1 nm. For the next three samples the Nb layer thickness decreases to a value of 11.5 nm. In the range of these six samples the thickness of the top ferromagnetic layer increases strongly from about 1 nm to about 9 nm and the bottom layer from about 3 nm to 8 nm. So the decrease of the critical temperature, in this region, appears due to a decrease of the niobium layer thickness and a strong increase of the top and bottom ferromagnetic layer thickness. For the rest of the sample the ferromagnetic layer thickness increases monotonously from 11.3 nm to 41.7 nm, for the top layer and from 9.7 nm to 32.2 nm for the bottom layer, whereas the superconducting layer thickness is constant at a value of about 10.9 nm.

To demonstrate the superconducting spin-valve effect, the critical temperature should be measured for parallel and antiparallel magnetization direction of the ferromagnetic layers. Therefore, the magnetization direction of one of the layers has to be changed by an external field.

In order to keep the magnetization direction of the other magnetic layer constant, an exchange bias between the ferromagnetic layer and the antiferromagnetic layer has to be induced. Therefore, the samples are first exposed to a magnetic field, of *e.g.* 3 T, and a temperature above the Néel temperature. Then the samples are cooled down, with the applied field, to low temperatures.

The largest spin valve effect is expected in a region where the sample series exhibit a minimum of T_c or a transition to an extinction of the superconducting state for the case of a reentrant behaviour. For the series AF-FSF4, sample No. 29 with $d_{CuNi\text{-}B}+d_{CuNi\text{-}T}$=11.0 nm fulfills this condition because its critical temperature is in the environment of the minimum of the $T_c(d_F)$ dependence (see Fig. 7.8).

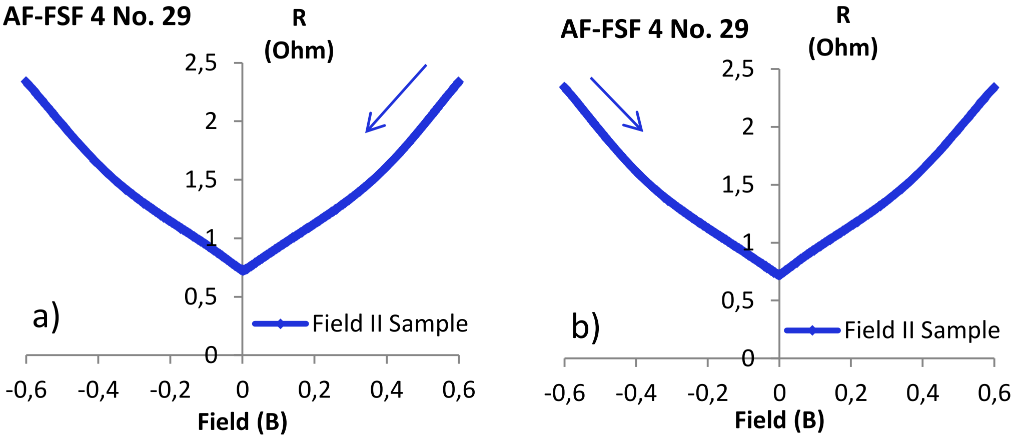

Fig. 7.11: For sample AF-FSF4 No. 29 the temperature was set to 2 K and the magnetic field was swept in the range between -0.6 T and +0.6 T. In a) the magnetic field declines from +0.6 T while in b) the magnetic field was increased from -0.6 T to +0.6 T.

To demonstrate the effect, critical temperature measurements have to be performed in magnetic fields parallel to the plane of the sample, applying the field into two opposing directions. For a first test, however, the following method may be applied: The temperature is fixed to a value within the transition, where the sample is resistive. Then a magnetic field, B, is applied and the resistance of the sample is observed as a function of B. Because the magnetic field shifts the superconducting transition towards lower temperatures, usually an increase of $R(B,T=const.)$ is expected. In our “spin-valve samples”, however, the critical temperature should, moreover, depend on the relative orientation of the magnetization of the ferromagnetic layers. If the magnetizations are parallel, the critical temperature should be lower compared to the antiparallel case. Therefore, a decrease of the resistance $R(B,T=const.)$ is expected, when the sample changes from the region of parallel magnetization to the antiparallel case. For high fields B, in the “positive” direction, the magnetization should be parallel. Reducing the, absolute value of B and then increase it again in the negative direction should lead to a certain range for negative values of B, in which the magnetizations are antiparallel. The reason is that first the direction of the magnetization of the ”free” not exchange biased layer changes the direction. For higher magnetic field values in the negative direction also the exchange biased magnetization turns around, so that finally both magnetizations are again parallel. Starting form high B in the negative direction, a similar behaviour is expected. However, now the range of antiparallel alignment should occur in a certain range of positive fields. Thus, one would expect a reduction of *R*(*B*,*T*=*const*.) for a certain negative field range, if one starts from high positive magnetic fields, whereas this reduction should appear in the positive field region, when starting from high magnetic fields. Such experiment was performed with sample No. 29 of the AF-FSF4 sample series.

The superconducting transition width, *i.e.* the difference in the temperature when 90 % and 10 % of the transition has occurred, of sample No. 29 of the AF-FSF4 series, is 0.2 K. The magnetic field was applied parallel to the plane of the film. The temperature was kept constant at 2 K, which is roughly the midpoint of the superconducting transition, while the magnetic field was changed, from 0.6 T to -0.6 T, (Fig. 7.11a) and afterwards increased again from -0.6 T to +0.6 T (Fig. 7.11b). However, the expected signature of the antiparallel alignment of the magnetizations is not seen. No spin valve effect seems to be present.

Because, before the measurement of sample No. 29, the magnetic field was changed a few times, due to measurements of different samples, no remanence field is present in the superconducting coil (see discussion below).

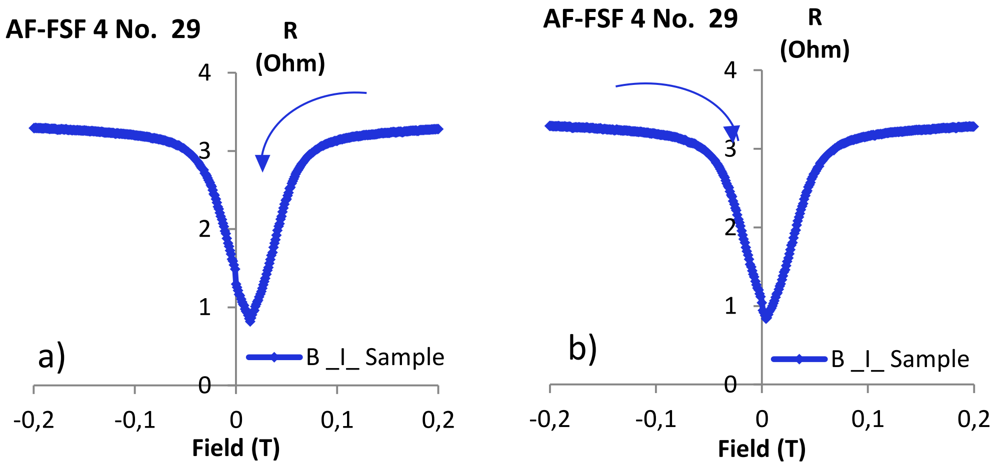

Fig. 7.12: Measurement of sample AF-FSF4 No. 29 in a perpendicular magnetic field at low temperatures, i.e. *T*=2 K.

Fig. 7.12In Fig. 7.12a) and b) the measurement of the sample has been repeated, but now the direction of the external magnetic field was perpendicular to the plane of the film. The temperature was kept constant at 2 K and the magnetic field changed from 0.2 T to -0.2 T in Fig. 7.12a) and then increased again from -0.2 T to +0.2 T in Fig. 7.12b). Comparing the position of the peak shows that there is some shift between both figures. However, changing the magnetic field between ±0.2 T several times decreases this shift. The reason for this may be that during cooling down in an applied field of 3 T, flux was trapped in the superconducting coil, leading to a remanence field. By changing the magnetic field in this way, the trapped flux is freed over time and the coil demagnetized.

The reasons for the absence of the spin-valve effect is probably that the exchange bias between the antiferromagnetic layer and the bottom ferromagnetic layer is only very weak. Then, there is no field range where the anitparallel alingment can occur.

8. Conclusion

In the present work, the Fulde-Ferrell Larkin-Ovchinnikov (FFLO) like state in superconductor/ferromagnet nano layered structures has been investigated. The samples were prepared in a special way by magnetron sputtering. During the deposition of layers of constant thickness, the target was moved in a circle above the substrate, in order to avoid inhomogeneities by intrinsic properties of the sputtering system. By this method it was possible to produce a homogenous and flat layer thickness. When sputtering wedge type layers, the sample was placed off axis from the symmetry axis of the magnetron, in order to use the natural sputtering gradient, to produce wedges with a constant slope, varying in the range between 40 nm and 0 nm. Cutting wedge type specimens into stripes perpendicular to the gradient of the wedge, yields series of samples which were deposited in the same run. As a superconducting material Nb was used and a $Cu_{41}Ni_{59}$ alloy as ferromagnetic one. The thickness of the layers was determined by Rutherford-Backscattering Spectrometry and Transmission Electron Microscopy. Furthermore, by Transmission Electron Microscopy it was possible to identify the lattice structure of the functional layers and determine the growth conditions during the deposition process.

At the beginning of the investigations, S/F bilayers have been deposited, where the F-layer was grown on top of the S-layer. The thickness of the functional S-layer was varied between 6.2 nm and 14.1 nm. It was possible to observe all kinds of non-monotonic behavior of the critical temperature predicted by theory. If the superconducting layer thickness is decreased from 14.1 nm, first a shallow oscillation of the critical temperature occurred for an increasing thickness of the ferromagnetic layer, which becomes more pronounced for decreasing S-layer thickness, so that a deep oscillation of the critical temperature is present. Finally, for the thinnest niobium layer, superconductivity vanishes before a reentrance of the superconducting state is observed.

In a next step, F/S bilayers have been fabricated, where the superconducting layer was deposited on top of the ferromagnetic material. Because the growth conditions for niobium and copper-nickel are different compared to the S/F layer, it was a milestone to demonstrate successfully deep oscillations of the superconducting transition temperatures and a reentrant superconducting behavior in this kind of samples.

Consequently, the experiences in depositing F/S and S/F layers could now be used to fabricate the spin valve core structure, i.e. a F/S/F trilayer, for which the theory predicts a higher critical temperature for antiparallel alignment of the magnetizations, compared to the parallel case. Two different types of trilayer geometries have been fabricated. Mirror symmetric sample series cut from a specimen, where a niobium layer of constant thickness is enclosed between two ferromagnetic wedges, and the other kind of samples where the Nb layer is grown on a ferromagnetic layer of constant thickness, while the second ferromagnetic layer is deposited as a wedge on top of the niobium layer. In both cases it was possible to observe the oscillations of the critical temperature as well as an extinction and reentrance of superconductivity.

Finally, the spin valve structure has been deposited by adding to the F/S/F core structure an antiferromagnetic layer (cobalt oxide) in order to keep the orientation of the magnetization of one F-layer fixed, while the orientation of the magnetization of the other one is changed by an external magnetic field. In this way it should be possible, for an optimal set of ferromagnetic and superconducting layer thickness to achieve a spin switching effect as large as 1-2 K. When no magnetic field was applied to the samples, one could observe deep critical temperature oscillations as well as an extinction and recovery of superconductivity. However, it was not possible to achieve a pinning of one of the ferromagnetic layers while changing the orientation of the magnetization of the other one by an external magnetic field. Analyzing the cobalt oxide by RBS, HRTEM, and electron diffraction, led to the conclusion, that Co_3O_4 has been formed during the deposition process. Although, this kind of cobalt oxide is also an antiferromagnet, CoO is expected to produce a larger exchange bias. In the future, the oxygen partial pressure during the deposition process will be reduced in order to favor the formation of CoO. If the CoO layer can be grown in a suitable orientation, it is expected, that the exchange biasing of the ferromagnetic layer can be increased, so that the superconducting spin valve works.

9. Appendix

9.1. Decay Length and Oscillation Wave Length of the Superconducting Pairing Wave Function

a) In the dirty case, the decay length and the oscillation wavelength can be obtained from the work of Radović et al. [**21**]. The pairing wave function is given by $\Phi_F(d_F) \sim \exp(ik_M d_F)$, where $k_M = (1+i)(2/\xi_M)$ with $\xi_M = \sqrt{\frac{4\hbar D_M}{I_0}}$ according to Eq. (10) and (11) of that work. Here, $D_M \equiv D_F$ and $I_0 = \frac{E_{ex}}{2}$, so that $\xi_M = \sqrt{\frac{8\hbar D_F}{E_{ex}}}$.

Thus, $$\Phi_F\left(d_F\right) \sim \exp(i(1+i)\frac{2}{\xi_M} d_F) = \exp(i\frac{2}{\xi_M} d_F - \frac{2}{\xi_M} d_F) = \exp(i\frac{d_F}{\xi_{FD}} - \frac{d_F}{\xi_{FD}})$$

where $\xi_{FD} = \xi_M / 2 = \sqrt{\frac{2\hbar D_F}{E_{ex}}}$. The decay length of $\Phi(d_F)$ is thus given by ξ_{FD}. The oscillation wavelength $d_F = \lambda_{FD}$ is obtained by the condition $d_F / \xi_{FD} = 2\pi$, yielding $\lambda_{FD} = 2\pi\xi_{FD}$.

b) This result is also obtained from Ref. [**22**] for the case of a dirty ferromagnet. By a comparison of the argument of the "*tanh*()" in Eqs. (3.14) and (3.17) of that work one gets $\tilde{k}_{\mathrm{m}} = \left(2/\xi_M\right)(1+i)$, with ξ_M given in Eq. (3.18). Inserting $\tilde{k}_{\mathrm{m}}$ in

Eq. (3.13) yields the results for the decay length and oscillation wave length given above.

In detail the derivation is as follows. The decay length and oscillation wave length of the pairing wave function in the F-material can be derived from the paring wave function (Eq. (3.13) in Ref. [**22**])

$$F_m = C_1 \exp(\tilde{k}_m x) + C_2 \exp(-\tilde{k}_m x) \qquad (9.1)$$

Comparing Eq. (3.14) and Eq. (3.17) in Ref. [**22**] yields (see the argument in *tanh*())

$$\tilde{k}_m = \frac{2}{\xi_m}(1+i) \qquad (9.2)$$

According to Eq. (3.18) in [**22**]:

$$\xi_m = \sqrt{\left(\frac{4D_m}{I}\right)_{\hbar=1}} = \sqrt{\left(\frac{4\hbar D_m}{I}\right)_{\hbar=\hbar}} \qquad (9.3)$$

And according to p.147 of [**22**] it is $2I=E_{ex}$, yielding

$$\xi_m = \sqrt{\left(\frac{8\hbar D_m}{E_{ex}}\right)_{\hbar=\hbar}} \qquad (9.4)$$

Inserting (9.2) in (9.1) and setting $C_1 = 0$, because, otherwise one would get a solution which increases exponentially into the F-material, which is physically not reasonable, one gets,

$$F_m = C_2 \exp\left(-\frac{2}{\xi_m}(1+i)x\right) = C_2 \exp\left(-\frac{2}{\xi_m}x\right)\exp\left(-i\frac{2}{\xi_m}x\right) \qquad (9.5)$$

With $\xi_{FD} = \xi_m / 2$ it follows,

$$F_m = C_2 \exp\left(-\frac{x}{\xi_{FD}}\right)\exp\left(-i\frac{x}{\xi_{FD}}\right) \qquad (9.6)$$

Thus, one obtains the decay length of F_m

$$\xi_{FD} = \frac{\xi_m}{2} = \frac{1}{2}\sqrt{\frac{8\hbar D_m}{E_{ex}}} = \sqrt{\frac{2\hbar D_m}{E_{ex}}} \qquad (9.7)$$

The oscillation wave length $x=\lambda_{FD}$ is given by the condition $x/\xi_{FD}=2\pi$, so that

$$\lambda_{FD} = 2\pi\xi_{FD} \qquad (9.8)$$

Here (see Eq. (3.16) of Ref. [**22**]), $D_m = \frac{1}{3} v_{Fm}^2 \tau_m$ with $v_{Fm}\tau_m = l_m$, so that one obtains

$$D_m = \frac{1}{3} v_{Fm} l_m \tag{9.9}$$

where we kept the notation of Ref. [**22**]. In the present work it is written $\Phi_F(d_F)$ instead of F_m and, moreover, x is denoted by d_F and D_m by D_F, and v_{Fm} by v_F, and l_m by l_F. With that notation we get that the decay length of $\Phi_F(d_F)$ is $\xi_{FD} = \sqrt{\frac{2\hbar D_F}{E_{ex}}}$ and the oscillation wave length is $\lambda_{FD} = 2\pi\xi_{FD}$.

c) Moreover from Ref. [**22**] the values for the case of a clean ferromagnet can be derived. For this purpose $\tilde{k}_\mathrm{m}$ from Eq. (3.24) has to be inserted into (3.13) of that work, yielding $2l_F$ for the decay length and $\lambda_{F0}=2\pi\xi_{\mathrm{F0}}$ with $\xi_{\mathrm{F0}}=\hbar v_F/E_{\mathrm{ex}}$ for the oscillation wave length.

In detail the derivation is as follows. In the case of a clean ferromagnet according to Eq. (3.24) on p.156 of Ref. [**22**] one has

$$\tilde{k}_m = \pm\frac{2iI}{v_{Fm}}\left(1+\frac{1}{4iI\tau_m}\right) = \pm\frac{2iI}{v_{Fm}} \pm \left(\frac{1}{2v_{Fm}\tau_m}\right) = \pm\frac{2iI}{v_{Fm}} \pm \left(\frac{1}{2l_m}\right) \tag{9.10}$$

Inserting the “+” solution into Eq. (9.1) and setting C_1=0 (same reason as discussed above), yields

$$F_m = C_2 \exp\left(-\frac{1}{2l_m}x\right)\exp\left(-\frac{2iI}{v_{Fm}}x\right) = C_2 \exp\left(-\frac{x}{2l_m}\right)\exp\left(-i\frac{x}{\xi_{F0}}\right) \tag{9.11}$$

where

$$\xi_{F0} = \left(\frac{v_{Fm}}{2I}\right)_{\hbar=1} = \left(\frac{\hbar v_{Fm}}{2I}\right)_{\hbar=\hbar} = \left(\frac{\hbar v_{Fm}}{E_{ex}}\right) = \left(\frac{\hbar v_F}{E_{ex}}\right) \tag{9.12}$$

where in the last step the notation of the present work was introduced. Thus, it can be seen that the decay length of the pairing wave function is $2l_m$, which is equal to $2l_F$ in the notation of the present work. To get the oscillation wave length $x=\lambda_{\mathrm{F0}}$ one has to require that $x/\xi_{\mathrm{F0}} = 2\pi$. So the oscillation wave length is given by

$$\lambda_{F0} = 2\pi\xi_{F0} \tag{9.13}$$

References

[1] B. Nagel, *Nobel Lectures Physics*, Gosta Ekspong, Ed. Singapore: World Scientific Pub Co, 2003.

[2] P. Grünberg, "Magnetic Field Sensor With a Thin Ferromagnetic Layer," Patentnummer DE 3820475 (C1), Dec. 21, 1988.

[3] M.N. Baibich, J.M. Broto, A. Fert, F. Nguyen Van Dau, F. Petroff, P. Eitenne, G. Creuzet, A. Friedrich, and J. Chazelas, "Giant Magnetoresistance of (001)Fe/(001)Cr Magnetic Superlattices," *Phys. Rev. Lett.*, vol. 61, p. 2472, 1988.

[4] I. Zutic, J. Fabian, and S. Das Sarma, "Spintronics: Fundamentals and Applications," *Rev. Mod. Phys.*, vol. 76, p. 323, 2004.

[5] L. Tagirov, "Low-Field Superconducting Spin Switch Based on a Superconductor /Ferromagnet Multilayer," *Phys. Rev. Lett.*, vol. 83, p. 2058, 1999.

[6] L.N. Cooper and D. Feldman, Eds., *BCS: 50 years*. Singapore: World Scientific, 2011.

[7] J Bardeen, L.N. Cooper, and J.R. Schriefer, "Microscopic Theory of Supercondutivity," *Phys. Rev.*, vol. 106, p. 162, 1957.

[8] J. Bardeen, L.N. Cooper, and J.R. Schrieffer, "Theory of Superconductivity," *Phys. Rev.*, vol. 108, p. 1175, 1957.

[9] R. Ferrell and P. Fulde, "Superconductivity in a Strong Spin-Exchange Field," *Phys. Rev.*, vol. 135, p. A550, 1964.

[10] A.I. Larkin and Yu.N. Ovchinnikov, *Zh. Eksp. Teor. Fiz.*, vol. 47, p. 1136, 1964.

[11] A.I. Larkin and Yu.N. Ovchinnikov, "Inhomogenous State of Superconductors," *Sov. Phys. JETP*, vol. 20, p. 762, 1965.

[12] A.S. Sidorenko, V.I. Zdravkov, J. Kehrle, R. Morari, E. Antropov, G. Obermeier, S. Gsell, M. Schreck, C. Müller, V.V. Ryazanov, S. Horn, R. Tidecks, and L.R. Tagirov, *Extinction and Recovery of Superconductivity by Interference in Superconductor/Ferromagnet Bilayers, in Nanoscale Phenomena - Fundamentals and Applications*, A. Sidorenko, I. Tiginyanu, and H. Hahn, Eds. Berlin-Heidelberg: Springer, 2009, Chap. 1.

[13] P. Fulde, "High Field Superconductivity in Thin Films," *Adv. phys.*, vol. 22, p. 667, 1973.

[14] A. Bianchi, R. Movshovich, C. Capan, P.G. Pagliuso, and J.L. Sarrao, "Possible Fulde-Ferrell-Larkin-Ovchinnikov Superconducting State in CeCoIn5," *Phys. Rev. Lett.*, vol. 91, p. 187004, 2003.

[15] R. Lortz, Y. Wang, A. Demuer, P.H.M. Böttger, B. Bergk, G. Zwicknagl, Y. Nakazawa, and J. Wosnitza, "Calorimetric Evidence for a Fulde-Ferrell-Larkin-Ovchinnikov Superconducting State in the Layered Organic Superconductor κ-(BEDT-TTF)2Cu(NCS)2," *Phys. Rev. Lett.*, vol. 99, p. 187002, 2007.

[16] K. Gloos, R. Modler, H. Schimanski, C.D. Bredl, C. Geibl, F. Steglich, A.I. Buzdin, N. Sato, and T. Komatsubara, "Possible Formation of a Nonuniform Superconducting State in the Heavy-Fermion Compound UPd2Al3," *Phys. Rev. Lett.*, vol. 70, p. 501, 1993.

[17] H.K. Wong, B.Y. Jin, Q. Yang, J.B. Ketterson, and J.E. Hillard, "Superconducting Properties of V/Fe Superlattices," *J Low Temp. Phys.*, vol. 63, p. 307, 1986.

[18] A.I. Buzdin and M.Yu. Kupriyanov, "Transition Temperature of a Superconductor-Ferromagnet Superlattice," *JETP Lett.*, vol. 52, p. 487, 1990.

[19] Z. Radovic, M. Ledvij, L. Dobrosavljevic-Grujic, A.I. Buzdin, and J.R. Clem, "Transition Temperatures of Superconductor-Ferromagnet Superlattices," *Phys. Rev. B*, vol. 44, p. 759, 1991.

[20] K. Usadel, "Generalized Diffusion Equation for Superconducting Alloys," *Phys. Rev. Lett.*, vol. 25, p. 507, 1970.

[21] Z. Radovic, L. Dobrosavljevic-Grujic, A.I. Buzdin, and J.R. Clem, "Upper Critical Fields of Superconductor-Ferromagnet Multilayers," *Phys. Rev. B*, vol. 38, p. 2388, 1988.

[22] L. Tagirov, "Proximity Effect and Superconducting Tranisition Temperatures in Supercondcutor/Ferromagnet Sandwiches," *Physica C*, vol. 307, p. 145, 1998.

[23] B.P. Vodopyanov, L.R. Tagirov, H.Z. Durusoy, and A.V. Berezhnov, "The Influence of Alloying or Interdiffusion on the Superconducting Properties of Ferromagnet/Superconductor Layered Systems," *Physica C*, vol. 366, p. 31, 2001.

[24] Leonh. Eulero, "De progressionibus harmonicis observationes," in *Commentarii academiae scientiarum imperialis Petropolitanae 7.*, 1734.

[25] A.I. Buzdin, "Proximity Effects in Superconductor-Ferromagnet Heterostructures," *Rev. Mod. Phys*, vol. 77, p. 935, 2005.

[26] A. A. Golubov, M.Yu. KuriYanov, and E. Il'ichev, "The Current-Phase Relation in Josephson Junctions," *Rev. Mod. Phys.*, vol. 76, p. 411, 2004.

[27] F.S. Bergeret, A.F. Volkov, and K.B. Efetov, "Odd Triplet Superconductivity and Related Phenomena in Superconductor-Ferromagnet Structures," *Rev. Mod. Phys.*, vol. 77, p. 1321, 2005.

[28] V.I. Zdravkov, J. Kehrle, G. Obermeier, S. Gsell, M. Schreck, C. Müller, H.A. Krug Von Nidda, J. Lindner, J. Moosburger-Will, E. Nold, R. Morari, V.V. Ryazanov, A.S. Sidorenko, S. Horn, R. Tidecks, and L.R. Tagirov, "Reentrant Superconductivity in Superconductor/Ferromagnetic-Alloy Bilayers," *Phys. Rev. B*, vol. 82, p. 054517, 2010.

[29] V.I. Zdravkov, Kehrle J., Obermeier G., Ullrich A., Gsell S., Schreck M., Müller C., Morari R., Sidorenko A. S., Tagirov L. R., Tidecks R., and Horn S., "Interference Effects of the Pairing Wave Function Due to the Fulde-Ferrell Larkin-Ovchinnikov Like State in Ferromagnet/Superconductor Bilayers," *Supercond. Sci. Technol.*, vol. 24, p. 095004, 2011.

[30] J. Kehrle, V.I. Zdravkov, G. Obermeier, J. Garcia-Garcia, A. Ullrich, C. Müller, R. Morari, A.S. Sidorenko, S. Horn, L.R. Tagirov, and R. Tidecks, "Critical Temperature Oscillations and Reentrant Superconductivity Due to the FFLO Like State in F/S/F Trilayers," *Ann. Phys.*, vol. 524, p. 37, 2012.

[31] J. Aarts, J.M.E. Geers, E. Brück, A.A. Golubov, and R. Coehoorn, "Interface Transparency of Superconductor/Ferromagnetic Multilayers," *Phys. Rev. B*, vol. 56, p. 2779, 1997.

[32] E.A. Demler, G.B. Arnold, and M.R. Beasley, "Superconducting Proximity Effects in Magnetic Metals," *Phys. Rev. B*, vol. 55, p. 15174, 1997.

[33] C.L. Chien and D.H. Reich, "Proximity Effects in Superconducting/Magnetic Multilayers," *J. Magn. Magn. Mater*, vol. 200, p. 83, 1999.

[34] V.I. Zdravkov, A. Sidorenko, G. Obermeier, S. Gsell, M. Schreck, C. Müller, S. Horn, R. Tidecks, and L.R. Tagirov, "Reentrant Superconductivity in Nb/Cu1-xNix Bilayers," *Phys. Rev. Lett.*, vol. 97, p. 057004, 2006.

[35] Z. Eilenberger, "Transformation of Gorkov's Equation for Type II Superconductors into Transport-Like Equations," *Z. Phys.*, vol. 214, p. 195, 1968.

[36] Z.G. Ivanov , M.Yu. Kupriyanov, K.K. Likharev, S.V. Meriakri, and O.V. Snigirev, "Boundary Conditions for the Eilenberger and Usadel Equations and Properties of "Dirty" SNS Sandwiches," *Sov. J. Low Temp. Phys.*, vol. 7, p. 274, 1981.

[37] M.Yu. Kupriyanov and V.F. Lukichev, *Sov. Phys. JETP*, vol. 67, p. 1163, 1988.

[38] J. Linder, M. Zareyan, and A. Sudbo, "Proximity Effect in Ferromagnet/Superconductor Hybrids: From Diffusive to Ballistic Motion," *Phys. Rev. B*, vol. 79, p. 064514, 2009.

[39] L. Tagirov, "Private Communications,".

[40] C. Weißmantel and C. Hamann, *Grundlagen der Festkörperphysik*. Berlin: Springer, 1980.

[41] Ch. Kittel, *Einführung in die Festkörperphysik*, 13th ed. München Wien: Oldenbourg, 2002.

[42] I.M. Ryzhik and I.S. Gradsteyn, *Tables of Integrals Sums and Rows and its Multiplications*, I.S. Gradsteyn and I.M. Ryzhik, Eds. Moscow, 1963.

[43] M. Abramowitz and I.A. Stegun, Eds., *Handbook of Mathematical Function With Formulas, Graphs, and Mathematical Tables*, 10th ed. Washington D.C., USA: United States Department of Commerce, 1964.

[44] I.S. Gradshteyn and I.M. Ryzhik, *Tables of Integrals, Series, and Products*, 5th ed., A. Jeffrey, Ed. San Diego, U.S.A/CA: Academic Press, 1994.

[45] A. S. Sidorenko, V. I. Zdravkov, A. Prepelitsa, C. Helbig, Y. Luo, S. Gsell, M. Schreck, S. Klimm, S. Horn, L. R. Tagirov, and R. Tidecks, "Oscillations of the Critical Temperature in Superconducting Nb/Ni Bilayers," *Ann. Phys. (Leipzig)*, vol. 12, p. 37, 2003.

[46] I.N. Bronstein and K.A. Semendjajew, *Taschenbuch der Mathematik*, 24th ed. Frankfurt: Deutsch Harri, 1989.

[47] A.A. Abrikosov, *Fundamentals of the Theory of Metals*. Amsterdam, North Holland: Elsevier Science Ltd, 1988.

[48] M. Tinkham, *Introduction to Superconductivity*, 2nd ed. NY: McGraw Hill, 1996.

[49] P.G. de Gennes, "Boundary Effects in Superconductors," *Rev. Mod. Phys.*, vol. 36, p. 225.

[50] C. Strunk, C. Sürgers, U. Paschen, and H. v. Löhneysen, "Superconductivity in Layered Nb/Gd Films," *Phys. Rev. B*, vol. 49, p. 4053, 1994.

[51] W.-K. Chu, A.W. Mayer, and M.-A. Nicolet, *Backscattering Spectrometry*. San Diego: Academic Press, 1978.

[52] G. Schatz and A. Weidinger, *Nukleare Festkörperphysik*. Stuttgart: Teubner, 1992.

[53] T.L. Alford, L.C. Feldman, and J.W. Mayer, *Fundamentals of Nanoscale Film Analysis*. New York: Springer, 2007.

[54] M. Thompson. (2011, Okt.) Computer Graphic Service - The very minimal Genplot and RUMP Web page! [Online]. http://www.genplot.com/

[55] M. Mayer. (2011, Okt.) SIMNRA Home Page. [Online]. http://home.rzg.mpg.de/~mam/

[56] M.C. Neuburger, "Präzisionsmessung der Gitterkonstante von Niob," *Z. Anorg. Allg. Chem.*, vol. 197, p. 219, 1931.

[57] R.C. West, *Handbook of Chemistry and Physics*. Cleveland: Chemical Rubber Company (CRC) Press, 1975.

[58] M. Chen , B. Hallstedt, and L.J. Gauckler, "Thermodynamic Assessment of the Co-O System," *J. Phase Equilib.*, vol. 24, p. 212, 2003.

[59] S. Greenwald, "The Antiferromagnetic Structure Deformations in CoO and MnTe," *Acta Cryst.*, vol. 6, p. 396, 1953.

[60] W.L. Smith and A.D. Hobson, "The Structure of Cobalt Oxide, Co3O4," *Acta Cryst.*, vol. B29, p. 362, 1973.

[61] D.B. Williams and C.B. Carter, *Transmission Electron Microscopy*, 2nd ed. Berlin, Heidelberg, New-York: Springer, 2009.

[62] B. Fultz and J.M. Howe, *Transmission Electron Microscopy and Diffractometry of Materials*. Berlin, Heidelberg, New-York: Springer, 2001.

[63] W.P. Davey, "Precision Measurements of the Lattice Constants of Twelve Common Metals," *Phys. Rev.*, vol. 25, p. 753, 1925.

[64] L. Vegard, "Die Konstitution der Mischkristalle und die Raumfüllung der Atome," *Z. Phys.*, vol. 5, p. 17, 1921.

[65] L. Vegard, *Z. Kristallogr.*, vol. 67, p. 239, 1928.

[66] Q.D. Jiang, Y.L. Xie, W.B. Zhang, H. Gu, Z.Y. Ye, K. Wu, J.L. Zhang, C.Y. Li, and D.L. Yin, "Superconductivity and Transport Properties in Ultrathin Epitaxial Single-Crystal Niobium Films," *J. Phys.: Condens Matter*, vol. 2, p. 3567, 1990.

[67] Y. Gotoh and I. Arai, "Calculation of Interfacial Energy of the fcc-bce Interface and Its Epitaxial Orientation Relationship," *Jpn. J. Appl. Phys.*, vol. 25, p. L583, 1986.

[68] Y. Gotoh and M. Uwaha, "Geometrical Interpretation of the Interfacial Energy between bcc and fcc Lattices and Preferred Orientation Relationship of the Epitaxy," *Jpn. J. Appl. Phys.*, vol. 26, p. L17, 1987.

[69] Y. Gotoh, M. Uwaha, and I. Arai, "Interpretation of the Epitaxial Orientation Relationship at bcc(110)/fcc(111) Interfaces," *Appl. Surf. Sci.*, vol. 33/34, p. 443, 1988.

[70] Y. Gotoh and H. Fukuda, "Interfacial Energy of the bcc (110)/fcc (111) Interface and Energy Dependence on its Size," *Surf. Sci.*, vol. 223, p. 315, 1989.

[71] N.F. Mott, "A Discussion of the Transition Metals on the Basis of Quantum Mechanics," *Proc. Phys. Soc.*, vol. 47, p. 571, 1935.

[72] N. Spaldin, *Magnetic Materials - Fundamentals and Device Applications*. Cambridge, UK: Cambridge University Press, 2003.

[73] J. Callaway and C.S. Wang, "Self-Consistent Calculation of Energy Bands in Ferromagnetic Nickel," *Phys. Rev. B*, vol. 7, p. 1096, 1973.

[74] S.A. Ahern, M.J.C. Martin, and W. Sucksmith, "The Spontaneous Magnetization of Nickel+Copper Alloys," *Proc. Roy. Soc.*, vol. A248, p. 145, 1958.

[75] R.B. Goldfarb and F.R. Fickett, *Units for Magnetic Properties*, 696th ed., U.S. Government Printing Office, Ed. Boulder, Colorado 801303: US Department of Commerce. National Bureau of Standards, 1985.

[76] A. Ruotolo, C. Bell, C.W. Leung, and M.G. Blamire, "Perpendicular Magnetic Anisotropy and Structural Properties of NiCu/Cu Multilayers," *J. Appl. Phys.*, vol. 96, p. 512, 2004.

[77] C. Tannous and J. Gieraltowski, "The Stoner-Wolfarth Model of Ferromagnetism," *Euro. J. Phys.*, vol. 29, p. 475, 2008.

[78] J.M.D. Coey, *Magnetism and Magnetic Materials*. Cambridge, UK: Cambridge University Press, 2010.

[79] W.H. Meiklejohn and C.P. Bean, "New Magnetic Anisotropy," *Phys. Rev.*, vol. 102, p. 1413, 1956.

[80] E.H. Meiklejohn and C.P. Bean, "New Magnetic Anisotropy," *Phys. Rev.*, vol. 105, p. 904, 1957.

[81] J. Nogues and I.K. Schuller, "Exchange Bias," *J. Magn. Magn. Mater.*, vol. 192, p. 203, 1999.

[82] P.W. Anderson, "Antiferromagnetism. Theory of Superexchange Interaction," *Phys. Rev.*, vol. 79, p. 350, 1950.

[83] M. Gruyters, "Cobalt Oxide/Ferromagnet Bilayers: Exchange Coupling and Dominance of the Antiferromagnet," *Europhys. Lett.*, vol. 64, p. 803, 2003.

[84] W.P. Meiklejohn, "Exchange Anisotropy—A Review," *J. Appl. Phys.*, vol. 33, p. 1328, 1962.

[85] M. Kiwi, "Exchange Bias Theory," *J. Magn. Magn. Mater.*, vol. 234, p. 584, 2001.

[86] A. P. Malozemoff, "Random-Field Model of Exchange Anisotropy at Rough Ferromagnetic-Antiferromagnetic Interfaces," *Phys. Rev. B*, vol. 35, p. 3679, 1987.

[87] P.J. van der Zaag, A.R. Ball, L.F. Feiner, R.M. Wolf, and P.A.A. van der Heijden, "Exchange Biasing in MBE Grown Fe3O4/CoO Bilayers: The Antiferromagnetic Layer Thickness Dependence," *J. Appl. Phys.*, vol. 79, p. 5103, 1996.

[88] B. You, Y. Wang, Y. Zhao, L. Sun, W. Sheng, M. Pan, and J. Du, "Exchange Bias in CoO/Co3O4 Bilayers," *J. Appl. Phys.*, vol. 93, p. 6587, 2003.

[89] C.A.F. Vaz, E.I. Altmann, and V.E. Henrich, "Exchange Bias and Interface Electronic Structure in Ni/Co3O4(001)," *Phys. Rev. B*, vol. 81, p. 104428, 2010.

[90] A.S. Sidorenko, V. Zdravkov, J. Kehrle, R. Morari, G. Obermeier, S. Gsell, M. Schreck, C. Müller, V.V. Ryazanov, S. Horn, L. Tagirov, and R. Tidecks, "Double Re-entrance of Superconductivity in Superconductor/Ferromagnet Bilayers," *J. Phys.: Conf. Series (JPCS)*, vol. 150, p. 052242, 2009.

[91] T.R. Lemberger, I. Hetel, J.W. Knepper, and F.Y. Yang, "Penetration Depth Study of Very Thin Superconducting Nb Films," *Phys. Rev. B*, vol. 76, p. 094515, 2007.

[92] M. Schöck, C. Sürgers, and H. v. Löhneysen, "Superconducting and Magnetic Properties of Nb/Pd 1-xFex/Nb Triple Layers," *Eur. Phys. J. B*, vol. 14, p. 1, 2000.

[93] J.Y. Gu, C.-Y. You, J.S. Jiang, J. Pearson, Ya.B. Bazaliy, and S.D. Bader, "Magnetization-Orientation Dependence of the Superconducting Transition Temperature in the Ferromagnet-Superconductor-Ferromagnet System: CuNi/Nb/CuNi," *Phys. Rev. Lett.*, vol. 89, p. 267001, 2002.

[94] A. Rusanov, R. Boogaard, M. Hesselberth, H. Sellier, and J. Aarts, "Inhomogeneous Superconductivity Induced in a Weak Ferromagnet," *Physica C*, vol. 369, p. 300, 2002.

[95] H. Sellier, C. Baraduc, F. Lefloch, and R. Calemczuk, "Temperature-Induced Crossover Between 0 and π States in S/F/S Junctions," *Phys. Rev. B*, vol. 68, p. 054531, 2003.

[96] V.V. Ryazanov, V.A. Oboznov, A.S. Prokofiev, and S.V. Dubonos, "Proximity Effect and Spontaneous Vortex Phase in Planar SF Structures," *JETP Letters*, vol. 77, p. 39, 2003.

[97] A. Potenza and A. Marrows, "Superconductor-Ferromagnet CuNi⁄Nb⁄CuNi Trilayers as Superconducting Spin-Valve Core Structures," *Phys. Rev. B*, vol. 71, p. 180503, 2005.

[98] J. Kim, J.H. Kwon, K. Char, H. Doh, and H.-Y. Choi, "Quantitative Analysis of the Proximity Effect in Nb⁄Co60Fe40, Nb⁄Ni, and Nb⁄Cu40Ni60 Bilayers," *Phys. Rev. B*, vol. 72, p. 014518, 2005.

[99] L. Cretion, A.K. Gupta, H. Sellier, F. Lefloc, M. Faure, A. Buzdin, and H. Courtois, "Scanning Tunneling Spectroscopy of the Superconducting Proximity Effect in a Diluted Ferromagnetic Alloy," *Phys. Rev. B*, vol. 72, p. 024511, 2005.

[100] C. Cirillo, S.L. Prischepa, M. Salvato, C. Attanasio, M. Hesselberth, and J. Aarts, "Superconducting Proximity Effect and Interface Transparency in Nb⁄PdNi Bilayers," *Phys. Rev. B*, vol. 72, p. 144511, 2005.

[101] G.P. Pepe, R. Latempa, L. Parlato, A. Ruotolo, G. Ausanio, G. Perluso, A. Barone, A.A. Golubov, Ya.V. Fominov, and M.Yu. Kupriyanov, "Proximity Effect in Planar Superconducting Tunnel Junctions Containing Nb⁄NiCu Superconductor/Ferromagnet Bilayers," *Phys. Rev. B*, vol. 73, p. 054506, 2006.

[102] Jinho Kim, Jun Hyung Kwon, K. Char, Hyeonjin Doh, and Han-Yong Choi, "Quantitative Analysis of the Proximity Effect in Nb⁄Co60Fe40, Nb⁄Ni, and Nb⁄Cu40Ni60 Bilayers," *Phys. Rev. B*, vol. 72, p. 014518, 2005.

[103] R.A. French, "Intrinsic type-2 Superconductivity in Pure Niobium," *Cryogenics*, vol. 8, p. 301, 1968.

Acknowledgment

First of all, I have to thank Priv.-Doz. Dr. Reinhard Tidecks for his guidance and mentoring the whole time of the thesis. During the discussions with him I learned much about superconductivity and about a very exact and precise thinking in the present topic. Without his valuable advice, discussion and support the thesis would not be thinkable in the present form.

Furthermore, I would like to thank Prof. Dr. S. Horn for the possibility of participating in this topic at the chair of Experimental Physics II.

Prof. Dr. Lenar Tagirov, for his patience in explaining the various aspects of his theory. During his visits at the University of Augsburg, my knowledge not only in the FFLO (-like) state deepened considerably, each time. He also fitted the theory to the experimental data.

Dr. Vladimir Zdravkov, for preparing the samples. The project was only possible through his deep experience in magnetron sputtering. Special thanks to him for the team work in the low temperature measurements.

Prof. Dr. Anatoli Sidorenko for taking care of the project and the sample preparation assembly in Kishinev since the early days.

Dr. Günter Obermeier and Dr. Robert Horny for their help and experience in low and ultra-low temperature measurements. They always had an open door to solve any difficulties arising in the low temperature laboratory.

Priv.-Doz. Dr. Hans-Albrecht Krug von Nidda for his help in interpreting the magnetic measurements.

Dipl. Phys. Aladin Ullrich for all kinds of discussion, especially concerning the TEM during the last years.

Dr. Moosburger-Will and Prof. Dr. J. Lindner for introducing me into the Transmission Electron Microscopy.

Daniel Lenk which made his bachelor thesis on this topic and contributed experimentally with RBS measurements.

Sabine Bessel and Dr. Günter Obermeier for ultra-sonic bonding of the samples for low temperature measurements.

Dr. Stefan Gsell for introducing me into the RBS measurement and fitting of the RBS data of the bilayer samples at the beginning.

Wolfgang Reiber, Sybille Heidemeyer und Birgit Knoblich for TEM sample preparation.

Dipl.-Ing. Dana Vieweg for making the SQUID measurements.

The work was supported by the Deutsche Forschungsgemeinschaft (DFG) under the grant No GZ: HO 955/6-1.

Publication List

1. J. Kehrle, V.I. Zdravkov, G. Obermeier, J. Garcia-Garcia, A. Ullrich, C. Müller, R. Morari, A.S. Sidorenko, S. Horn, L.R. Tagirov, R. Tidecks, Critical Temperature Oscillations and Reentrant Superconductivity Due to the FFLO Like State in F/S/F Trilayers, Ann. Phys. (Berlin) **524**, 37 (2012).

2. V.I. Zdravkov, J. Kehrle, G. Obermeier, C. Müller, R. Morari, A. Sidorenko, S. Horn, R. Tidecks, and L. Tagirov, *A Superconducting Spin Valve Core Structure Based on the FFLO Like State: Studies on Bilayers and Trilayers of Superconductors and Ferromagnets*, Submitted to: 26th International Conference on Low Temperature Physics (LT26) - Beijing, China, 10-17 August, 2011. Accepted for publication in: Journal of Physics: Conference Series (2012).

3. V.I. Zdravkov, J. Kehrle, G. Obermeier, A. Ulrich, S.Gsell, M. Schreck, C. Müller, R. Morari, A.S. Sidorenko, L.R. Tagirov, R. Tidecks, and S. Horn, *Interference Effects of the Pairing Wave Function Due to the Fulde-Ferrell Larkin-Ovchinnikov Like State in Ferromagnet/Superconductor Bilayers*, Supercond. Sci. Technol. **24**, 095004 (2011).

4. V. I. Zdravkov, J. Kehrle, G. Obermeier, S. Gsell, M. Schreck, C. Müller, H.-A. Krug von Nidda, J. Lindner, J. Moosburger-Will, E. Nold, R. Morari, V. V. Ryazanov, A. S. Sidorenko, S. Horn, R. Tidecks, and L. R. Tagirov, *Reentrant Superconductivity in Superconductor/Ferromagnetic-Alloy Bilayers*, Phys. Rev. B **82**, 054517 (2010).

5. A. S. Sidorenko, V. I. Zdravkov, J. Kehrle, R. Morari, E. Antropov, G. Obermeier, S. Gsell, M. Schreck, C. Müller, V. V. Ryazanov, S. Horn, R. Tidecks, and L. R. Tagirov *Extinction and Recovery of Superconductivity by Interference in Superconductor/Ferromagnet Bilayers*, in *Nanoscale Phenomena - Fundamentals and Applications.*

H. Hahn, A. Sidorenko, I. Tiginyanu, Eds. (Springer-Verlag, Berlin-Heidelberg, 2009) Chap. 1.

6. J.-M. Kehrle, V. V. Zdravkov, R. Morari, A. Prepelitsa, C. Müller, A. Wixforth, S. R. Horn, R. Tidecks, A. Sidorenko, *Change of the Effective Dimensionality of an Nb/CuNi Bilayer in an External Magnetic Field*, J. Phys: Condens Matter **21**, 254202 (2009).

7. A.S. Sidorenko, V.I. Zdravkov, J. Kehrle, R. Morari, G. Obermeier, S. Gsell, M. Schreck, C. Müller, M.Yu. Kupriyanov, V.V. Ryazanov, S. Horn, L. R. Tagirov, and R. Tidecks, *Quasi-One-Dimensional Fulde-Ferrell-Larkin-Ovchinnikov-like State in* $Nb/Cu_{0.41}Ni_{0.59}$ *Bilayers*, Pis'ma v ZhETF **90**, 149 (2009) [JETP Lett. **90**, 139 (2009)].

8. A.S. Sidorenko, V. Zdravkov, J. Kehrle, R. Morari, G. Obermeier, S. Gsell, M. Schreck, C. Müller, V. Ryazanov, S. Horn, L.R. Tagirov, and R. Tidecks, *Double Re-entrance of Superconductivity in Superconductor/Ferromagnet Bilayers.* The 25th International Conference on Low Temperature Physics (LT25), Amsterdam, The Netherlands, August 6-13, 2008. Journal of Physics: Conference Series (JPCS) **150**, 052242 (2009), doi:10.1088/1742-6596/150/5/052242.

9. V.I. Zdravkov, J. Kehrle, G. Obermeier, A. Ullrich, C. Müller, R. Morari, A. Sidorenko, L. Tagirov, R. Tidecks, and S. Horn, *FFLO like State in Bilayers and Trilayers of Superconductors and Ferromagnets: The Spin-Valve Core Structure*, 75th Annual Meeting of the DPG and combined DPG Spring Meeting 2011, Dresden, 13-18 March 2011, Verhandl. DPG (VI) 46, 1/TT 10.54 (2011).

10. Kehrle, J.M.; Zdravkov, V.; Obermeier, G.; Morari, R.; Antropov, E.; Prepelitsa, A.; Müller, C.; Wixforth, A.; Horn, S.; Tidecks, R.; Sidorenko, A. *Crossover from 2D-3D Behavior in Superconducting Nb/CuNi Bilayers in a Magnetic Field*. 73th Annual Meeting of the DPG and combined DPG spring Meeting 2009, Dresden, 22-27 March 2009, Verhandl. DPG (VI) 44, TT 32.16 (2009).

Curriculum Vitae

Jan-Michael Kehrle

PERSONAL DETAILS

Date of birth: 30th of June, 1977
Place of Birth: Augsburg, Germany
Nationality: German

EDUCATION

Since 10/2007	PhD student at the University Augsburg
10/2003-03/2007	Master Student of Material Science at the University Augsburg Obtained Degree: Master of Science (M.Sc.) in Material Science
02/2001-10/2003	Undergraduate studies in Physics at the Open University, Milton Keynes, Great Britain Obtained Degree: Bachelor of Science with Honors
10/1999-08/2004	Student of Business Administration at the University Augsburg Obtained Degree: Diplom Kaufmann
10/1998-04/1999	Physics Studies at the University Augsburg
11/1997-08/1998	Military Service at the Bundeswehr
10/1988-07/1997	Holbein Gymnasium Augsburg